FREQUENCY-MODULATED CONTINUOUS-WAVE SYNTHETIC-APERTURE RADAR: IMPROVEMENTS IN SIGNAL PROCESSING

by

©Yake Li

A thesis submitted to the

School of Graduate Studies

in partial fulfillment of the requirements for the degree of

Doctor of Philosophy

Faculty of Engineering and Applied Science

Memorial University of Newfoundland

May, 2016

St. John's Newfoundland and Labrador

ABSTRACT

With the advance of solid state devices, frequency-modulated continuous-wave (FMCW) designs have recently been used in synthetic-aperture radar (SAR) to decrease cost, size, weight and power consumption, making it deployable on smaller mobile platforms, including small (< 25 kg) unmanned aerial vehicle(s) (UAV). To foster its mobile uses, several SAR capabilities were studied: moving target indication (MTI) for increased situational awareness, bistatic operation, e.g. in UAV formation flights, for increased range, and signal processing algorithms for faster real-time performance.

Most off-the-shelf SAR systems for small mobile platforms are commercial proprietary and/or military (ITAR, International Trades in Arms Regulations) restricted. As such, it necessitated the design and build of a prototype FMCW SAR system at the early stage to serve as a research tool. This enabled unrestricted hardware and software modifications and experimentation.

A model to analyze the triangularly modulated (TM) linear frequency modulated (LFM) waveform as one signal was established and used to develop a MTI algorithm which is effective for slow moving targets detection. Experimental field data collected by the prototyped FMCW SAR was then used to validate and demonstrate the effectiveness of the proposed MTI method.

A bistatic FMCW SAR model was next introduced: Bistatic configuration is a potential technique to overcome the power leakage problem in monostatic FMCW SAR. By mounting the transmitter and receiver on spatially separate mobile (UAV) platforms in formation deployment, the operation range of a bistatic FMCW SAR can be significantly improved. The proposed approximation algorithm established a signal model for bistatic

FMCW SAR by using the Fresnel approximation. This model allows the existing signal processing algorithms to be used in bistatic FMCW SAR image generation without significant modification simplifying bistatic FMCW SAR signal processing.

The proposed range migration algorithm is a versatile and efficient FMCW SAR signal processing algorithm which requires less memory and computational load than the traditional RMA. This imaging algorithm can be employed for real-time image generation by the FMCW SAR system on mobile platforms. Simulation results verified the proposed spectral model and experimental data demonstrated the effectiveness of the modified RMA.

ACKNOWLEDGEMENTS

I would like to thank my supervisor Dr. Siu O'Young for his support, advice, and direction throughout my years of research. Without his support, the radar would not have been built. I thank him for helping me through the most difficult times when every goal seemed to be out of reach. But, I also had fun because he has built such a wonderful research team.

I also would like to thank Robert MacIsaac for his careful and patient help in solving many of the problems I encountered during these years. Thanks are also due to all my supervisory committee members: Dr. Eric Gill and Dr. Weimin Huang for their insight and directions. For my fellow Ph.D. research students in RAVEN (Remote Aerial Vehicle for ENvironmental-monitoring, a Major Research Partnership project supported by the Atlantic Innovation Fund): Kevin Murrant, Jordan Peckham, Brendan Harvey, Iryna Borshchova and Oihane Cereceda, and the RAVEN staff: Scott Fang, Dr. Yu Liu, Dilhan Balage, Stephen Crewe and Noel Purcell, I am grateful for your comradeship and support.

To my dear wife, Xiaowei: Thank you for your love and encouragement, and for helping me to overcome all the difficulties in every step of the way. I could not have gone through all these years without your support.

And to my daughter, Emma, this is for you.

TABLE OF CONTENTS

LIST OF FIGURES

LIST OF TABLES

LIST OF ABBREVIATIONS

ADC	analog to digital converter
BYU	Brigham Young university
CCU	central control unit
CSA	chirp scaling algorithm
CTFT	continuous time Fourier transform
CTIFT	continuous time inverse Fourier transform
CW	continuous wave
DDS	direct digital synthesizer
DFT	discrete Fourier transform
DMA	direct memory access
FFT	fast Fourier transform
FM	frequency modulation
FMCW	frequency modulated continuous wave
FT	Fourier transform
FSA	frequency scaling algorithm
GPS	global positioning system
IDFT	inverse discrete Fourier transform
IF	intermediate frequency
IFFT	inverse fast Fourier transform
IFT	inverse Fourier transform
IMU	inertial measurement unit
ITAR	international trades in arms regulations

LFM	linear frequency modulated
MTI	moving target indication
OCXO	oven controlled crystal oscillator
PCB	printed circuit board
PLL	phase locked loop
PLSR	peak to sidelobe ratio
POSP	principle of stationary phase
PRF	pulse repetition frequency
PRT	pulse repetition time
RCM	range cell migration
RAVEN	remote aerial vehicle for environmental-monitoring
RCMC	range cell migration correction
RDA	range Doppler algorithm
RF	radio frequency
RFM	reference function multiplication
RMA	range migration algorithm
RVP	residual video phase
SAR	synthetic aperture radar
SF	stepped frequency
SM	sawtooth modulated
SNR	signal to noise ratio
SRC	second range compression

TM	triangularly modulated
UAV	unmanned aerial vehicle
VCO	voltage controlled oscillator

LIST OF SYMBOLS

Symbol	Definition	Page of first appeared
f_0	Centre frequency	13
t	Range time	13
Bw	Bandwidth of the transmitted signal	13
T	Pulse repetition time	13
k	Range Frequency modulation rate	13
$s_T(t)$	Value of transmitted signal as a function of time t	13
$rect$	Rectangular function	13
$s_R(t)$	Value of received signal as a function of time t	13
τ	Propagation delay of the transmitted signal	13
c	Speed of light	13
R_0	MTI: distance between target and radar	13
R_0	SAR: closest approach distance	21
$s_{IF}(t)$	Value of IF signal as a function of time t	14
f	Range frequency variable	14
$S_{IF}(f)$	Fourier transform of $s_{IF}(t)$	14
ρ_s	Range resolution	14
$\mathrm{sinc}(x)$	$\mathrm{sinc}(x) = \sin(\pi x)/(\pi x)$	14
f_s	ADC sampling rate	15

Symbol	Definition	Page of first appeared
λ	Wavelength	20
η	Azimuth time (slow time)	21
$R(\eta)$	Instantaneous slant range as a function of slow time	21
θ	Instantaneous incidence angle	21
η_c	Azimuth Doppler centre time	21
v	Radar speed	22
v_r	Radial speed	22
k_a	Azimuth Frequency modulation rate	22
T_a	Synthetic aperture time	23
D	Physical length of the radar antenna in azimuth	23
ρ_a	Azimuth resolution	23
Bw_a	Azimuth signal bandwidth	23
f_η	Azimuth frequency	30
$H_a(f_\eta)$	Azimuth matched filter as a function of f_η	31
l	Ambiguity index	78
R_{0R}	Closest approach distance between the receiver and target	92
R_{0T}	Closest approach distance between the transmitter and target	92
η_{0R}	Closest approach time of the receiver	92
η_{0T}	Closest approach time of the transmitter	92

Symbol	Definition	Page of first appeared
v_R	Receiver speed	92
v_T	Transmitter speed	92
$D\left(f_\eta, v\right)$	Cosine of θ as a function of f_η and v	97

CHAPTER 1. INTRODUCTION

The modern radar (RAdio Detection And Ranging) system was developed during the 1920s. The original purpose was to detect and measure the range to airborne targets which are too far away to be detected by optical devices. Short pulses were used to measure the distance and velocity, and pulse compression techniques were then employed to improve resolution for longer pulses. Target information, such as range, azimuth angle and speed were obtained by the first generation radar systems.

A milestone in radar development was the realization of the synthetic-aperture radar (SAR) concept. The SAR concept was first proposed under the name 'Doppler beam-width sharpening' by Carl A. Wiley [1] at Goodyear Aircraft Company in 1951. The same concept was proposed independently around the same time by Sherwin and others at the University of Illinois [2]. The basic idea of SAR is to use the inherent resolution of Doppler frequency shifts to resolve objects in the cross-range (azimuth) dimension so that a two-dimensional image, similar to that of an optical sensor, can be generated. An interferometric mode [3] was later developed to obtain three-dimensional information of the target so that the height of an object could also be measured.

The first SAR images were obtained by using film recording and optical processing [4]. Digital signal processing techniques were developed in the mid 1960s. With the increasing speed of large scale integrated circuits, SAR images, which used to need several hours to generate, can now be displayed in real time using embedded computers on small mobile platforms.

A SAR is an active device in that it has its own transmitter and does not depend on ambient radiation. This allows it to work under most weather conditions and measure dis-

tance accurately. For example, long-term interferometric observation using satellite SAR can measure to as little as a 1 mm in land movement per year [5]. Moreover, microwave energy can penetrate plants and soil, and is sensitive to strong reflectors (like metal objects), which makes it a good alternative to optical sensors in many instances.

Bistatic SAR represents an important development in SAR techniques. In a bistatic configuration, the transmitting and receiving channels of the radar system are spatially separated on different platforms. This configuration makes the realization of SAR more flexible and provides advantages over the monostatic configuration [6], [7]. Although bistatic experiments were conducted in the 1970s–1980s [6], bistatic SAR is still not widely used because of technical difficulties in synchronization. Since the transmitter and the receiver are spatially separated and SAR works at a high pulse-repetition frequency (PRF), time synchronization between the transmitting channel and the receiving channel is difficult to obtain. Moreover, the spatial synchronization problem (the transmitting and receiving antennas should be pointed at the same area) is another factor that needs to be overcome. However, with the advancements in UAV technology, the synchronization problem can be minimized and the bistatic SAR technique may become more popular.

Another important trend in the development of airborne SAR is miniaturization that allows the system to be mounted on a small UAV. The combination of a SAR and a UAV provides a versatile and cost-effective solution to real time ground/ocean monitoring. FMCW techniques are an attractive choice to accomplish these tasks because they require simpler radar structures and they can easily be realized by solid-state devices.

FMCW techniques have been widely implemented in recent years on various applications such as SAR imaging [8]–[16], automotive detection [17]–[19] and sea state

measurement [20]. FMCW radar constantly transmits and receives signals and is thus capable of maintaining a high signal to noise ratio (SNR) while transmitting much less peak power than a corresponding pulse radar system. Since more time is used to generate the signal, the frequency modulation (FM) rate can be kept low, which makes it easier to achieve high signal bandwidth.

Since the middle of the last century, FMCW techniques have only been used in limited applications such as radio altimeters. The main reason was the isolation requirement between the transmitter and the receiver. Unlike pulse radar systems, FMCW radar transmits and receives during the whole pulse repetition time (PRT). This causes direct energy feedthrough from the transmitter to the receiver. By separating the transmitting and receiving antennas, an isolation up to 60dB [21] can be achieved. However, the detection range of FMCW radar is limited to several kilometers because the compact size of a typical FMCW radar on a single small mobile platform does not allow sufficient spatial separation between the transmitting and receiving antennas. Therefore, the transmitted power of an FMCW radar is normally limited to several watts even if the devices can handle more.

The technology that extends the FMCW radar to broader applications is the development of solid-state devices. Modern silicon integrated circuits have the advantages of miniaturization and low cost. Unlike vacuum tubes, they cannot handle high peak power, which makes their use in the traditional high-peak-power pulse radar systems difficult. An FMCW radar works continuously and is hence readily compatible with small solid-state devices. Therefore, even though the detection range is limited to a few kilometers, FMCW radars are now much smaller, lighter and less expensive than comparable pulse

radar systems. This makes them very suitable as a viable payload to work on smaller mobile platforms such as small UAV.

1.1 Motivation and Purpose

The systems and imaging processing algorithms (for real time and for post processing) for pulse SAR have been significantly improved since the middle of last century when the concept of SAR was first proposed. Sophisticated airborne and space-borne pulse SAR systems have then been developed and put to operation. Compared with the various pulse SAR systems, FMCW SAR was only developed and experimented recently [8] in this century with the increasing demand of UAV SAR operation. Most of the FMCW SAR systems are still under development and only very few of them have been commercialized. As a relatively new technique, the FMCW SAR systems available on the market are either very expensive or have strict export control (ITAR). Moreover, different from the pulse SAR data that are commercially available, there are no FMCW SAR data available in the market. Therefore, designing and building a customized FMCW SAR system is the only way to realize UAV SAR imaging and to conduct related experiments.

The initial plan was to build a simple stepped frequency radar using off-the-shelf components for SAR operation. However, the radar altimeter has been found to be not suitable for SAR imaging during the experiments, because the coherence and the PRF of the altimeter are not high enough and the recorded data is not well defined in the frequency domain. A high PRF, highly coherent, and wideband FMCW SAR was then designed and built in-house using printed circuit boards (PCBs) and basic microwave components.

Ground experiments were conducted and the results verified the coherence characteristics of the FMCW SAR.

Despite imagery, the high phase coherency provided by SAR system can be used for moving target indication (MTI), which increases the application areas of the FMCW SAR. Though the triangularly modulated (TM) linear frequency modulated (LFM) signal has been employed in many FMCW SAR systems, it was treated and analyzed as two separate sawtooth signals [17]–[19], [22]. Only one side of the TM-LFM signal, which is a sawtooth modulated (SM) LFM signal, is used in signal processing most times, while the other side of the TM-LFM signal is discarded. The motivation to combine the up chirp side and down chirp side of the TM-LMF signal generates a model to express both sides of a TM-LFM signal by one equation, and subsequently a MTI method which is based on the new model and is especially effective on slow moving target indication.

One limitation of the FMCW SAR system is the power leakage from the transmitter to the receiver due to the continuous operation of FMCW principles. This limits the operation range of the FMCW SAR. One method to improve the isolation between transmitter and receiver is to separate the transmitting and receiving antennas [21]. However, monostatic FMCW SAR does not allow much separation because the transmitting and receiving antennas need to be mounted on the same platform. To solve this problem, bistatic configuration is studied and a bistatic FMCW SAR model is proposed to simplify the signal processing of bistatic FMCW SAR. As the synchronization (which is important in bistatic configuration) of UAV can be well realized using autopilots, the bistatic FMCW SAR configuration is possible to be implemented in the near future to increase the radar range.

Another concern that arises during the building of the FMCW SAR system is the signal processing problem, especially when real-time processing is necessary. A versatile and high efficient algorithm for signal processing is important because the configuration and operation conditions of FMCW SAR may change according to real situations. The efficiency of an algorithm is also very important in real time image generation. Range migration algorithm (RMA) is one of the most universal algorithms in pulse SAR signal processing. Unfortunately, the efficiency of this algorithm is low [5], which makes the algorithm hard to be implemented in real time signal processing. In FMCW SAR, because of the special characteristics of the intermediate frequency (IF) signal introduced by dechirp-on-receive demodulation, the traditional RMA used in pulse SAR signal processing can be improved and more efficiently used in FMCW SAR signal processing. This modified RMA increases the capability of FMCW SAR real time signal processing.

The purpose of this thesis is to improve SAR signal processing capabilities, with an application focus on small mobile platform deployment, to complement advances in SAR hardware development. Specially, the following stepped approaches were taken:

(a) Design and build a prototype FMCW SAR system suitable for research purposes.

(b) Study moving target indication algorithms to increase the application areas of FMCW SAR.

(c) Research bistatic FMCW SAR signal model to lay the foundation for FMCW SAR imaging range increase by using bistatic configuration.

(d) Investigate the FMCW SAR signal processing algorithms for image generation.

The technical and theoretical challenges that had been overcome were:

(a) Design, build and test of a FMCW SAR using off-the-shelf components with limited access to high-frequency test equipment.

(b) Develop a signal model for indicating moving target by FMCW SAR.

(c) Develop a signal model for bistatic FMCW SAR signal analysis.

(d) Improvement of the existing FMCW SAR signal processing algorithms.

1.2 Overview

Figure 1.1 shows the overview of the work.

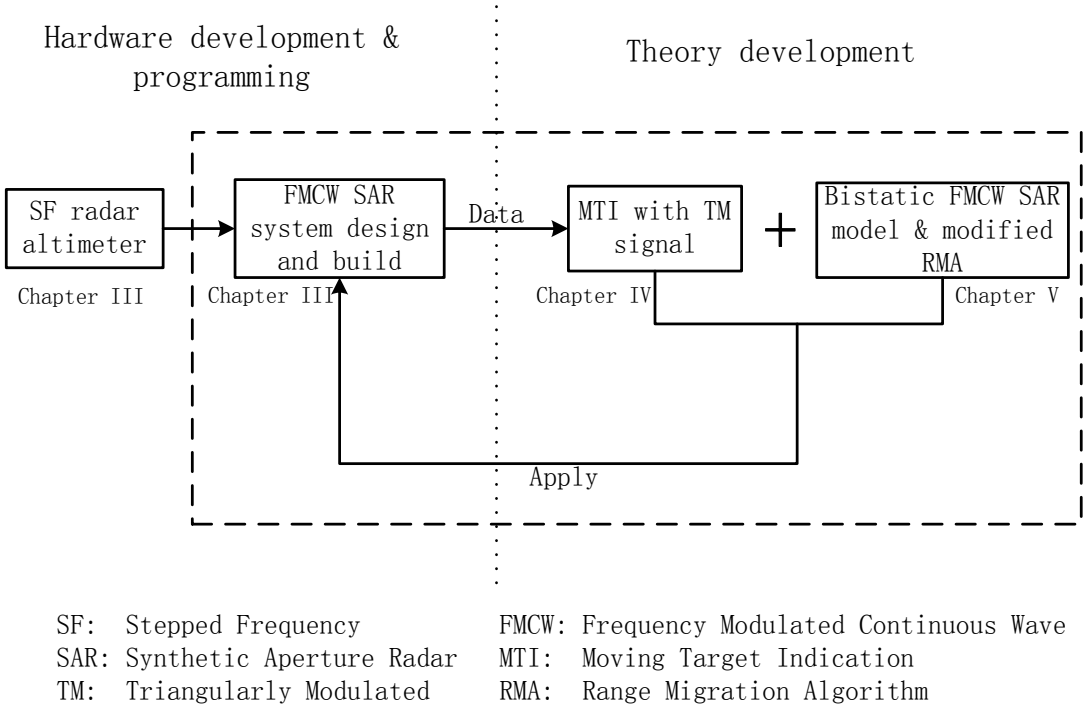

Figure 1.1 Overview of the Ph.D. work

Two different parts of work have been conducted: the first part is the hardware development and the second part is the theory development.

The start of the Ph.D. program was to build a stepped frequency (SF) radar altimeter. The altimeter was then found not able to perform SAR operation. Subsequently, with the

experience obtained during the building of the altimeter, a fully customized FMCW SAR was designed and built. The data collected by the FMCW SAR was then used to verify some of the conclusions obtained in the theory development. The hardware work is documented in Chapter 3. The prototype FMCW SAR built has the potential to be developed into a multifunctional radar that can be mounted on UAV to improve the capability of aerial surveillance and monitoring.

The theory development is composed by two parts. The first part includes a new model for analyzing TM-LFM signal, and a MTI method especially efficient for slow target indication. The developed MTI algorithm provides a new method to use SAR for moving targets indication.

The second part of the theory development consists of a model for bistatic FMCW SAR imaging and a modified RMA. The bistatic FMCW SAR model can be used for signal processing and the modified RMA can be used as a versatile and efficient real time signal processing algorithm.

In hardware development, since the FMCW SAR system is designed from the basic circuits and is built by basic electric and microwave elements, the radar does not depend on any off-the-shelf products in the market from the system level. The parameters and configurations of the radar system can be modified according to the experiment requirements.

In the theory research part, the data used by the algorithms are collected by the FMCW SAR system. Moreover, the algorithms developed during this stage can be used in the radar system for real time processing.

1.3 Contributions

The contributions are:

1. A high performance FMCW SAR has been designed and built using PCBs and microwave components. Since SAR systems are not commonly available in the non-military market and the detailed designs do not appear in the literatures, the system had to be designed from scratch. The system uses one premium oven controlled crystal oscillator (OCXO) for the clocks of the entire system to improve the coherence. Only one chip is used to perform the control, data recording and real time processing tasks, simplifying the structure of the radar system. A direct digital synthesizer (DDS) is employed to generate the linear frequency modulated signal. High speed analog to digital converter (ADC) and data recording units are used to sample and record the data. The data are then processed by computer to generate SAR images. The whole system is controlled by hardware and hence has very accurate timing. SAR images have been generated during field experiments.
2. A novel mathematical model has been proposed for analyzing the two sides of TM-LFM signal as one signal. Triangular modulation is normally a requirement driven by radar hardware limitation rather than the ease of signal processing. Therefore, in some cases, only one side of the triangularly modulated signal is used for data processing. In other cases, the triangularly modulated signal is analyzed as two separated SM-LFM (up-chirp and down-chirp) signals for Doppler information extraction. The combination of the up-chirp and down-chirp as one

signal proposed changes the range sensitive term from a phase to an amplitude effect, which extends the applications of the TM-LFM signal.

3. A moving target indication (MTI) method has been proposed according to the model established for analyzing the TM-LFM signal. The traditional MTI algorithm using the triangular LFM signal is based on the opposite Doppler frequency shifts induced by the moving target to the up-chirp and down-chirp of a triangular LFM signal. These methods are not applicable when the Doppler effect is small, either caused by the slow radial speed or the high PRF. The proposed method takes advantage of the wavelength-order movement that occurs between the target and the radar to indicate the moving target and hence are particularly effective for slow moving targets and high PRF cases. The method is capable of detecting and measuring targets with speeds less than 1 m/s.
4. A spectral model based on the Fresnel approximation for FMCW bistatic SAR has been proposed. The new model approximated the dual square roots in the instantaneous slant range expression of the FMCW bistatic SAR by one square root. By using the new spectral model, the existing FMCW monostatic SAR imaging algorithms can be used to process bistatic data without significant modification. The proposed model simplifies data processing under normal bistatic configurations.
5. A modified range migration algorithm (RMA) has been proposed for processing the FMCW SAR data. Through exploitation of the special characteristics of the IF signal after dechirp-on-receive in FMCW SAR, a modified Stolt mapping is proposed to reduce the computational load and the memory needed during image

generation. The proposed algorithm modifies the traditional Stolt mapping [5] equation and decrease the memory needed in the traditional Stolt mapping. The proposed RMA has roughly the same computational load and memory size requirements as the range Doppler algorithm in FMCW SAR signal processing. If the same length of the spectrums, after Stolt mapping, is used for image generation, then better SAR images can be generated by using the modified RMA rather than by the traditional RMA.

1.4 Outline

This dissertation is organized as follows:

In Chapter 2, the background needed to understand the work in the remainder of this dissertation is introduced. Certain formulas in this chapter are the basis for the derivations in the following chapters. In the first part of Chapter 2, the principles and the basic formulas of FMCW and the stepped frequency technique are introduced. Then the principles and imaging algorithms of SAR are introduced in detail in the second part of Chapter 2. The algorithms derived in this part focus on FMCW SAR.

In Chapter 3, the design and construction of the prototype FMCW SAR is described. A stepped frequency radar built for altimeter use is first introduced as a reference. This indicates the required improvements to an FMCW system for SAR use. The design considerations of the FMCW SAR are then discussed. The structure, parameters and system considerations are described. The experimental results are given at the end of this chapter. This chapter corresponds to Contribution 1 in Section 1.3.

In the first part of Chapter 4, the mathematical method to analyze the TM signal as one signal is derived. Traditional methods analyze the TM signal as two separated SM

signals or only use one side of the TM signal. The proposed method in this chapter combines the two sides (up-chirp and down-chirp) of the TM signal as one signal when the target speeds are slow. An MTI method is then proposed by using the established model in the second part of Chapter 4. Instead of using the Doppler effect caused by target motion, the new method detects targets by exploiting their small radial movement in short time periods. The proposed method can detect slow moving targets and measure their velocities. This chapter corresponds to Contributions 2 and 3 in Section 1.3.

At the beginning of Chapter 5, an approximated spectral expression for bistatic FMCW SAR is developed based on the Fresnel approximation. The model is effective under long range and narrow azimuth beamwidth assumptions. The proposed spectral model is similar to that of a monostatic FMCW SAR, allowing the existing algorithms to be employed directly for image generation without significant modification. An extended RMA is then derived according to the characteristics of the IF signal obtained by dechirp-on-receive demodulation. This algorithm has the advantages of lower computational load and smaller data size. The method is first verified by simulation to process the FMCW bistatic SAR signal. Its effectiveness on FCMW monostatic SAR signal processing is then validated by simulation and the real data collected by the prototype FMCW SAR. This chapter corresponds to Contributions 4 and 5 in Section 1.3.

CHAPTER 2. BACKGROUND

The theory behind frequency modulated continuous wave (FMCW) radar will be presented in this chapter. The principles of the FMCW is presented first. As a special case of FMCW, the stepped frequency technique is then briefly introduced. The FMCW SAR is then introduced in detail. Firstly, an overview is given of SAR principles. Secondly, different SAR modes are introduced. Finally, two different algorithms, range Doppler algorithm (RDA) and range migration algorithm (RMA), are derived. The RDA provides a clear interpretation of the basic concept of SAR, as RMA is one of the most accurate SAR processing methods. Other important SAR imaging algorithms, such as the chirp scaling algorithm (CSA) [23]-[26] and frequency scaling algorithm (FSA) [22], [27]-[29] are not included in this chapter because only RDA and RMA were used in the signal processing for the FMCW SAR system in this dissertation.

2.1 FMCW Background and Literature Review

FMCW was one of the earliest techniques used by radar. Since a FMCW radar continuously transmits and receives signals, part of the transmitted power will be received directly by the receiving antenna and appear as a very strong returned signal. This is known as the power feedthrough problem. This leakage limits the transmitted power of the FMCW radar and hence influences the operational range. Therefore, the continuous wave (CW) signal was replaced by the pulse compression technique which permits transmitting and receiving at different times.

The FMCW technique has recently be realized using inexpensive and small solid state devices, and thus been widely used in small radar systems though the operation

range is still limited. The FMCW system commonly employs two different techniques that a pulse radar system does not.

The first technique is to use dual antennas. The transmitting and receiving antennas are normally separated in an FMCW radar to reduce the power feedthrough. The separation of the transmitter and receiver allows an isolation up to 60 dB [21]. However, the operation range of a compact FMCW radar is still limited to several kilometers because insufficient spatial isolation of the transmitter and receiver can be provided.

The second technique is the use of dechirp-on-receive. In pulse radar, the local reference signal used to demodulate the received signal is normally the carrier frequency and the demodulated signal is a baseband LFM signal. Unlike the orthogonal demodulation [5] in pulse radar, the FMCW radar uses a copy of the transmitted signal as the local reference signal for demodulation. Therefore, the IF signal in FMCW radar system is a monotone whose frequency is proportional to the target distance. In the case of short operational ranges, the ADC frequency needed to sample the IF signal is much lower in the dechirp-on-receive system than in the orthogonal demodulation system. Orthogonal demodulation is normally not used in dechirp-on-receive technique because it is difficult and expensive to phase shift the transmitted signal to produce a quadrature wideband reference signal. Therefore, only one channel of data, i.e. the data with only real part, is normally obtained in dechirp-on-receive demodulation.

2.1.1 FMCW Principles

A sawtooth sweep is used in this section to explain the principles of FMCW. A time-frequency plot that shows the principles of FMCW range measurement is shown in Figure 2.1. The top part shows the transmitted signal and the received signals from different

targets. The received signals are time delayed versions of the transmitted signal. The solid line is the transmitted signal, the dashed line is the returned echo from a closer target and the dotted line is the returned signal from a further target.

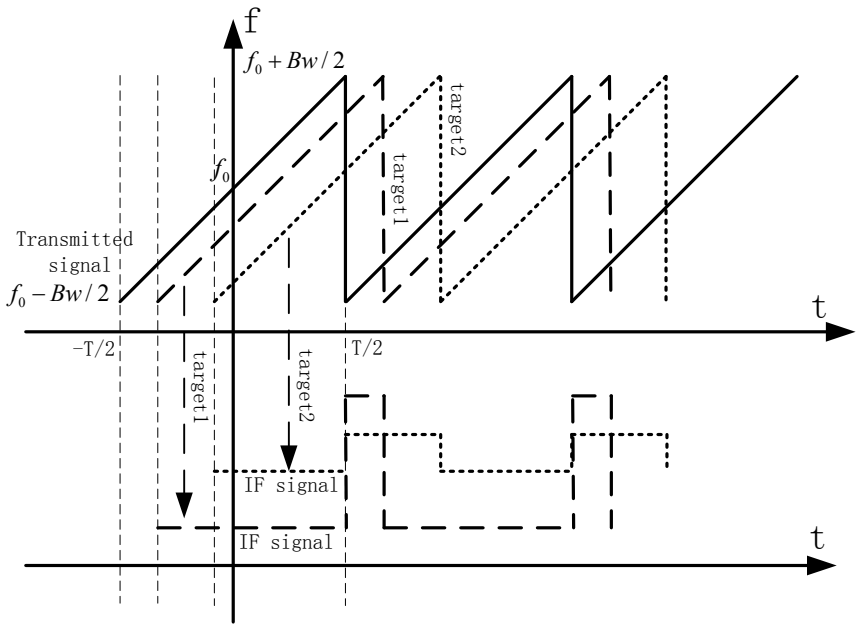

Figure 2.1 FMCW range measurement principles

The received signal is then mixed with a copy of the transmitted signal to generate the IF signal, through the dechirp-on-receive process. The time delay of the returned signal in Figure 2.1 is much exaggerated to better illustrate the principles. In real cases, the delay times are on the order of microseconds and the returned signal will be very close to the transmitted signal in time. Both the radar and the targets are assumed to be stationary in this section.

The IF signal is shown in the lower part of Figure 2.1. As shown by the dashed line, two different monotones appear in the IF signal for a single target. The frequency of the faster monotone is much higher than the slower one, and is eliminated by filtering. The IF

signal corresponding to a single target after filtering is a fixed frequency signal whose frequency is proportional to the target distance. The Fourier transform (FT) can be used to separate different targets in the frequency domain.

In Figure 2.1, f_0 is the carrier frequency, Bw is the bandwidth of the transmitted signal, and T is the PRT. The first period of the transmitted signal can be expressed as

$$s_T(t) = rect\left(\frac{t}{T}\right)\cos\left(\pi k t^2 + 2\pi f_0 t\right) \tag{2.1}$$

where

$$rect\left(\frac{t}{T}\right) = \begin{cases} 1 & |t| \le T/2 \\ 0 & others \end{cases} \tag{2.2}$$

is the rectangular function, and $k = Bw/T$ is the FM rate. For simplicity, the amplitude of the transmitted signal is assumed to be one.

The received signal is a time delayed version of the transmitted signal, which is

$$s_R(t) = \sigma \cdot rect\left(\frac{t}{T}\right)\cos\left[\pi k\left(t-\tau\right)^2 + 2\pi f_0\left(t-\tau\right)\right] \tag{2.3}$$

where

$$\tau = \frac{2R_0}{c} \tag{2.4}$$

is the two way time delay for a fixed target, R_0 is the distance between the radar and the target, c is the speed of light, and σ is the reflection coefficient, which is neglected in the following derivation without loss of generality. In real cases, R_0 is normally no more than several kilometers, and hence the time delay τ is on the order of tens of microseconds. This delay will slightly decrease the length of the frequency beating between the

reference signal and the received signal (as shown in Figure 2.1, the IF signal is shorter than the PRT). As the theoretical resolution is calculated by the IF signal of which the length equals to PRT, the shorter IF signal will lower the resolution. However, since the delay τ is very small compared with T (normally on the order of milliseconds), its effect on the resolution could be neglected. This is the reason why it is neglected in the rectangular function in (2.3). However, τ cannot be neglected in the phase because its coefficient in the phase is sufficiently large to make the two way time delay a significant contribution to the change of the phase. By measuring the change of phase, the LFM signal can be used to measure the distance of the target.

In dechirp-on-receive, the received signal (2.3) is then mixed with the transmitted signal (2.1). The sum frequency is eliminated by filtering, and only the beat frequency appears in the final IF signal, which is

$$s_{IF}(t) = rect\left(\frac{t}{T}\right)\cos\left(2\pi k\tau t - \pi k\tau^2 + 2\pi f_0\tau\right) \tag{2.5}$$

.

Eq. (2.5) is the IF signal sampled by ADC. To express the FT of (2.5), it is then expressed by exponential form. One way is to use Euler's identity. Eq. (2.5) can be expressed in exponential form by using Euler's identity as

$$s_{IF}(t) = \frac{1}{2}rect\left(\frac{t}{T}\right)e^{j2\pi k\tau t}e^{j2\pi f_0\tau}e^{-j\pi k\tau^2} + \frac{1}{2}rect\left(\frac{t}{T}\right)e^{-j2\pi k\tau t}e^{-j2\pi f_0\tau}e^{j\pi k\tau^2} \tag{2.6}$$

.

By using the FT pair

$$rect\left(\frac{t}{T}\right) \leftrightarrow T\,\mathrm{sinc}(Tf) \tag{2.7}$$

,

the (continuous time Fourier transform) CTFT of (2.6) can be expressed as

$$S_{IF}(f)=\frac{1}{2}T\text{sinc}\left[T(f-k\tau)\right]e^{j2\pi f_0\tau}e^{-j\pi k\tau^2}+\frac{1}{2}T\text{sinc}\left[T(f+k\tau)\right]e^{-j2\pi f_0\tau}e^{j\pi k\tau^2} \quad (2.8)$$

where $\text{sinc}(x)=\sin(\pi x)/(\pi x)$ is the sinc function.

Eq. (2.8) shows that two sinc-shaped peaks that are symmetric about the Y-axis appear in the frequency domain of $|s_{IF}(t)|$. One is at $f=k\tau$ and the other one is at $f=-k\tau$. The phases of the two peaks are opposite. In digital signal processing, the two peaks will appear in the digital frequency domain after fast Fourier transform (FFT) and be symmetric about zero frequency (if zero frequency point has been properly shifted to the centre of the frequency axis). The peak at $f=k\tau$ will be on the positive frequency side of the digital spectrum and the other peak will be on the negative frequency side.

As the two peaks have the same amplitudes and inverse phases, we can discard one and only use the other. In digital processing, this corresponds to discarding half of the digital spectrum and using the other half. Supposing we always keep the positive spectrum and discard the negative frequency, we have

$$S_{IFL}(f)=\frac{1}{2}T\text{sinc}\left[T(f-k\tau)\right]e^{j2\pi f_0\tau}e^{-j\pi k\tau^2} \quad (2.9)$$

.

The resolution of a LFM signal can now be analyzed by using (2.9). The existence of a target is indicated by the peak of this sinc function in frequency domain. Two factors affect the resolution of the IF signal: the peak position and the 3dB width.

Assuming the sampling rate of ADC is f_s. If the IF signal is continuously sampled during its whole duration, each sample in the digital frequency domain represents

$$\Delta f=\frac{f_s}{Tf_s}=\frac{1}{T}\ \ (\text{Hz}) \quad (2.10)$$

.

Therefore, the position of the sinc function in (2.9) is

$$\frac{k\tau}{\Delta f}=\frac{\left(Bw/T\right)\cdot\left(2R_0/c\right)}{\left(1/T\right)}=\frac{R_0}{\left(c/\left(2\cdot Bw\right)\right)}=\frac{R_0}{\rho_s}\ \left(\text{FFT samples}\right) \tag{2.11}$$

where $\rho_s=c/\left(2\cdot Bw\right)$ is the range resolution of the signal. Eq. (2.11) shows that a distance change equaling ρ_s will cause the sinc function to shift by one sample in FFT digital frequency domain.

The 3 dB width of the sinc function in (2.9) equals the reciprocal of the coefficient of the variable f, which is

$$\frac{1}{T}\left(Hz\right)=1\left(\text{sample}\right) \tag{2.12}$$

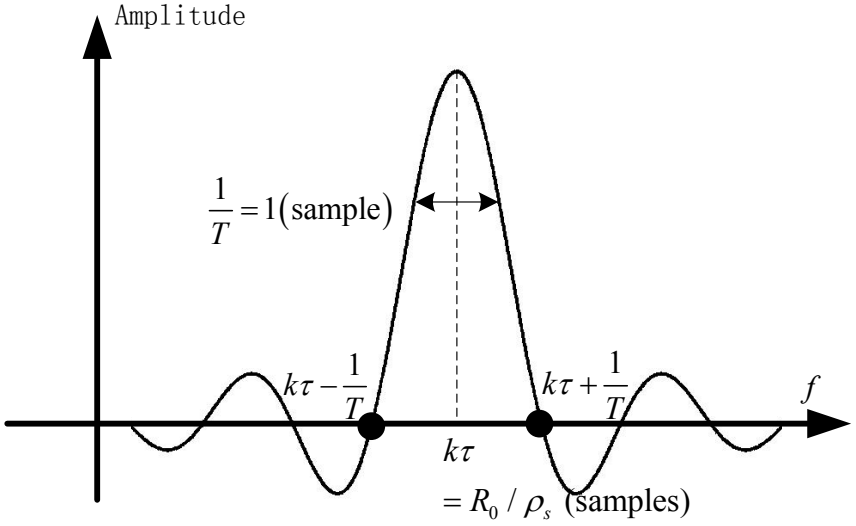

Figure 2.2 Sinc function

The sinc function in (2.9) is shown in Figure 2.2. When the distance of a target changes by ρ_s meters, the peak of the sinc function will move by 1 sample in digital fre-

quency domain. Since the 3dB width of the sinc function is 1 sample, then two targets that separated by ρ_s meters can be resolved in frequency domain.

Another way to explain the resolution of (2.9) is to use the definition of the resolution. If two targets that are R_1 and R_2 away from the radar are to be resolved, the centre of the sinc functions corresponding to each target must be separated by at least the 3 dB width of the sinc function, which leads to

$$k\left(\frac{2R_2}{c}-\frac{2R_1}{c}\right)\geq\frac{1}{T}\Rightarrow R_2-R_1\geq\frac{c}{2kT}=\frac{c}{2Bw}. \tag{2.13}$$

Eq. (2.13) shows that a minimum space separation of ρ_s is required if the two targets are to be resolvable by the IF signal in frequency domain.

From (2.12), we know that the 3dB mainlobe width of the sinc function in the spectrum of the IF signal after dechirp-on-receive is determined by the time duration of the signal if the original signal before demodulation is continuous.

2.1.2 Stepped Frequency Radar

Instead of transmitting continuous LFM signal, a pulse chain with discrete frequencies can be used to achieve high range resolution [30]. It is worth mentioning that there is another form of stepped frequency (SF) waveform, in which several wideband signals are transmitted with stepped centre frequencies so that a total bandwidth of over 1GHz can be achieved [31]. Different from this bandwidth synthesizing method, the SF technique introduced in this section is a special realization of the FMCW technique, which can be used to realize high range resolution with the simplest radar structure.

In SF radar, a monotone is transmitted in every pulse. The frequency of the monotones transmitted in different pulses is different. The simplest form is the constant frequency step, in which the frequency difference between each step is constant. All the frequency steps in a burst are combined at last to form the high resolution signal.

Assuming in the nth step of the chain, the transmitted signal is

$$s_T(t) = e^{j2\pi f_n t} \tag{2.14}$$

where f_n is the signal frequency of the nth step

$$f_n = f_0 + nf_{sp} \quad \text{n} \in \left(-\frac{N}{2}, \ \frac{N}{2} \right] \tag{2.15}$$

where N is the total numbers of the steps in one sweep, and f_{sp} is the frequency step which is a constant. f_0 is the centre frequency. The received signal is then

$$s_R(t) = e^{j2\pi f_n (t-\tau)} \tag{2.16}$$

where τ is the two way time delay. The IF signal obtained in the nth step is the beat frequency of (2.16) and (2.14), which is

$$s_{IF} = e^{j2\pi f_n \tau} \tag{2.17}$$

which represents a constant voltage because both f_n and τ in each step are constants. If all the different steps in a sweep chain are considered (substituting (2.15) into (2.17)), the combined IF signal will be

$$s_{IF}(n) = \text{g}(n) e^{j2\pi f_0 \tau} e^{j2\pi f_{sp} \tau \cdot n} \tag{2.18}$$

where

$$g(n)=1 \qquad -\frac{N}{2} \le n < \frac{N}{2} \,. \tag{2.19}$$

Eq. (2.18) is a discrete function of the variable n. The discrete Fourier transform (DFT) shows the position of the target in frequency domain, which is

$$S_{IF}(m)=\frac{\sin\left[\pi\left(m-Nf_{sp}\tau\right)\right]}{\sin\left[\frac{\pi}{N}\left(m-Nf_{sp}\tau\right)\right]}e^{-j(N-1)\frac{\pi}{N}\left(m-Nf_{sp}\tau\right)}e^{j2\pi f_0\tau} \quad \text{m=0,1,2...N-1} \tag{2.20}$$

where m is the frequency index in discrete frequency domain. The peak will appear at $m=Nf_{sp}\tau$ samples. Note that since $Nf_{sp}=Bw$, we have

$$Nf_{sp}\tau = Bw\cdot\frac{2R}{c}=\frac{R}{\rho_s} \tag{2.21}$$

where $\rho_s = c/2Bw$ is the range resolution. Comparing (2.21) with (2.11), it can be seen that the peak position expressed in discrete frequency domain is the same for both SF and FMCW radar.

As shown by the above derivation, the IF signal in each frequency step is a constant voltage. However, the IF signals between different steps are different. By combining all the IF signals of different frequency steps in a sweep chain, the combined IF signal for a single reflector is a sampled sinusoidal function. Therefore, the SF radar employs a discrete transmitting waveform in the transmission stage. In fact, the transmitted signal is a sampling of the corresponding continuous LFM signal.

The structure of the SF radar could be very simple, only including a voltage controlled oscillator (VCO), a mixer and antennas. However, the SF radar is not suitable for high PRF and high coherence requirements. The monotone has to be transmitted and re-

ceived inside the same frequency step, which limits the PRF of the radar. VCO is also not a good source for wide bandwidth generation in terms of phase stability. Therefore, the SF radar is normally used in the applications where coherence and PRF are not important.

2.2 Synthetic Aperture Radar Principles

2.2.1 SAR Concepts

The positioning of a target on a two dimensional plane needs both range and cross-range (azimuth) information. The range information can be obtained accurately in any pulse compression radar system, while the azimuth resolution is poor in real aperture radars (hundreds of meters) at long range. For example, for a real aperture antenna with 10° half power beamwidth (0.174 rad), the projection of the antenna beam on the ground (beamwidth length) will be about $0.174 \text{ rad} \times 1000 \text{ m} = 174 \text{ m}$ at a range of 1000 m.

A real aperture antenna that could achieve azimuth resolution on the order of meters at long range would be hundreds of meters long. For example, the half power beamwidth θ of an unweighted line antenna can be expressed by [5]

$$\theta \approx \frac{\lambda}{D} \tag{2.22}$$

where λ is the wavelength of the transmitted wave and D is the antenna length. If the beamwidth length of this antenna is 1 m at 10 km, the half power beamwidth of this antenna should be 1×10^{-4}. If the wavelength in (2.22) is 5 cm, the physical length of the antenna will be 500 m, which is not manageable.

The SAR achieves high azimuth resolution by synthesizing the Doppler information obtained at different observing angles to the object. Strictly speaking, the azimuth resolution in SAR is achieved by signal processing rather than by electromagnetics.

The SAR concept can be interpreted in a variety of ways, with each providing its own special insight into the principles. Two different views are given below to explain the principles of SAR.

The first view is from the aspect of an antenna array. The beamwidth of the array pattern of a broadside antenna array is inversely proportional to the array length, i.e. the longer the array, the narrower the beamwidth. The half power beamwidth of a broadside array with M elements can be expressed as [32] (Page 215 or 219)

$$\theta_{1/2} \approx \frac{2.782\lambda}{\pi M s} = \frac{2.782\lambda}{\pi a} \tag{2.23}$$

where λ is the wavelength, s is the element distance, and a is the array length. As shown by (2.23), the longer the equivalent aperture, the higher the azimuth resolution will be.

High cross range resolution can be achieved by the antenna array if enough elements are used. While the physical building of this kind of antenna is not realistic, there is no fundamental requirement that the elements need to be working simultaneously. A single element carried on a moving vehicle could serve in sequence the functions of each element of the array. As a single element moves, the data point obtained in each array element position are sampled and stored. The Doppler processing of the recorded data, after the traverse of all the array elements, can be performed to sharpen the azimuth beamwidth. The equivalent array length (e.g. several hundreds of meters) that a moving plat-

form (e.g. aircraft) travels through as a single radiation element is known as the 'synthetic aperture length'.

The process of synthesizing the aperture is shown in Figure 2.3. As there is no limitation on the length of this synthetic aperture, its equivalent azimuth beamwidth can be much narrower than that of a practical real aperture antenna. Therefore, the azimuth resolution can be significantly improved as long as the radar is highly coherent. The difficulties now lie in signal processing for azimuth signal compression (see Section 2.2.3.1), and motion compensation [33] (Page 403) to compensate the undesired movement of the aircraft caused by the air turbulence (in real cases, the plane will not fly in a straight line as shown in Figure 2.3).

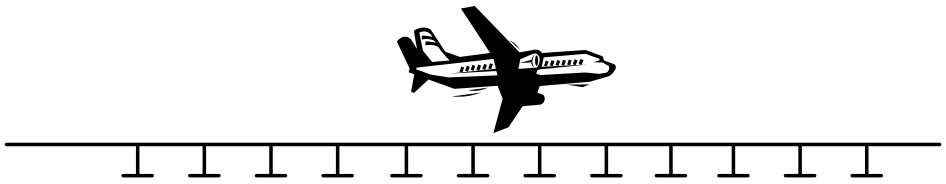

Figure 2.3 The form of synthetic aperture

Another view is given in terms of azimuth Doppler frequency analysis, as shown in Figure 2.4. In Figure 2.4, η is the azimuth time (slow time), R_0 is the closest distance between the radar and the target (closest approach distance), $R(\eta)$ is the instantaneous slant range at point η, and θ is the instantaneous incidence angle at η. The moving vehicle (e.g. aircraft) travels along the horizontal line with constant speed v. The instantaneous radial speed v_r changes continuously with the movement of the aircraft. To focus only on the azimuth resolution formation, a fixed frequency is assumed to be transmitted at each azimuth sampling position.

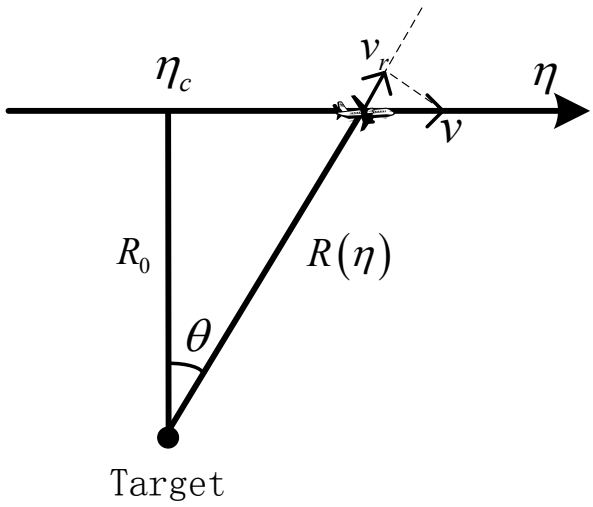

Figure 2.4 Azimuth Doppler interpretation

The Doppler frequency caused by the relative movement between the radar and target is

$$f_d = \frac{2}{\lambda}\frac{dR(\eta)}{d\eta} = \frac{2}{\lambda}v_r = \frac{2}{\lambda}v\sin\theta \tag{2.24}$$

where

$$\sin\theta = \frac{v\eta}{R(\eta)} = \frac{v\eta}{\sqrt{R_0^2 + v^2\eta^2}} \tag{2.25}$$

where η_c is assumed to be zero. One assumption to simplify (2.25) is to assume $R(\eta) \approx R_0$, which is only valid for narrow beamwidth and low squint angle (small θ) cases. Then the instantaneous Doppler frequency in (2.24) can be expressed as

$$f_d = \frac{2v^2}{\lambda R_0}\eta \tag{2.26}$$

Eq. (2.26) implies that the azimuth Doppler history for a target at R_0 is an LFM signal with constant FM rate, by which the azimuth high resolution could be achieved using pulse compression. The azimuth Doppler history will be more complex than the expression shown in (2.26) in wider beamwidth and higher squint angle situations, but the main component is still an LFM signal.

In either interpretation above, the transversal movement of the radar is the key to improve azimuth resolution. The high cross-range resolution is in fact obtained by post processing, which can be achieved in real time (the image of the observing area can be generated a few seconds after the aircraft flies over it) nowadays with the help of digital signal processing. The phase of the radar needs to be very stable and accurate to reveal the relative phase changes among different azimuth sampling positions. The quantization of the phase accuracy to meet a required performance specified is beyond the scope of this thesis.

An approximated azimuth resolution can be obtained by using (2.26). From (2.26), we know that the FM rate of the azimuth Doppler history is

$$k_a = \frac{2v^2}{\lambda R_0}. \tag{2.27}$$

The synthetic aperture time T_a is decided by the radar beamwidth and the velocity of the aircraft, which is

$$T_a = \frac{L}{v} = \frac{\lambda R_0}{Dv} \tag{2.28}$$

where L is the beamwidth length in meters at a specific range R_0, D is the physical length of the antenna in azimuth. An approximation of the unweighted line antenna

beamwidth $\beta_{bw} \approx \lambda / D$ [5] is used above. Therefore, the bandwidth of the azimuth LFM can be expressed as

$$Bw_a = T_a k_a = \frac{2v}{D} . \tag{2.29}$$

Thus the azimuth resolution at any range is

$$\rho_a = \frac{v}{Bw_a} = \frac{D}{2} . \tag{2.30}$$

Unlike the common antennas for which the beamwidth is constant, SAR has a constant resolution at different ranges, which means the equivalent beamwidth ($\theta_{eq} = \rho_a / R$) of SAR changes with the range R. This is because the synthetic aperture length for different distances is different according to (2.28).

2.2.2 SAR Configurations

There are three fundamental modes in SAR, stripmap mode, spotlight mode and scan mode. The stripmap mode is shown in Figure 2.5.

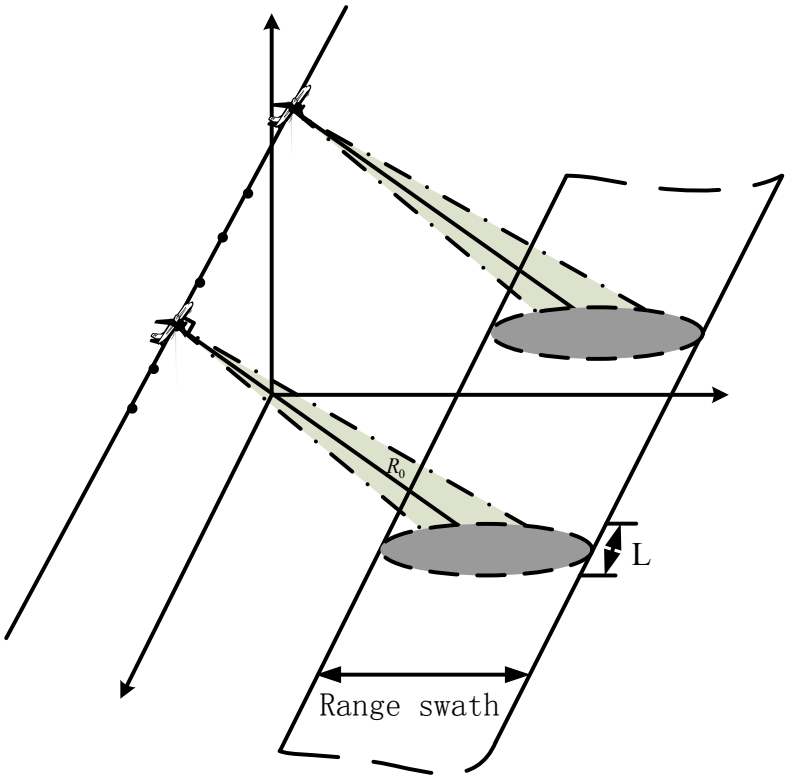

Figure 2.5 Stripmap mode

In stripmap mode, the antenna does not turn during flying and the projection of the antenna beam on the ground forms a strip. The synthetic aperture length L equals the azimuth projection length of the antenna beam. This is the basic and most commonly used mode in SAR.

Spotlight mode is used when higher azimuth resolution is required, such as in an ultra-high resolution SAR with centimeters resolution. The spotlight SAR mode is shown in Figure 2.6. The antenna keeps pointing to the same area during the whole data collecting duration. Mechanical structures such as gimbals or electronic methods such as phased arrays are used to steer the antenna beam and maintain its pointing direction. A longer synthetic aperture length than in the stripmap mode is obtained by steering the antenna beam to the same area, introducing wider azimuth signal bandwidth because the time

used to form the synthetic aperture is increased. However, spotlight mode requires precise control of the antenna pointing and strict motion compensation to generate high quality images.

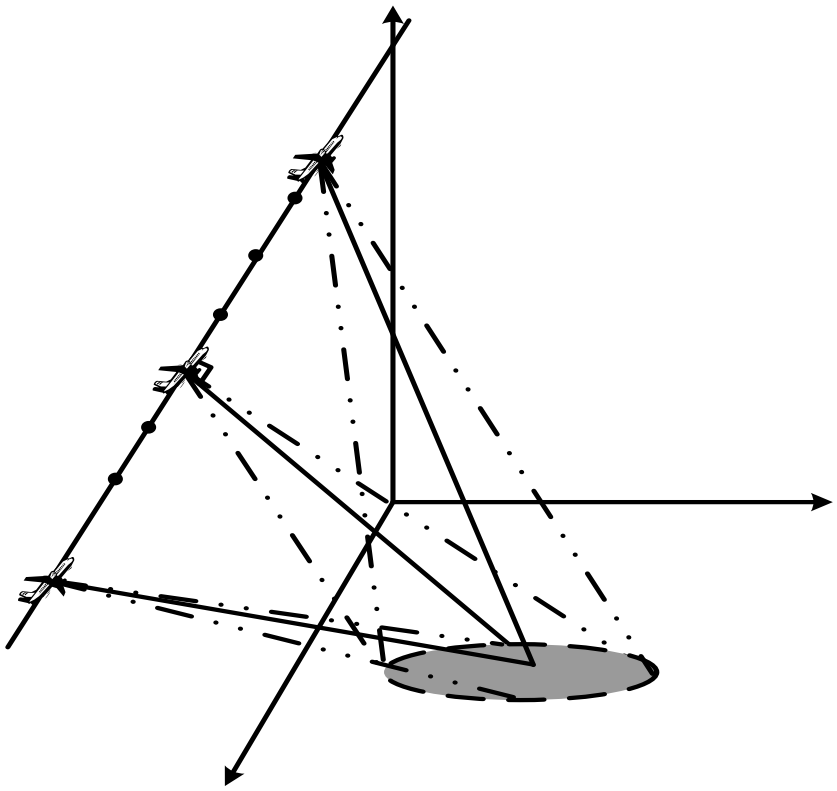

Figure 2.6 Spotlight mode

Scan mode increases the range swath by sacrificing azimuth resolution. The configuration is shown in Figure 2.7. The shadows in the figure show the footprints of the antenna beam. The antenna scans while the aircraft is moving so that a larger area can be observed. Since less time is used to observe a target than in the stripmap mode, then the azimuth resolution is lower. SPECAN algorithm [5] (Page 369) is the commomly used imaging algorithm for this mode.

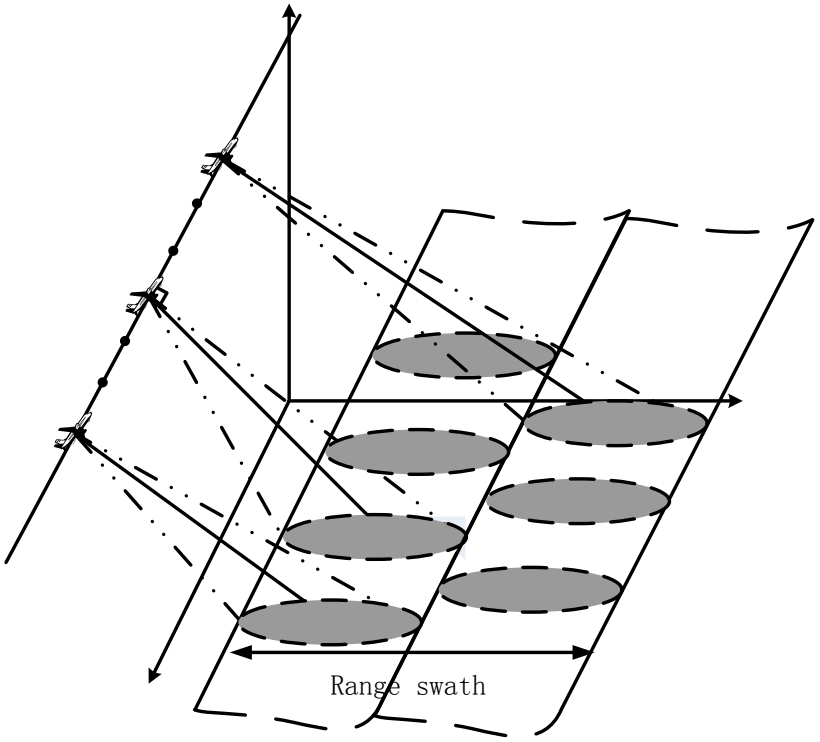

Figure 2.7 Scan mode

2.2.3 FMCW SAR Imaging Algorithms

Three different motions of the SAR platform occur during SAR data collection [33] (Page 55):

1. Motion between successive pulses;
2. Motion during the transmission and reception of a pulse;
3. Motion in the interval between transmission and reception of a pulse.

The targets are assumed to be stationary during SAR operation. The imaging of moving targets by SAR is another area which is beyond the scope of this thesis.

In pulse SAR, the pulse length is very short, hence the effect caused by the second and third categories of motions listed above, which are mentioned in this dissertation as

the in-pulse Doppler effect, are negligible. This is the so called start-stop (also known as stop-and-go) assumption [5] (Page 167).

Unlike pulse SAR, FMCW SAR continuously transmits and receives signals, thus the pulse length equals the PRT. This makes the start-stop assumption no longer valid, and hence all the three different motions mentioned above need to be considered [27], [34]-[36].

Another difference in FMCW SAR from pulse SAR is that dechirp-on-receive is normally not employed in pulse SAR. This is normally not employed in pulse SAR. Dechirp-on-receive decreases the ADC rate when the range swath is narrow. In pulse SAR, since the range swath is normally very wide, dechirp-on-receive does not have advantages over the orthogonal demodulation. The effect of the dechirp-on-receive on raw data is that it transforms the data to the equivalent range frequency domain by eliminating the chirp component in the received signal.

Due to the above two reasons, the signal model and imaging algorithms for FMCW SAR are different from those in the pulse SAR. Two different algorithms will be introduced below. The first is the range Doppler algorithm (RDA), which provides a clear and easy interpretation of SAR signal processing. The in-pulse Doppler effect is neglected for simplicity when presenting this algorithm. The second is the range migration algorithm (RMA), which is a more accurate algorithm than RDA and is preferred to be used in FMCW SAR signal processing. The correction of the in-pulse Doppler effect is also easier in this algorithm than in the RDA.

2.2.3.1 Range Doppler algorithm

RDA [37]-[39] was the first imaging algorithm developed for digital SAR signal processing during 1976-1978. The RDA has been modified and introduced into airborne FMCW SAR signal processing in [34]-[36]. As a concise and straightforward algorithm, RDA provides an easier insight into SAR signal processing. For easy understanding, the RDA introduced here is the basic RDA (i.e. still use the start-stop assumption), which does not consider the second range compression (SRC) and the in-pulse Doppler effect. Complex signals are used in this section for conciseness in mathematics even if the actual data acquired by the FMCW SAR are real valued. Methods of transforming real signals to complex signals have been presented in Section 2.1.1.

Assume the transmitted signal is

$$s_T(t,\eta) = rect_r\left(\frac{t}{T}\right) rect_a\left(\frac{\eta-\eta_c}{T_a}\right) e^{j\pi k t^2} e^{j2\pi f_0 t} \tag{2.31}$$

where t is range time (fast time) and η is azimuth time (slow time), and η_c is the zero azimuth Doppler time. The azimuth envelope is assumed to have a rectangular shape, though its precise form is similar to the mainlobe of a sinc function [5]. T_a is the synthetic aperture time. The amplitude of $s_T(t,\eta)$ is assumed to be 1. k is the FM rate and f_0 is the carrier frequency. The received signal is

$$s_R(t,\eta) = rect_r\left(\frac{t}{T}\right) rect_a\left(\frac{\eta-\eta_c}{T_a}\right) e^{j\pi k(t-\tau)^2} e^{j2\pi f_0(t-\tau)} \tag{2.32}$$

where

$$\tau = \frac{2R(\eta)}{c} = \frac{2}{c}\sqrt{R_0^2 + v^2(\eta-\eta_c)^2} \tag{2.33}$$

.

The geometry of deriving the expression for τ is shown in Figure 2.4. The SAR is assumed to look broadside. Expanding the square root in (2.33) by a Taylor series about $\eta = \eta_c$ and discarding the terms higher than the square of slow time (in RDA, the antenna beamwidth is assumed to be narrow, hence the terms higher than the square of slow time is very small and can be neglected [5] (Page 170)), we have

$$\tau \approx \frac{2}{c}\left(R_0 + \frac{v^2 (\eta - \eta_c)^2}{2R_0} \right). \tag{2.34}$$

The IF signal is the multiplication of (2.31) with the conjugate of (2.32), which is

$$s_{IF}(t,\eta) = rect_r\left(\frac{t}{T}\right) rect_a\left(\frac{\eta - \eta_c}{T_a}\right) e^{j2\pi f_0 \tau} e^{j2\pi k \tau t} e^{-j\pi k \tau^2}. \tag{2.35}$$

The last exponential term is known as the residual video phase (RVP), which can effect SAR signal processing when the imaging scene is larger [33] (Page 144). This term is normally removed before image generation [33] (Page 501). After RVP removal, we have

$$s_{IF}(t,\eta) = rect_r\left(\frac{t}{T}\right) rect_a\left(\frac{\eta - \eta_c}{T_a}\right) e^{j2\pi f_0 \tau} e^{j2\pi k \tau t}. \tag{2.36}$$

Substituting (2.34) into (2.36) and performing the range CTFT, we have

$$S_r(f,\eta) = T\text{sinc}\left[T\left(f - \frac{2k}{c} R_0 - \frac{2k}{c} \frac{v^2 (\eta - \eta_c)^2}{2R_0} \right) \right] rect_a\left(\frac{\eta - \eta_c}{T_a}\right) e^{j\frac{4\pi}{\lambda} R_0} e^{j\pi k_a (\eta - \eta_c)^2} \tag{2.37}$$

where

$$k_a = \frac{2v^2}{\lambda R_0} \quad \text{and} \quad \lambda = \frac{c}{f_0} \tag{2.38}$$

is the azimuth FM rate, which is the same as the one given by (2.27). An azimuth CTFT then brings the signal to the range-Doppler domain

$$S_{rd}\left(f,f_\eta\right)=Te^{j\frac{4\pi}{\lambda}R_0}\int \text{sinc}\left[T\left(f-\frac{2k}{c}R_0-\frac{2k}{c}\frac{v^2\left(\eta-\eta_c\right)^2}{2R_0}\right)\right] \cdot rect_a\left(\frac{\eta-\eta_c}{T_a}\right)e^{j\pi k_a\left(\eta-\eta_c\right)^2}e^{-j2\pi f_\eta\eta}\,d\eta \tag{2.39}$$

where f_η is the azimuth frequency. The principle of stationary phase (POSP) [33] (Page 423) can be used at this stage to solve the integral. In POSP, by letting

$$\frac{d\left[\pi k_a\left(\eta-\eta_c\right)^2-2\pi f_\eta\eta\right]}{d\eta}=0 \tag{2.40}$$

we have

$$\eta=\frac{f_\eta}{k_a}+\eta_c \tag{2.41}$$

.

Substituting (2.41) into (2.39), we have

$$S_{rd}\left(f,f_\eta\right)=T\text{sinc}\left[T\left(f-\frac{2k}{c}R_0-\frac{2k}{c}\frac{v^2f_\eta^2}{2k_a^2R_0}\right)\right]rect_a\left(\frac{f_\eta}{k_aT_a}\right)e^{j\frac{4\pi}{\lambda}R_0}e^{-j\pi\frac{f_\eta^2}{k_a}}e^{-j2\pi f_\eta\eta_c} \tag{2.42}$$

.

The sinc function in (2.42) shows that the signal has been compressed in range, and the peak of the sinc function along azimuth (azimuth trajectory of the point target) is a curve that varies with azimuth frequency f_η. The azimuth-dependent range shift is called range cell migration (RCM), which is

$$RCM=\frac{2k}{c}\frac{v^2f_\eta^2}{2k_a^2R_0} \tag{2.43}$$

.

This term needs to be removed by an azimuth frequency dependent range shift operation, i.e. the range cell migration correction (RCMC). In RDA, accurate RCMC needs to be realized by high orders of interpolation which is a time consuming operation. A faster and more accurate algorithm that only needs phase multiplication to realize precise RCMC is the chirp scaling algorithm (CSA) [23]-[25].

The rectangular function in (2.42) is the azimuth envelope, which implies that the range-Doppler signal has zero Doppler centre and width $k_a T_a = Bw_a$, where Bw_a is the azimuth bandwidth of the signal. The first exponential term is a constant; the second one is a quadratic function of f_η, which implies azimuth modulation; the last one is a linear function of f_η, which determines the azimuth position of the target after azimuth compression. The azimuth matched filter used to perform azimuth compression is

$$H_a\left(f_\eta\right) = e^{j\pi\frac{f_\eta^2}{k_a}}. \tag{2.44}$$

After azimuth compression and RCMC, (2.42) becomes

$$S_{rd1}\left(f, f_\eta\right) = T\text{sinc}\left[T\left(f - \frac{2k}{c}R_0\right)\right] rect_a\left(\frac{f_\eta}{k_a T_a}\right) e^{j\frac{4\pi}{\lambda}R_0} e^{-j2\pi f_\eta \eta_c}. \tag{2.45}$$

An azimuth inverse Fourier transform (IFT) then generates the image of the point target, which is

$$S_i\left(f, \eta\right) = A\text{sinc}\left[T\left(f - \frac{2k}{c}R_0\right)\right]\text{sinc}\left[Bw_a\left(\eta - \eta_c\right)\right] e^{j\frac{4\pi}{\lambda}R_0} \tag{2.46}$$

where A is the amplitude. As shown by (2.46), the range and azimuth positions of the target are determined by the two sinc functions. The 3 dB width of the range sinc func-

tion is $1/T$; and that of the azimuth sinc function is $1/Bw_a$, which is the same as the results of (2.29) and (2.30). Targets with different range and azimuth positions are now separated and correctly positioned. The exponential term in (2.46) is a constant phase, which does not influence the absolute value image.

The in-pulse radar movement is neglected during the above RDA derivation for a clearer view of SAR signal processing. This assumption is good for narrow beamwidth and low squint angle. For cases of high squint angle and wide beamwidth, the RMA introduced in the next section is a preferred imaging algorithm.

2.2.3.2 Range migration algorithm

The RMA had its roots in seismic signal processing and was introduced into the SAR field around 1980s [40]-[42]. Similar to SAR, in seismic monitoring, a linear array of geophones is placed on the surface of the earth to detect geological features under the ground. Each of the seismic sensor position could be viewed as an azimuth sampling point in SAR imaging. Therefore, the application of RMA in SAR signal processing is very straightforward.

The original RMA applied in SAR signal processing was given in the wavenumber domain [40]. Therefore, the RMA is also named the wavenumber algorithm. The frequency domain form that derived from the signal processing view-point is given in [5]. For the reasons of simpler analysis of the IF signal used in the dechirp-on-receive FMCW SAR, the derivation below is also given in the frequency domain, even though most RMA algorithms in the literature are given in wavenumber form. A detailed derivation of RMA in wavenumber domain can be found in [33] (Page 401).

RMA is well accepted as one of the most accurate SAR imaging algorithms because it does not make any approximations about the instantaneous slant range expression shown in (2.33), which is approximated in most other processing algorithms. Because the RMA processes data in the two dimensional frequency domain, the special in-pulse Doppler effect (this effect is normally neglected in pulse SAR) in FMCW SAR, which is neglected in Section 2.2.3.1, is also considered in the following derivation.

Starting from the RVP removed signal, which is

$$s_{IF}\left(t,\eta\right)=rect_r\left(\frac{t}{T}\right)rect_a\left(\frac{\eta-\eta_c}{T_a}\right)e^{j2\pi f_0\tau}e^{j2\pi k\tau t} \tag{2.47}$$

where

$$\tau=\frac{2R\left(\eta,t\right)}{c}\approx\frac{2}{c}\sqrt{R_0^2+v^2\left(\eta+t-\eta_c\right)^2}\ . \tag{2.48}$$

The derivation of (2.48) is given in Appendix A.

Since the dechirp-on-receive has readily transformed the signal to its equivalent range frequency domain, then only one azimuth FT is required to obtain the two dimensional frequency expression, which is

$$S\left(t,f_\eta\right)=rect\left(\frac{t}{T}\right)\int rect_a\left(\frac{\eta-\eta_c}{T_a}\right)e^{j2\pi f_0\tau}e^{j2\pi k\tau t}e^{-j2\pi f_\eta\eta}d\eta\ . \tag{2.49}$$

The POSP can be used to obtain an approximation of (2.49). Letting

$$\frac{d\left(2\pi f_0\tau+2\pi k\tau t-2\pi f_\eta\eta\right)}{d\eta}=0 \tag{2.50}$$

we have

$$\eta = \frac{cf_\eta R_0}{2v^2\left(kt+f_0\right)\sqrt{1-\dfrac{c^2 f_\eta^2}{4v^2\left(kt+f_0\right)^2}}} + \eta_c - t \tag{2.51}$$

Substituting (2.51) into (2.49), we have

$$S\left(t, f_\eta\right) = rect\left(\frac{t}{T}\right) rect_a\left(\frac{f_\eta}{k_a T_a}\right) \exp\left(j\Phi\left(t, f_\eta\right)\right) \tag{2.52}$$

where

$$\Phi\left(t, f_\eta\right) = \frac{4\pi R_0}{c}\sqrt{\left(f_0+kt\right)^2 - \frac{c^2 f_\eta^2}{4v^2}} + 2\pi f_\eta t - 2\pi f_\eta \eta_c \tag{2.53}$$

The approximation

$$\eta = \frac{cf_\eta R_0}{2v^2\left(kt+f_0\right)\sqrt{1-\dfrac{c^2 f_\eta^2}{4v^2\left(kt+f_0\right)^2}}} + \eta_c - t \approx \frac{cR_0}{2v^2 f_0\sqrt{1-\dfrac{c^2 f_\eta^2}{4v^2 f_0^2}}} f_\eta + \eta_c \approx \frac{1}{k_a} f_\eta + \eta_c \tag{2.54}$$

is used in the azimuth envelope $rect_a$ in (2.52) for clarity. k_a is the same as defined in (2.38). As discussed in Section 2.1.1, the envelope is not sensitive to small changes in its parameters, so this approximation holds. In fact, the azimuth envelope is neglected in most SAR signal model derivations because it does not impact the signal processing.

The second term of (2.53) is the in-pulse Doppler effect caused by the continuous movement of the aircraft during the transmitting and receiving of the signal. This term can be removed by multiplying (2.53) with the phase

$$H_d = e^{-j2\pi f_\eta t} \tag{2.55}$$

The difficulty of SAR signal processing lies in the square root of (2.53), which represents the coupling of range and azimuth. The most common way of decoupling is to express the square root by Taylor expansion and keep the first several terms (normally the first three term because in narrow beamwidth and low squint cases, the higher order terms are very small) in the series. As the SAR configurations push the parameters beyond the validity of the Taylor approximation, the algorithms based on the Taylor expansion does not focus the SAR images well. This is because more terms in Taylor expansion need to be kept to better approximate the square root of (2.53) when the SAR parameters are in extreme cases. However, when too many terms are taken, it will be very complex (or even not possible) to derive a closed form of SAR signal that can be used for signal processing.

The way that RMA processes the square root of (2.53) is to perform a variable substitution instead of using approximations. Before variable change, RMA first uses a reference function multiplication (RFM) operation to focus the point at the reference range. The reference phase is

$$\Phi_{ref}\left(t, f_\eta\right) = -\frac{4\pi R_{ref}}{c}\sqrt{\left(f_0 + kt\right)^2 - \frac{c^2 f_\eta^2}{4v^2}} \tag{2.56}$$

where R_{ref} is the reference range, which is normally chosen to be the centre range of the imaging scene. Eq. (2.55) and (2.56) are then multiplied with (2.53), and the result phase is

$$\Phi\left(t, f_\eta\right) = \frac{4\pi\left(R_0 - R_{ref}\right)}{c}\sqrt{\left(f_0 + kt\right)^2 - \frac{c^2 f_\eta^2}{4v^2}} - 2\pi f_\eta \eta_c \tag{2.57}$$

.

The points at reference range now have constant phase and thus could be well focused. Then the variable substitution is performed, which is

$$\sqrt{\left(f_0+kt\right)^2-\frac{c^2f_\eta^2}{4v^2}}=f_0+kt_1 \tag{2.58}$$

where t_1 is the new time variable. This is the so called Stolt mapping [5] because this variable change corresponds to a re-mapping of the time axis. For different azimuth frequency f_η, the mapping for the time variable is different. Therefore, the RCM and the range-azimuth coupling are removed.

After the Stolt mapping shown by (2.58), the phase of (2.57) is a linear function of the new time variable t_1, which implies the range from the reference one. Then a range FT and an azimuth IFT will focus the target.

Although no approximation is made in RMA about the square root, there are two factors that will affect the accuracy of RMA.

The first is the variable substitution. In digital signal processing, the change of variable in (2.58) has to be achieved by interpolation (normally the sinc function interpolation), which cannot be perfectly accurate. The interpolation accuracy could be increased by using a longer kernel function (sinc function with more points) and perform higher order interpolation, but this will significantly increase the computational load and data size. Thus a tradeoff needs to be made between the accuracy and the efficiency. However, this accuracy does not decrease with the change of SAR parameters, which means the method will have the same accuracy in both low squint and high squint situations.

The second factor is that the RMA cannot adapt to changes of velocity. In the case of satellite SAR, the velocity is different at different ranges (the speed can vary by 0.15%

over a swath of 50km) [5]. Thus a reference velocity should be used in the RFM shown in (2.56). In this case, the result in (2.57) does not hold because the square roots in (2.53) and (2.56) are not the same. Therefore, an approximation of constant velocity needs to be made for all ranges. But as the speed variation is very small in both space-borne and air-borne cases [5] (Page 343), the change of velocity with range can be neglected.

The two problems discussed above only slightly affect the accuracy of the algorithm, thus the RMA is still the most accurate imaging algorithm suitable for wide beamwidth and large squint angle. The drawback of RMA is that it requires a significant amount of interpolation (sinc function interpolation) to perform the Stolt mapping, which is very time consuming [22].

CHAPTER 3. A CUSTOMIZED FMCW SAR SYSTEM

3.1 Background and Literature Review

The development of the modern solid-state devices has made possible the implementation of small and cost effective FMCW SARs for short range operations. Compared with traditional pulse SAR system which is about 30–70 kg and consumes more than 500 W power [8], an FMCW SAR can now weigh several kilograms and consume less than 50 W power, which makes it more applicable to fly on a small UAV from the weight and power consumption perspective. Several experimental FMCW SAR systems have been developed and tested successfully [8]–[16].

In 2004, a millimeter wave FMCW radar system and several experimental results were reported [10]. The radar works at 35 GHz centre frequency, and has 1 m (range) by 1 m (azimuth) resolution. The transmitted power is 18 dBm, and the maximum range is 730 m. The PRF is 1000 Hz and sawtooth modulated LFM signal is employed.

MISAR [8], [11] is a 35 GHz centre frequency FMCW SAR system developed in 2002 with resolution 0.5 m by 0.5 m. The radar uses dual antennas and dechirp-on-receive methods. The weight of the radar system is about 4 kg, and the onboard volume is about 10 liter. The maximum imaging range is 4 km and the onboard power consumption is 100 W. The range swath is 500–1000 m. The SAR system is designed to fly on the small UAV LUNA, and has real time data link to transmit data and images. High quality and high resolution images obtained by this FMCW SAR were reported in [11].

In 2005, a small FMCW SAR system μSAR [9] was developed at Brigham Young University (BYU). The successful development of this SAR system demonstrates the possibility of building low cost and high resolution FMCW SAR systems. The radar

works at C-band (centre frequency 5.56 GHz) and has a 1.875 m range resolution (bandwidth 80 MHz). The transmitted power is 0.5 W. The system was built by customized micro-strip circuit boards and some off-the-shelf components. Dechirp-on-receive and dual antennas were used in this SAR system. The antennas are patch array micro-strip antennas and the weight of the whole system is less than 2 kg. The transmitted signal uses TM-LFM waveform. Some experimental results can also be found in [12], [43].

Based on the successful development of the μSAR system, another FMCW SAR system, MicroSAR, was developed by BYU around 2008 [13]. The system works at C-band and has the maximum range resolution of 1.25 m. The transmitted power is 30 dBm and the imaging range is about 3 km. The whole system weighs about 3.3 kg. The transmitted signal used in this system is SM-LFM signal that enable a higher PRF [13].

MIRANDA35 [14], [15] is another FMCW SAR system developed in Europe around 2010. The radar works at 94 GHz, and has a maximum resolution of 0.3 m by 0.3 m. The transmitted signal bandwidth is 600 MHz. The system uses sawtooth modulation and the operational range is about 4 km. Direct digital synthesizer (DDS) is used to generate the linear FMCW signal and the whole front-end is synchronized to a very stable master oscillator source, which ensures the phase stability both inside one chirp and over a time series of consecutive chirps. Several successful experiments have been conducted on small manned aircraft [14].

A multichannel FMCW SAR was developed recently [16] designed to work on X-band with a maximum range resolution of 10-15 cm and maximum range of 5 km. The multichannel technique is a method commonly used to generate ultra-wide bandwidth over one gigahertz. The whole wide bandwidth is divided into several sub-bands and

transmitted on stepped carrier frequencies. The sub-bands are then received and synthesized during signal processing. The system weights about 6 kg and consumes 75 W of power.

The review of the above systems provides a brief overview of the weight, power and range of modern FMCW SAR systems. The transmitted power is normally about 0.5 W–1 W and the imaging range is limited to several kilometers. High resolution and light weight are the common advantages of all the systems, while the limitation is the imaging range.

This chapter first introduces a SF radar system, which is the start of my research. While the original purpose of building the SF radar is to use the radar as an altimeter for height measurement of the UAV, the data recording part is designed for SAR operation. However, for the reasons discussed in Section 3.2.4, this SF radar is not suitable for SAR uses. However, the experience and lessons learnt from the radar altimeter helped the development of a fully customized FMCW SAR system for ground imaging described in Section 3.3 to 3.5. The radar design considerations, parameters, and structures are introduced. Experimental results are then given. A summary for this chapter is given in the last section.

3.2 Stepped Frequency Altimeter

As a small and inexpensive radar system, SF radar has been widely used for distance measurements when a high update frequency is not required. The principles of stepped frequency technique is introduced in Section 2.1.2. A normal SF radar system is composed of two parts. One is the SF sensor head and the other is the peripheral circuit.

The structure of the simplest SF radar head includes VCO, mixer, and antenna(s). The VCO receives the outer linear control voltage to generate a series of stepped frequencies, which are transmitted one by one to form a sweep burst. A specific frequency signal is received after reflection and mixed with its transmitted copy to generate a constant voltage (the IF signal). The peripheral circuit then takes one sample of the IF singal in each frequency step and stores it. All the samples in one sweep burst form the high resolution IF signal.

3.2.1 SF Radar Head

Many SF sensor heads are now available on the market. Two of them were tested during the development of the SF radar altimeter. The first one is the RS3400X/K from SIVERSIMA [44], [45], which is shown in Figure 3.1.

Figure 3.1 SIVERSIMA RS3400X

The top small board with a SMA connector is the radar sensor head and is 55 mm x 38 mm x 9.4 mm in size. It works at X-band and the maximum output power is 5 dBm. The SMA port is used to connect to the antenna for transmitting and receiving signals.

The bigger board at the bottom is the mother control board. The mother board uses a RS232 port to communicate with a computer. The sensor module is connected to the

mother board with 42 pins on its bottom side. The whole radar system is controlled by software on the computer through the mother board. All the working parameters are first set in the computer and then sent to the mother board. The mother board samples and stores the IF data. However, only the IF data from the last burst can be stored and recorded by the computer. A customized board with functions similar to the mother board needs to be built if the radar needs to work standalone.

The other sensor head is the SRR series [46] shown in Figure 3.2. The radar works on K-band and the transmitted power is 10 dBm. A linear voltage should be provided to the sensor head to control the transmitted frequency.

Figure 3.2 SRR series radar head

The whole radar system is composed by a gunn oscillator (VCO), a polarizer diplexer, a mixer and an antenna. The VCO generates a fixed frequency signal which is defined by the input control voltage. The signal is sent through the diplexer to the antenna for transmission and to the mixer in the receive channel as the reference signal. The received

signal goes through the diplexer to the mixer and mixes with the reference signal to generate the IF signal, which is available on one pin of the sensor head. The working of the radar is fully controlled by peripheral circuits.

The second sensor head (SRR series) has simpler interface and larger output power than SIVERSIMA RS3400X, hence this second sensor head was used to build the altimeter.

3.2.2 Peripheral Circuits

The composition of the peripheral circuits includes three parts. The first part is the radar control section that generates the linear voltage. This function is realized by the microcontroller board mbed NXP LPC1768. The linear voltage generated is from 0 V to 3 V, which needs to be amplified and offset to the desired values.

The second part is the small signal amplifier. The output from the IF pin of the radar head is very weak and needs to be amplified before sampling. Because the IF signal from the sensor head in every frequency step is a constant voltage, an amplifier circuit composed by normal op-amps can finish the tasks.

The last part is the ADC and data record unit. For easy and fast realization of this function, a TMS320VC5505 evaluation board, which has built-in ADC and supports SD card writing, is used.

3.2.3 Radar System

The structure diagram of the SF radar altimeter is shown in Figure 3.3.

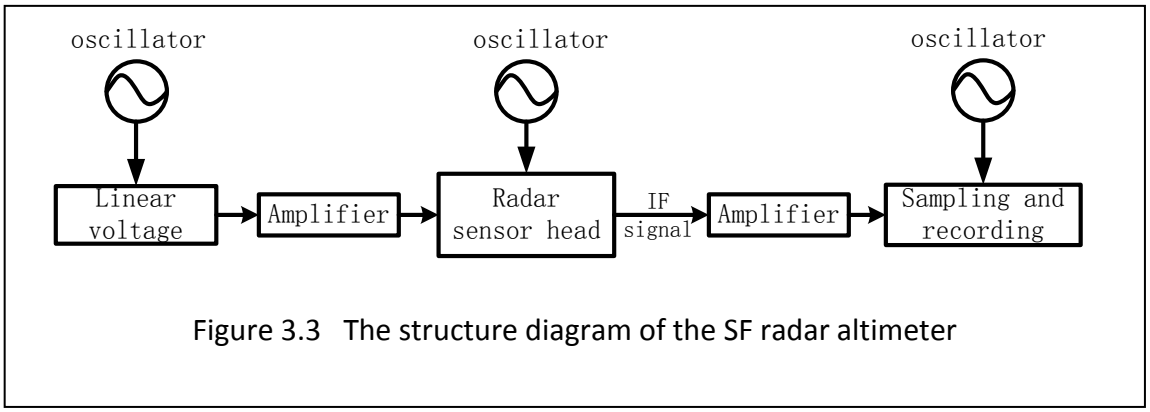

Figure 3.3 The structure diagram of the SF radar altimeter

The final system is shown in Figure 3.4. On the top left of the figure is the SRR series K-Band SF radar head. The small board on the left bottom is the control board, which includes the mbed NXP LPC1768 system, one RC filter and two amplifier circuits. 0-3 V linear voltage is first generated by the mbed system and then amplified and offset by one

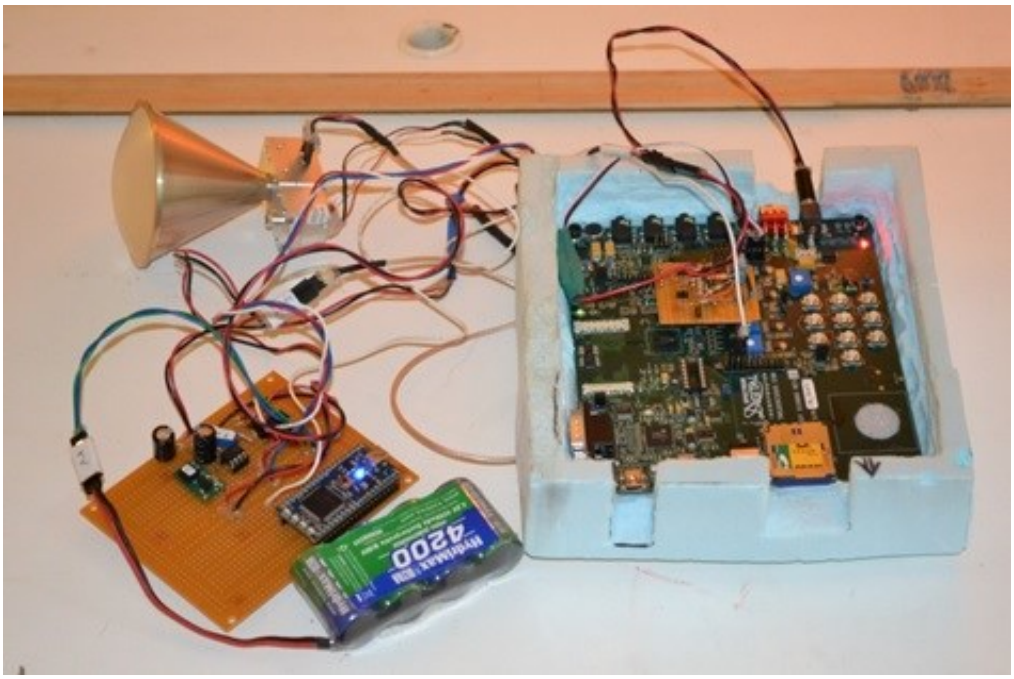

Figure 3.4 The SF radar altimeter

amplifier circuit to 7-17 V, which is used to control the SF radar head. The IF signal from the sensor head has a small offset voltage, which is removed by the high pass RC filter before amplification by the other amplifier circuit on the small board.

The amplified IF signal is then sent to the TMS320VC5505 evaluation board shown on the right side of Figure 3.4, where the signal is offset and amplified again before sampling. The sampled data are then recorded on a 256 Mbytes SD card. The whole system is less than 1kg and powered by a 4.8 V battery.

3.2.4 Discussion

The SF radar works for simple range measurement but cannot work as a SAR. There are several reasons for this:

First, due to the working principles of SF radar and the clock speed limitation of the mbed system, the PRF of the SF radar is less than 100 Hz, which is not sufficient for SAR operation. The continuous LFM radar needs to be used instead of the discrete SF radar.

Second, the ADC and SD card writing are all controlled by software, which limits the speed and accuracy. The SD card is controlled through several GPIO (general purpose input output) ports by software, which limits the speed of SD card writing. Therefore, only the old SD card standard is supported by the evaluation board. The ADC is also controlled by software. The ADC sampling is triggered by the software every time a sample needs to be taken. Since the software also performs other tasks, the clock speed of the chip is not sufficient to support simultaneous high speed sampling and recording. Real time processing is also impossible.

Third, the coherence of the radar is poor. As can be seen from Figure 3.3, three different oscillators working separately are used in the system. Therefore, it is impossible to obtain high synchronization in this radar system. For example, the mbed system of the SF radar could only be operated at milliseconds level, which is not sufficient for high accuracy applications. In a highly coherent, high PRF and wideband radar system, a lot of operations are performed according to the period of the clock, so the system should be synchronized to the clock level (nanoseconds).

Fourth, there is no access to the radio frequency (RF) signal because it is all enclosed in the sensor head. The SAR image is only recognizable when the antenna beam footprint on the ground covers a large enough area in which the recognizable ground objects are included. Therefore, a power amplifier is normally required in the transmission channel to increase the radar range. This is impossible in this SF radar because the generated signal is fed directly to the antenna inside the radar head.

Due to the above reasons and other commercial reasons mentioned in Section 1.1, a SAR system should be designed and built as a whole system.

3.3 FMCW SAR Design Considerations

3.3.1 Sampling Frequency

SAR is a two dimensional imaging system. Therefore, two factors: range sampling frequency and cross-range sampling frequency, need to be considered. Nyquist–Shannon sampling theorem should hold in both dimensions.

Range sampling is the sampling of a radar signal in the traditional sense. For a signal with bandwidth Bw, the lowest sampling rate is $2Bw$ for direct (one channel) demodula-

tion and Bw for orthogonal demodulation. In a dechirp-on-receive demodulation system, the sampling frequency is determined by the FM rate and range swath. As shown by (2.9), the frequency of the IF signal for a target at range R_0 is $k\tau$. Therefore, for an FMCW SAR system designed to work with the maximum range swath $R_{\max}$ (or maximum range if the reference chirp is zero time delayed), the required ADC sampling rate is given by

$$f_s = 2 \cdot k \frac{2R_{\max}}{c} \quad . \tag{3.1}$$

Higher frequencies than f_s should be eliminated by a low pass filter before sampling, or else they will wrap back to the sampled signal as false targets. Eq. (3.1) also explains why dechirp-on-receive is not employed in pulse SAR since both k and $R_{\max}$ are normally large. Assuming the transmitted signal of a pulse SAR has 600 MHz bandwidth and $6\ \mu s$ pulse length, the FM rate is $k = 1 \times 10^{14}$. According to (3.1), the sampling rate needed for a range swath of 400 m in dechirp-on-receive will exceed the Nyquist rate required in orthogonal demodulation. The range swath of pulse SAR is normally several kilometers, which makes it not worth to use dechirp-on-receive demodulation.

The azimuth sampling rate, i.e. the PRF, is determined by the azimuth signal bandwidth. As shown by (2.29), the azimuth Doppler bandwidth is $2v/D$. To meet the Nyquist sampling criterion, the PRF is

$$PRF > \frac{2v}{D} \Rightarrow \frac{PRF}{v} > \frac{2}{D} \quad . \tag{3.2}$$

where D is the antenna length in azimuth direction. PRF/v corresponds to azimuth maximum wavenumber, and always appears in pair in SAR signal processing. Therefore, this value is kept constant in most SAR systems. Eq. (3.2) shows that a high PRF is normally

necessary in SAR configurations. For example, for a SAR system with 100 m/s velocity and 0.2 m antenna, we need $PRF \geq 1000Hz$. This explains why high toggling speed components are required in SAR systems, especially when the antenna is small.

3.3.2 RF Signal Generation

Since the cross-range resolution of SAR is achieved by analyzing the azimuth Doppler phase history, the coherence of the radar system is important. RF signal generation is the most important factor affecting the coherence of the SAR system.

The traditional way to generate the LFM signal is to use a VCO as the determining device for the waveform. However, a wide tuning range of the VCO leads to low phase coherency [15]. Techniques such as phase locked loop (PLL) are necessary to overcome this problem. Several developed FMCW SAR systems using VCO as LFM signal generator have encountered the nonlinearity problem [34], in which the output frequency of the VCO is not strictly a linear function of the input voltage. One way of solving the problem is to measure the nonlinearity directly and compensate the control voltage. Another way is to add a delay line into the SAR system, through which a copy of the transmitted signal with accurately known time delay is directly demodulated by dechirp-on-receive. Then estimation algorithms could be used to estimate and compensate the nonlinearity during the processing of the data [34], [47].

Another way for high quality LFM signal generation is to use DDS [48], [49]. DDS has certain advantages over VCO such as better frequency agility, higher phase coherency, and lower phase noise, which makes it a better option for generating the SAR LFM signal. However, as a sampling system, the clock frequency of the DDS must be at least twice the highest frequency of the generated signal. Moreover, as the operation of the

DDS is controlled by the variables stored in the registers, either serial or parallel communication should be used to program the DDS. The phase stability of the DDS is greatly influenced by the stability of the clock source, thus a highly stable oscillator must be used. Another shortcoming of DDS is the high spurs due to the truncation effect, which should be compensated by an inverse sinc filter [49]. The output from DDS also comes with a great amount of harmonics, which need to be eliminated by filters. Therefore, the implementation of the DDS is always accompanied by harmonics elimination filters.

3.3.3 System Synchronization

Besides high coherency, wide bandwidth and high PRF are two other requirements of SAR. The operation of the system should be synchronized to the clock level (normally nanoseconds or microseconds) for better performance. One example is the clock synchronization of the DDS and the ADC. If the DDS is started by a rising edge of the clock signal, the ADC should also be triggered by this edge or another edge that has constant time delay to this one. If the system is not synchronized to the clock level, the ADC may start after a random delay every time the DDS starts a new pulse. Since the phase varies very rapidly in SAR (a typical value of FM rate is about 10^{14} Hz/s in pulse SAR and 10^{11} Hz/s in FMCW SAR for 1 m resolution), even small time differences in starting the analog to digital conversion among different pulses can cause large phase differences in the sampled data. As a result, the initial phases of the sampled data from different pulses are random even though they are the same. This will obviously influence the image quality of the SAR system. Another example is the clock synchronization of the DDS and microcontroller. The DDS used by the FMCW SAR does not have a stop frequency register. Only the starting frequency and FM rate can be set. Therefore, the bandwidth of the

transmitted signal is controlled by the PRT, i.e. the sweeping time of the DDS. If the microcontroller and the DDS clocks are not synchronized, the sweeping time will be different in each PRT, which makes the bandwidth of the transmitted signal different among different PRTs.

The best way to increase the system synchronization is to use only one stable oscillator to derive all the clocks needed by different parts. As the original clock from an oscillator is an analog sinusoidal signal while the digital parts require rectangular-like signal, the transformation between analog signal and digital signal should also be considered. The use of high-speed comparators is a viable choice to perform this task.

3.3.4 Data Sampling and Recording

The wide bandwidth and high PRF of SAR system requires high speed data recording media and high speed and stable ADC.

In high resolution pulse SARs with resolution on the orders of centimeters, the ADC rate is normally several hundred mega-samples per second. This could easily raise the ADC output data rate to more than 50 Megabytes per second even though only a short pulse needs to be sampled in every PRT. Therefore, the data recording section of pulse SAR systems should be extremely fast.

In FMCW SAR, the data rate is decreased by dechirp-on-receive technique. The ADC sampling rate is typically only several mega-samples per second, and the data rate is about several megabytes per second, which can be handled by some small commercial recording medias (for example, a class 10 SD card).

The stable operation of ADC is also important. A stable ADC can provide an accurate definition of the signal frequency, which is important in the case where frequency

analysis is important. If the ADC rate changes during sampling, it will be hard to analyze the signal in frequency domain. Therefore, a better way to trigger ADC is by hardware, where once the ADC starts, no software interference is needed.

3.4 System Details

As indicated by the above discussions, a high performance FMCW SAR system requires custom design and development to ensure the synchronization and coherency of the system. It cannot be readily realized by assembling the existing off-the-shelf products (such as radio sources, radar heads).

3.4.1 Structure

The simplified block diagram of the customized FMCW SAR system built in this research is shown in Figure 3.5.

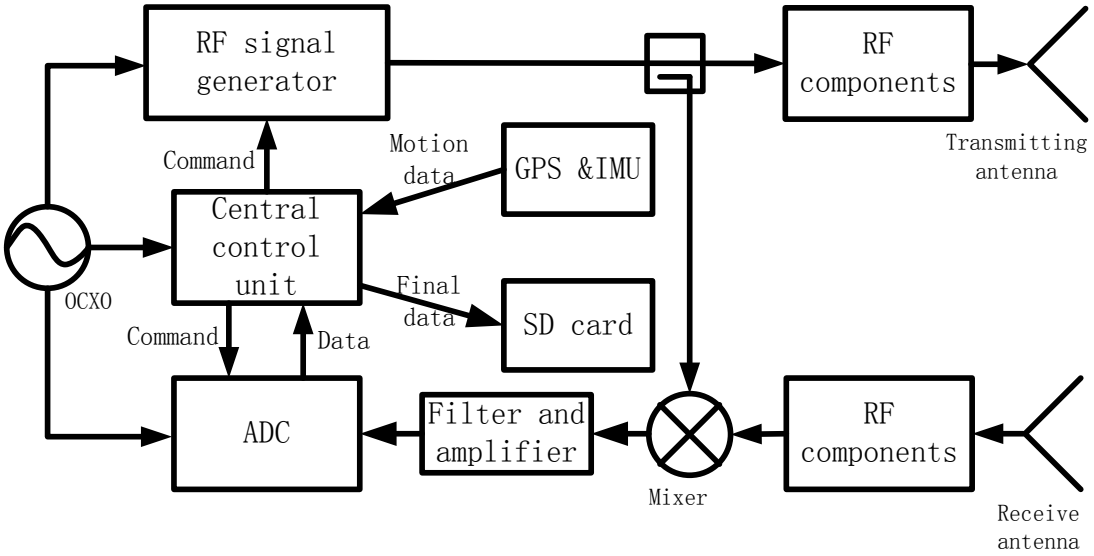

Figure 3.5 The simplified FMCW SAR block diagram

The whole system uses a 100 MHz premium OCXO as the clock source for different units. As the clock frequencies required by different parts are different, several frequency multipliers and dividers are employed in the system for clock generation.

One important feature of this FMCW system is that only one microcontroller is used to perform the entire control, data recording and calculation tasks. Large amounts of data can now be handled and organized inside the central control chip directly, which avoids the delay between different processing stages and increases the data processing speed.

The DDS is programmed by the central control unit (CCU) through serial communication port. The CCU also controls the PRF and the bandwidth of the radar system. At the beginning of each pulse, the CCU starts the DDS with the working parameters. The DDS then operates according to the parameters until the next command is issued by the CCU.

The generated RF signal is filtered and amplified and then sent to the transmission antenna. A part of the RF signal is coupled and sent to the receive channel mixer as the reference signal. The received echo is first filtered and amplified and then mixed with the reference signal to generate the IF signal, which is then filtered and amplified before being sampled by ADC.

A successive approximation ADC with 3 Msamples/s maximum speed and 12 bit accuracy is used to sample the IF signal. The ADC is triggered by the CCU at the beginning of each pulse. The sampled data is then sent to CCU through DMA (direct memory access).

The GPS and IMU (inertial measurement unit) can be used on the SAR platform to record the motion information of the SAR system for motion compensation. They are designed to connect to the SAR by two I^2C ports. The motion data are then merged with the

sampled IF data in the CCU to form the final raw data. The construction of the GPS and IMU part has not been undertaken and is not part of this dissertation.

The final data are then written into a class 10 SD card by 4-bits parallel writing through DMA. Interruption is used because the data writing has the lowest priority in the entire radar operations. The recorded raw data in the SD card will be read and processed by a computer after the data collection.

3.4.2 System Parameters

C-band radar system is a compromise of UAV application, size of antenna, design difficulties, microwave components and instruments availabilities. A wide range of C-band microwave components, such as filters, amplifiers, frequency multipliers and mixers, are available in the market. Also, the C-band FMCW radar can be made sufficiently small for UAV operation. Therefore, the centre frequency of the FMCW SAR is chosen to be around 5 GHz (C-band).

The parameters of the finished customized FMCW SAR system are shown in Table 3.1. The centre frequency of the radar system is 5545–5600 MHz, which is controlled by the DDS. The maximum transmitted signal bandwidth is 150 MHz, corresponding to 1 m range resolution. PRF is changeable between 1 Hz and 2000 Hz. This is because in SAR system, the value of PRF / v (see (3.2)) is normally constant. Therefore, the PRF needs to change with the variation of the radar speed v. Either TM or SM LFM waveform can be generated as the transmitted signal.

The SAR system is designed to be mounted on a UAV, thus the power of the system is provided by a battery. The DC input voltage range can be from 12 V to 36 V. The sys-

tem consumes 1.5 A current when the input voltage is 18 V, thus the power consumption of the whole system is about 27 W. The transmitted power is 0.5 W.

Table 3.1 FMCW SAR parameters

Parameters	Value	Unit
Center frequency	5545-5600	MHz
Bandwidth	150	MHz
Maximum range	3	km
PRF	1–2000	Hz
Transmitted power	0.5	W
Supply voltage	12–36	V
Power consumption	27	W
ADC rate	3	Msamples/s
ADC accuracy	12	Bits
Maximum data recording speed	25	Mbytes/s
CCU core clock speed	400	MHz
Waveform	Triangular or sawtooth modulated	

The designed maximum range of the radar is 3 km. According to (3.1), the maximum operational range is also limited by the sampling speed. Leaving aside the factor of the transmitted power, the maximum imaging range is related to the PRF and sampling rate f_s by the following equation

$$R_{\max} = \frac{cf_s}{4Bw \cdot PRF} . \tag{3.3}$$

According to (3.3), the maximum range will be shorter than 3 km when the PRF is higher than 500 Hz.

3.4.3 System Considerations

3.4.3.1 Waveform selection

Sawtooth modulated and triangularly modulated signal are the two commonly used LFM waveforms in radar. In FMCW techniques, as the transmitting and receiving are continuous, SM-LFM CW signal may cause problems if there is no time delay between the successive sweeps.

In SM radar, the baseband LFM signal needs to jump from the end frequency to the starting frequency immediately after the next sweep starts. This return time is normally on the order of nanoseconds. Since the bandwidth is normally very wide in SAR, the instantaneous frequency change in the RF generator can be very large. This instantaneous jump of the entire bandwidth can cause ring effect in the radar system.

Figure 3.6 shows the ring effect when SM signal is used in the customized FMCW SAR system. The antennas were pointed to the sky during the test, thus no signal should appear in the IF signal. The parameters used for this test are shown in Table 3.2.

Table 3.2 Ring effect test parameters

Parameters	Value	Unit
Bandwidth	150	MHz
PRF	500	Hz
ADC rate	1	Msamples/s
Waveform	Sawtooth modulated	

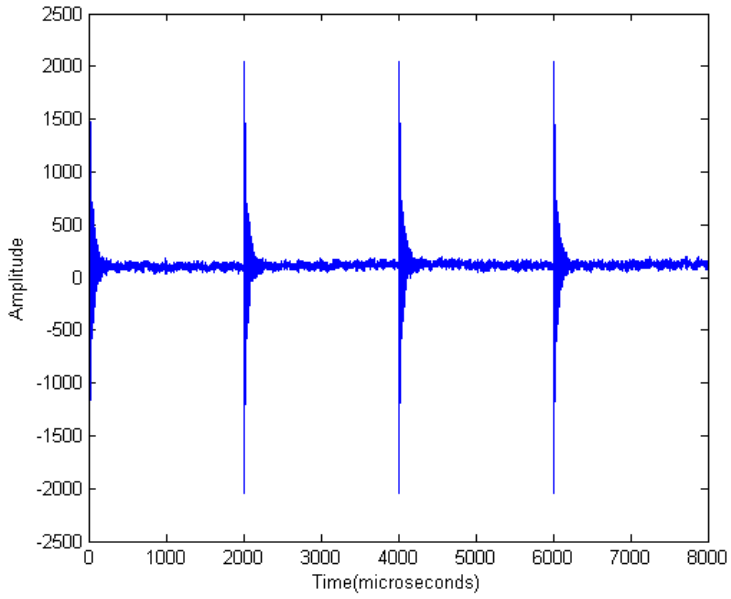

Figure 3.6 Ring effect when using SM signal

As can be seen from Figure 3.6, the ring effect appears at the beginning of each pulse (2ms, 4ms and 6ms). Closer view of the ring effect in time and frequency domain is given in Figure 3.7 (time) and Figure 3.8 (frequency), separately.

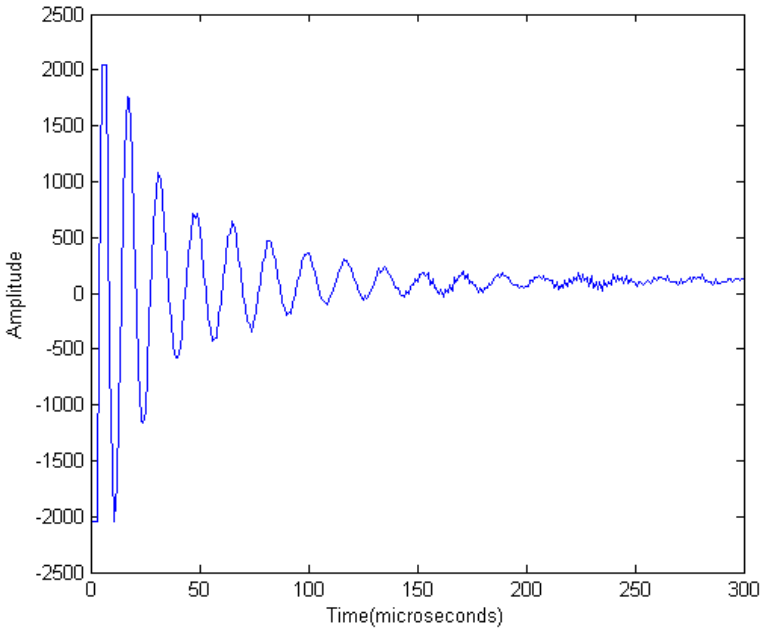

Figure 3.7 Ring effect in one pulse

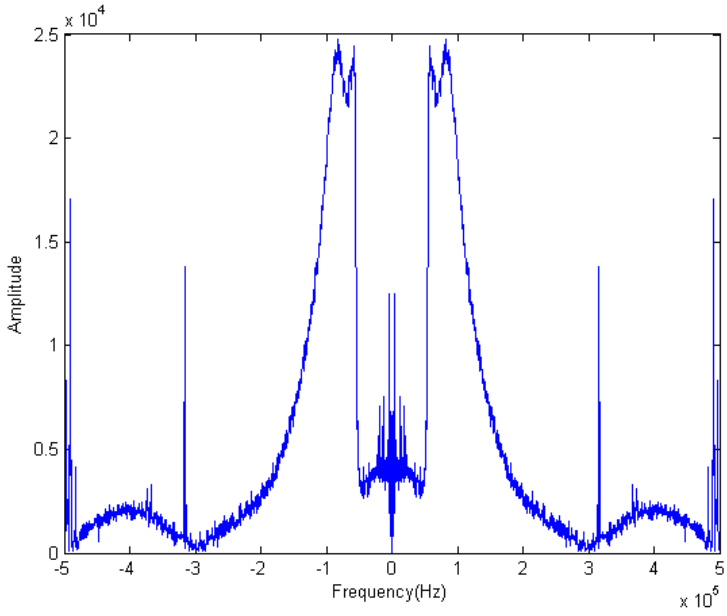

Figure 3.8 Spectrum of the ring signal

As can be seen from Figure 3.7, the ring effect lasts approximately 0.2 ms and then vanishes. The magnitude of the ring signal is large and exceeds the reference voltage at the beginning of the pulse. Therefore, the ring signal will totally submerge the wanted returned signal. Figure 3.8 is the FFT result of Figure 3.7, and zero frequency has been properly shifted to the middle of the figure. As can be seen, the ring is a wideband signal from about 0.05 MHz to 0.2 MHz. Therefore, the measurement of the distance which corresponds to this frequency range (0.05 MHz to 0.2 MHz) will be seriousely corrupted.

One method to eliminate the ring effect is to use the TM signal, in which frequency is continuous even between the successive pulses. However, the PRF will be havled compared to the SM case.

Another method is to discard the data sections corrupted by the ring effect in post signal processing. However, this has the negetive impact of decreasing the signal resolution. Either way has its advantages and disadvantages, and therefore a tradeoff must

be made according to the actual demands. If high resolution is more important than high PRF, then TM-LMF signal can be used. Othterwise, SM-LFM signal should be used and the data corrupted by the ring effect should be discarded .

In the customized FMCW SAR system in this research, the TM signal is used because the PRF is still high enough (maximum 1000 Hz) for normal SAR configuration in field test.

3.4.3.2 Power supply

The power unit of the radar supports 12 V–36 V DC input voltage and 6 A maximum current. Several power modules are used to generate six different voltages: 15 V, 5 V, 3 V, 1.8 V, 1.3 V, and -5 V.

3.5 Results

This section first shows the photo of the radar system in Figure 3.9. Then test results for different units are presented separately. The SAR ground tests and results are shown at the end of this section.

3.5.1 Radar System

The radar is composed of three customized micro-strip circuit boards and some off-the-shelf microwave components. The final system is powered by a 5-cell 5000 mAh 18 V battery. The working current of the system is about 1.5 A. Therefore, the radar can work up to 3 hours when the power supply battery is fully charged. The photo of the radar system is shown in Figure 3.9.

Figure 3.9 The customized FMCW SAR radar system

The metal box on the left side of Figure 3.9 is the experimental radar system. The battery next to the metal box is the power supply for the system. The long box on the right side of the figure is the antenna system which contains two antennas, one for transmitting and one for receiving. The antenna is 2x8 patch array which is shown in front of the long box and was originally used in the BYU μSAR system [9]. The centre of the picture is a laptop used for image generation and parameter settings. The SAR system can work standalone to collect raw data without connecting to a computer.

3.5.2 RF Generator

The LFM signal generated by the DDS is shown in Figure 3.10.

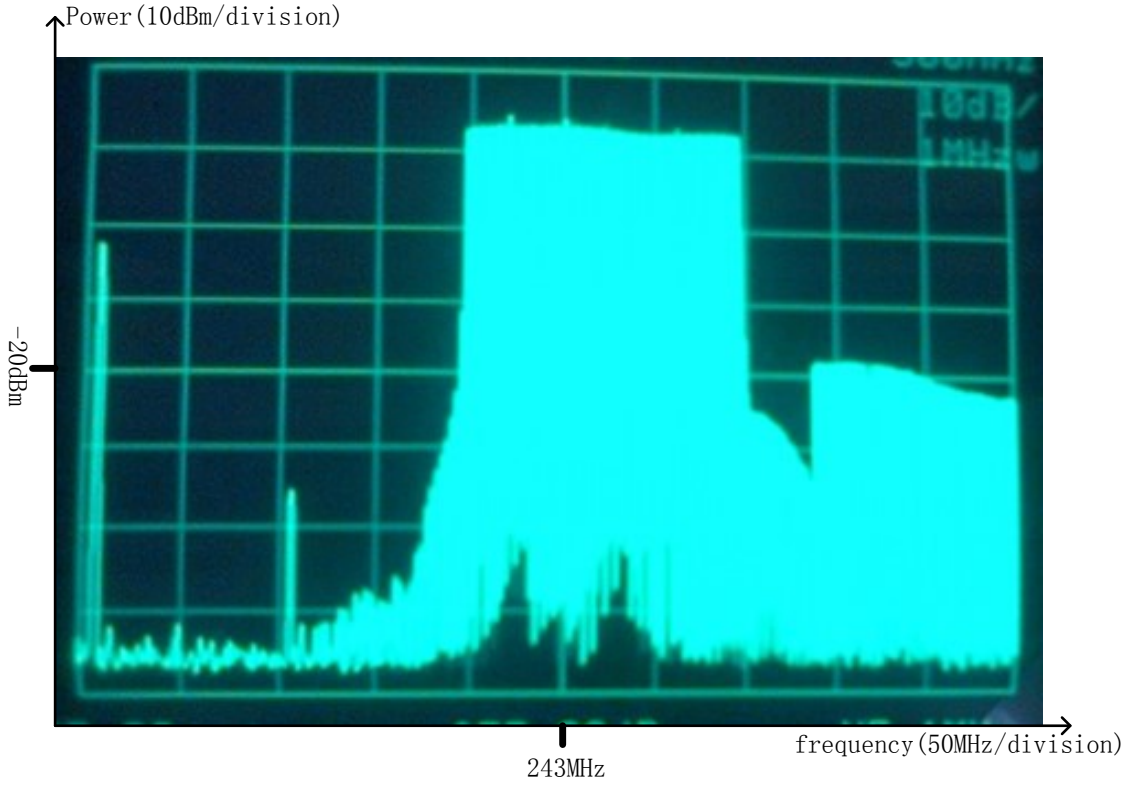

Figure 3.10 Spectrum of the LFM signal

Figure 3.10 shows the 150 MHz bandwidth LFM signal monitored on a spectrum analyzer. The horizontal direction is the frequency axis, and each division represents 50 MHz. Therefore, the mainlobe of the LFM signal occupies 3 grids. The vertical direction is the power of the spectrum with 10dBm per division. The average power of the mainlobe is about 12 dBm. Higher sidelobes are observed on the right side of the mainlobe, which is about 30 dB below the mainlobe. The two single peaks on the left side of the LFM signal are artificials of the analyzer.

3.5.3 Impulse Response

The impulse response of the radar (not including the antennas) can be obtained by a closed loop test. A coaxial cable connected the transmitter to the receiver, with no antennas connected. The transmitted signal will be directly received by the receiver likes the signal is reflected by an ideal point target. Therefore, the impulse response of the radar system can be measured. Attenuators were used at the output of the transmitter to decrease the transmitted power. The parameters used in the test are given by Table 3.3.

Table 3.3 Impulse response test parameters

Parameters	Value	Unit
Bandwidth	150	MHz
PRF	1000	Hz
Cable length	5.5	m
ADC rate	2	Msamples/second

The results are shown by Figure 3.11 and Figure 3.12. The impulse response of three pulses is shown in Figure 3.11. The horizontal direction is time axis and the vertical direction is amplitude axis. Each division represents 250 microseconds along time axis and 100 mV along vertical axis. The horizontal line in the middle represents 0 V. We can see that the IF signal of the middle pulse occupies 4 divisions of time axis ($250\ \mu s \times 4\ divisions = 1000\ \mu s$), which corresponds to 1000 Hz PRF. The responses of different pulses are the same.

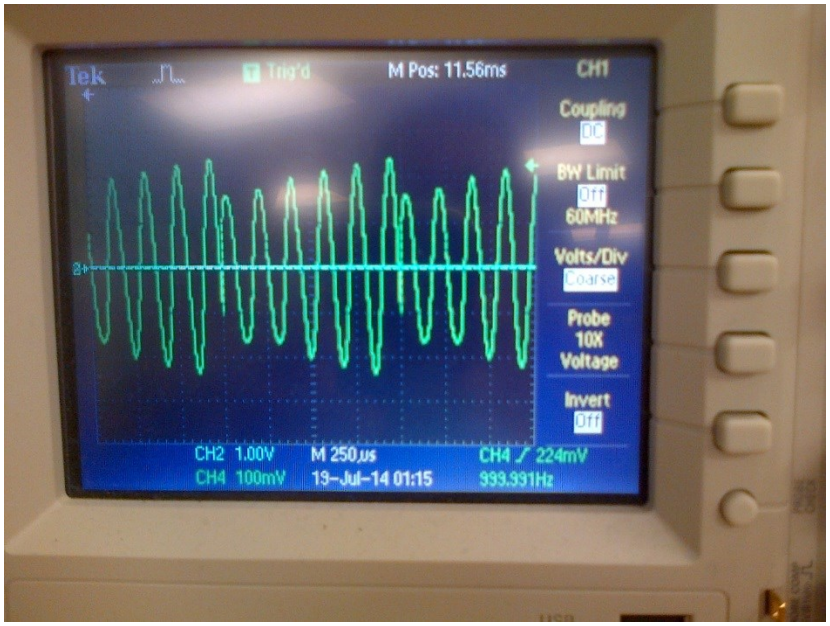

Figure 3.11 Overview of the impulse response

The impulse response in one pulse is shown by Figure 3.12. The horizontal direction is time axis and the vertical direction is amplitude axis. Each division represents 100 microseconds along time axis and 100 mV along vertical axis. The middle horizontal line is 0 V. The total time represented by the time axis is thus $100\ \mu s \times 10\ divisions = 1000\ \mu s$, and there are 5.5 periods of sinusoidal functions in this time interval. Therefore, the frequency of the signal is 5.5 kHz. For a target at 1 m from the radar, the frequency of the IF signal can be calculated as

$$f_{R=1} = \frac{Bw}{T} \cdot \frac{2 \cdot 1}{c} \tag{3.4}$$

where Bw is the signal bandwidth and T is the PRT. Substituting the value of the parameters shown in Table 3.3 to (3.4), we obtain that $f_{R=1} = 1000$ Hz. Therefore, 5.5 kHz IF signal corresponds to 5.5 m distance, which equals the length of the cable used in the experiment.

The amplitude of the IF should theoretical be constant. The unstable amplitude fluctuations shown in Figure 3.11 and Figure 3.12 may be caused by imperfections in the radar hardware.

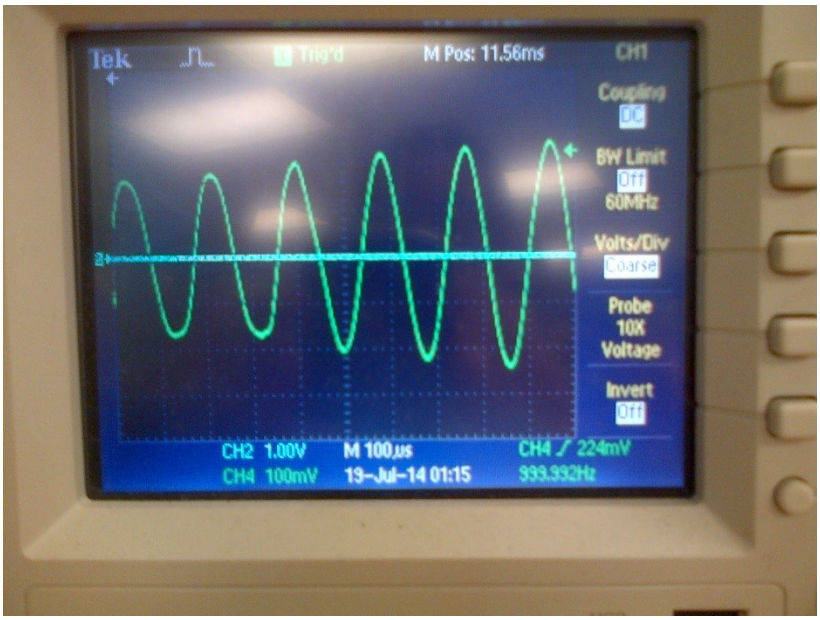

Figure 3.12 Impulse response in one pulse

3.5.4 System Coherency and Data Recording

In a coherent radar system, the continuous movement of antennas will cause continuous phase variations between the successive pulses in the recorded data. The coherence of the radar can be tested in the laboratory before field experiments by rotating the antenna and observing the recorded data. The data recorded by SD card during the rotating test is shown in Figure 3.13.

In this test, the antennas were manually held and rotated by an angle of approximately 150 degree. Attenuators were used to decrease the transmitted power. The radar parameters used in this experiment is shown by Table 3.3. In Figure 3.13, horizontal axis is

azimuth time and vertical is range time. There are 3444 pulses in azimuth direction, which corresponds to 3.444 s.

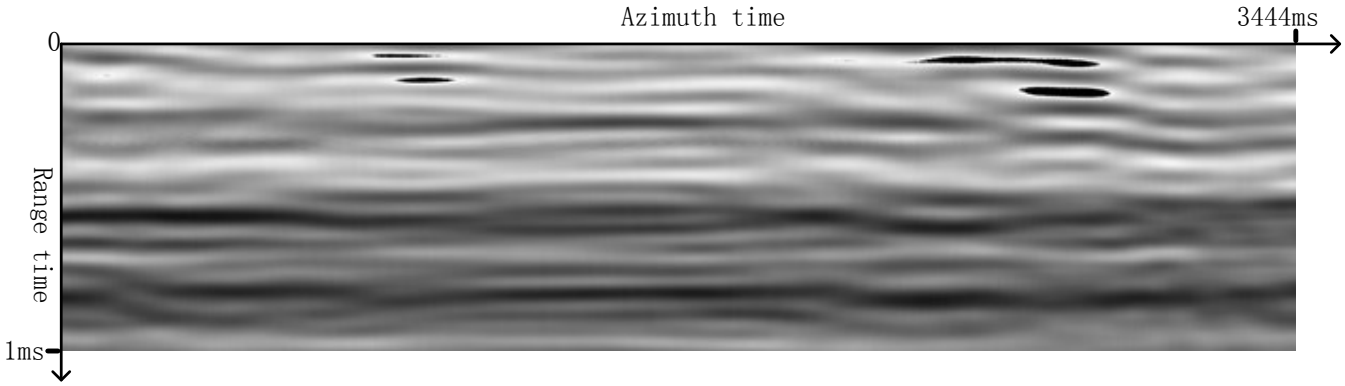

Figure 3.13 Recorded data when rotating antennas

It can be observed that the phase changes continuously along azimuth because of the continuous rotation of the antennas. The black spots on top of the figure are caused by ADC saturation because of the strong signal reflected from close strong targets. This test demonstrates that the data recording section works well.

3.5.5 Range Test

In the range test, the antennas were pointed outside through a window. The configuration is shown in Figure 3.14 (an image cut from google map). In this test, the antennas are mounted inside the houses shown at the left bottom corner of Figure 3.14 and pointed to the direction marked by the straight line in the figure. The length of the straight line shows the distance from the antennas to the observing area. The window in Figure 3.14 shows that the ground length of the line is 123.76m.

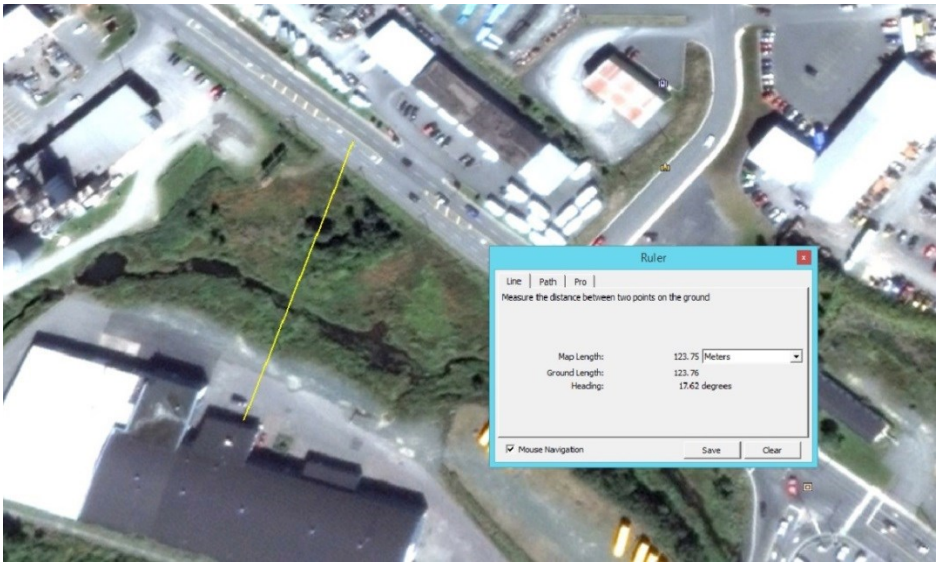

Figure 3.14 Range test configuration

The time domain IF data in one pulse and its FFT result are shown in Figure 3.15 and Figure 3.16, separately. The transmitted signal bandwidth is 150 MHz, PRF is 1000 Hz and ADC rate is 1 Msamples/second. For the convenience of the range distance calculation, the spectrum in Figure 3.16 is not shifted after FFT. Zero frequency point is the origin of the figure. From the origin to the middle of the frequency axis, the frequency increases. As can be observed from Figure 3.16, the main energy locates around 120 samples. From (3.4), it is known that 1 m distance corresponds to an IF signal of 1000 Hz when using the parameters of 150 MHz bandwidth and 1000 Hz PRF. Since each sample in frequency domain represents 1000 Hz (see (2.10)) when $PRT = 1/PRF = 1\,\text{ms}$, the 120^{th} sample represents an IF signal of 120 kHz, which corresponds to 120 m distance from the radar. This result is consistent with the distance of the observing area shown in Figure 3.14.

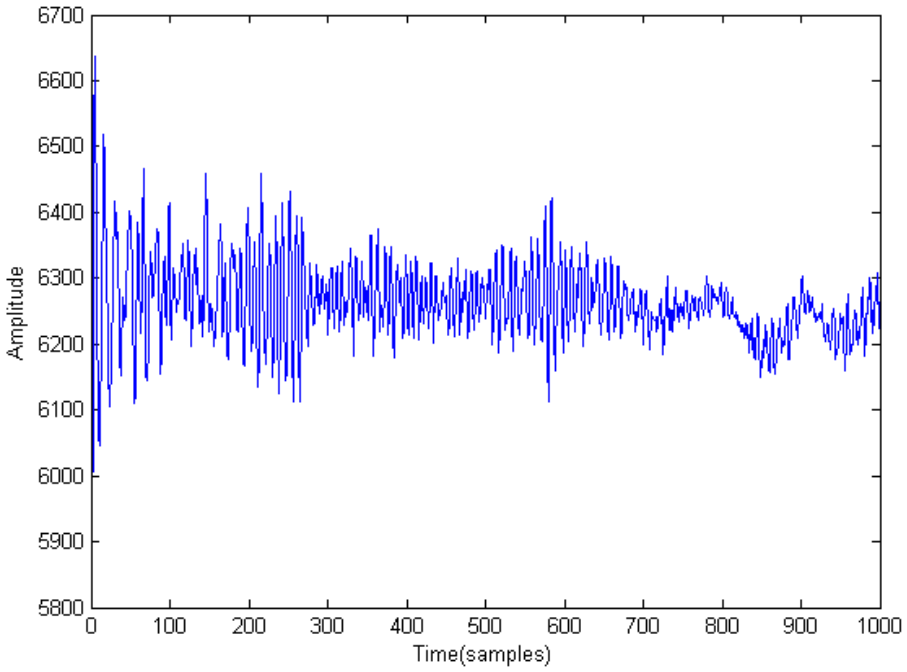

Figure 3.15 Time domain plot of the IF signal

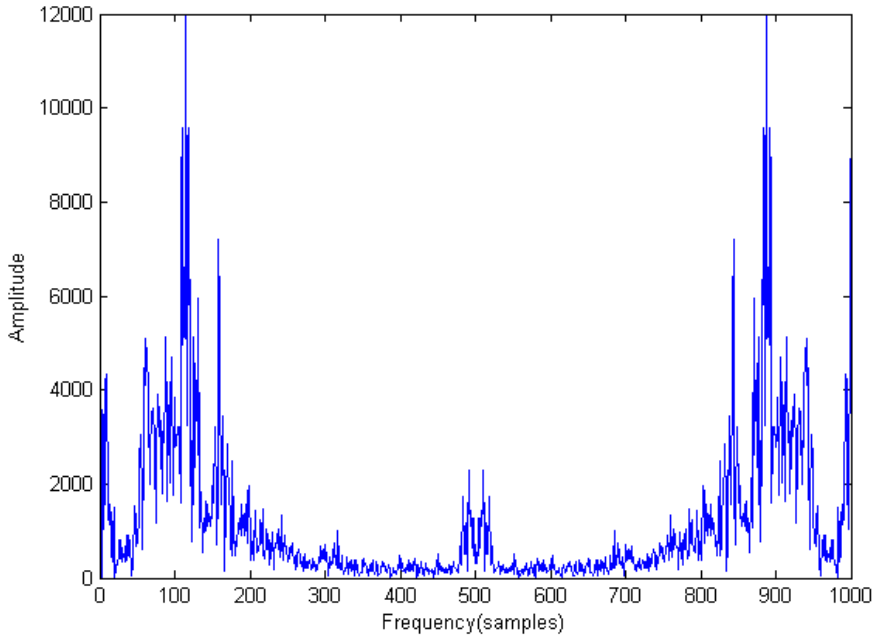

Figure 3.16 Frequency domain plot of the IF signal

3.5.6 SAR Imaging

A moving platform is required to obtain SAR images. A van was used in the test to be the carrier platform of the SAR. The parameters of the test are shown in Table 3.4.

Table 3.4 SAR test parameters

Parameters	Value	Unit
Bandwidth	150	MHz
PRF	250	Hz
Velocity	60	km/h
Waveform	Triangularly modulated	

The antennas were mounted on top of the van using a wood frame; the radar was put inside the van and connected to the antennas via coaxial cables. The configuration for this ground car experiment is shown in Figure 3.17.

The route of the van in the ground test is The Boulevard Road in St. John's, NL in Figure 3.18 which is cut from google map. The antennas were pointed to the other side of Quidi Vidi Lake. The imaging distance is about 400 m–600 m.

Figure 3.17 Antennas in ground car experiment

Figure 3.18 Route of the van in the ground test

The SAR image generated during the ground experiment is shown in Figure 3.19.

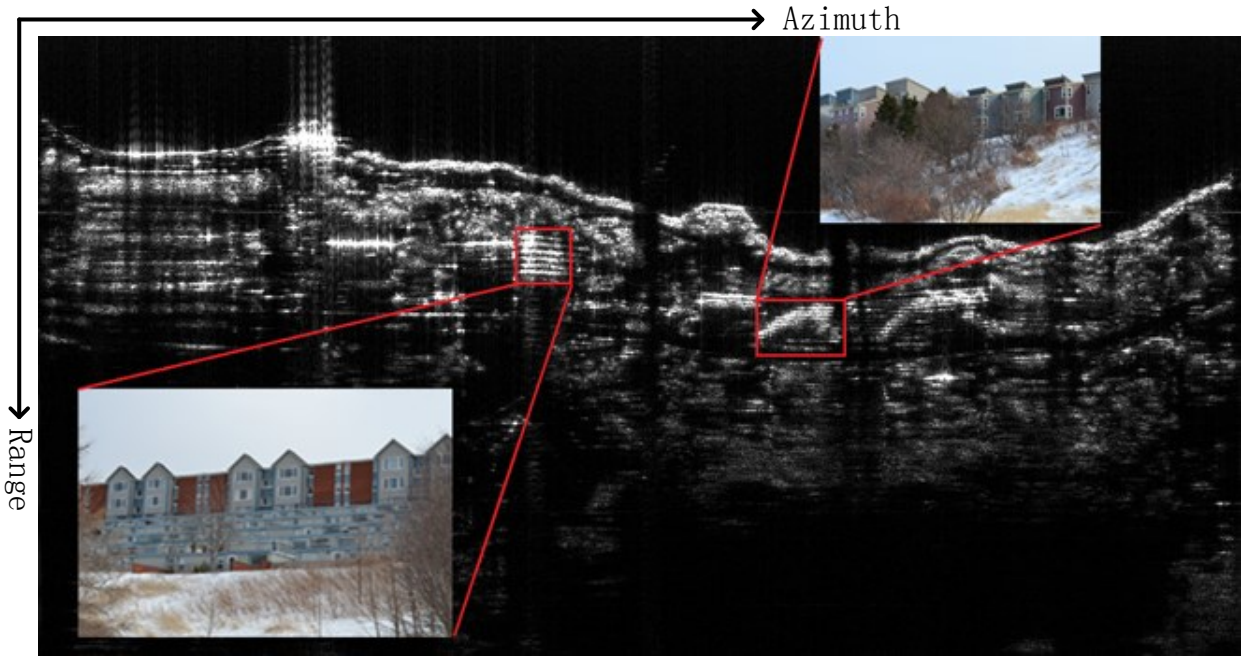

Figure 3.19 SAR image of Quidi Vidi Lake area (998 m x 1268 m)

The optical photos of the corresponding buildings in the SAR image are also included in Figure 3.19. The ladder-shape building shown by the picture on the left bottom is represented in the SAR image by several horizontal lines because the radar only observed

its side. Several vertical black strips are presented in the image because the radar beam was blocked by close-by buildings. The building shown by the top optical picture appears twice in the SAR image because the road has a small curve when observing this building, which made the radar illuminate it twice. The SAR image of the same area obtained by the early prototype of the BYU μSAR can be found in [43], which is shown in Figure 3.20. A better image quality (lower noise level, higher resolution) in Figure 3.19 than that of Figure 3.20 can be observed. Better images could be obtained by flying the SAR because more viewing angles of the ground objects can be obtained in airborne cases. For example, the ladder-shape building in Figure 3.19 will not be represented by six white horizontal lines in an airborne image. The building will look more similar to its optical image.

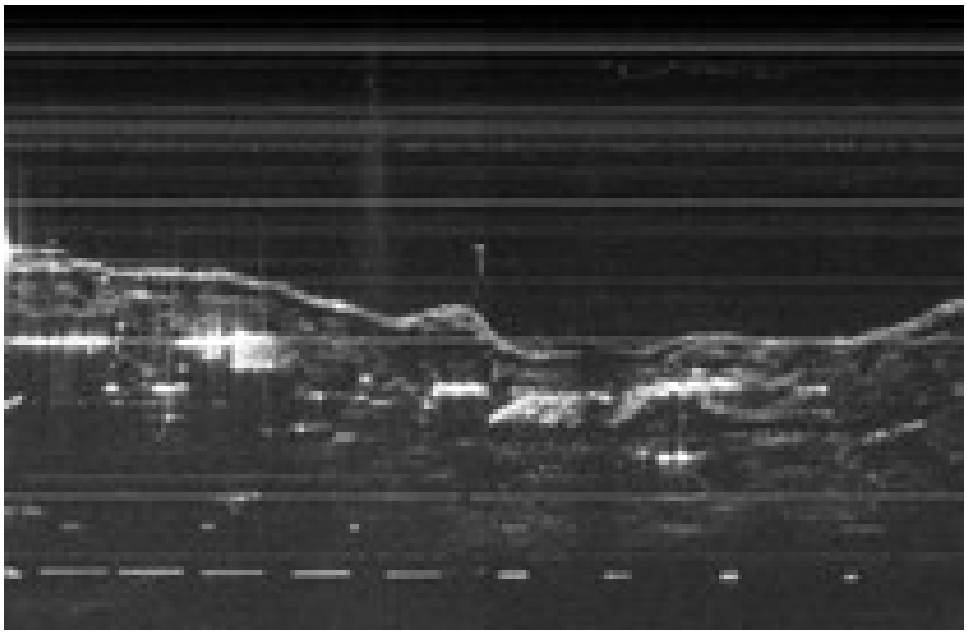

Figure 3.20 SAR image of the Quidi Vidi Lake area from [43]

Figure 3.19 is generated by the RDA introduced in Section 2.2.3.1 using computer. The SAR signal processing program is written by the author using Matlab. No motion

compensation [50] is used. The vertical is the range direction and the horizontal is the azimuth direction. The background noise is low as can be observed in the dark area on top of Figure 3.19. Speckle noise will be presented in the cases of higher noise floor and the dark area will not be as pure as shown in Figure 3.19.

The optical image of the same area cut from Google map is shown by Figure 3.21 for a comparison with the SAR image. As can be observed, the SAR image in Figure 3.19 shows the same ground features (such as the shape of the lake shore and the position of the buildings) as the optical image in Figure 3.21.

Figure 3.21 Optical image cut from Google map

3.6 Summary

This chapter corresponds to Contribution 1 in Section 1.3: This chapter introduces the two different radar systems built by the author. The first one is a SF radar altimeter, which is also the beginning of the research. The customized FMCW SAR system is designed and built on the experience obtained during the building of the SF radar. The FMCW SAR has been tested and validated to be able to generate high quality images of the observed area.

CHAPTER 4. DETECTING MOVING TARGETS BY TRIANGULARLY MODULATED SIGNALS

4.1 Background and Literature Review

Sawtooth modulated (SM) LFM signal and triangularly modulated (TM) LFM signal are the most widely used LFM waveforms in the modern pulse compression radar systems.

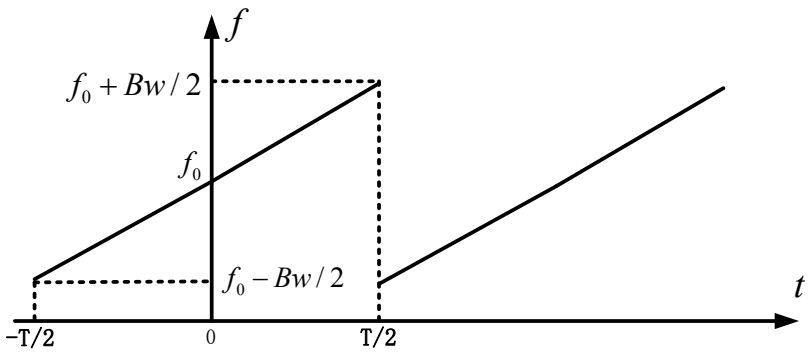

Figure 4.1 Sawtooth modulated LFM signal

The time frequency plot of a SM signal is shown in Figure 4.1. The frequency increases linearly from a starting value up to the end value, and then jumps back to the starting frequency immediately. Most FMCW SAR systems use this modulation method because it is the simplest LFM waveform. It can also achieve a higher PRF [13], [22].

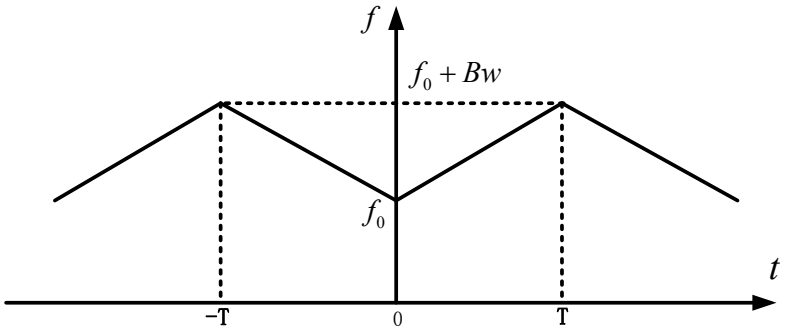

Figure 4.2 Triangular modulated LFM signal

A typical TM signal is shown in Figure 4.2. The frequency increases linearly from a starting value up to an end value and then ramps down to the starting frequency with the same (or different) FM rate. The up and down sweep can be symmetric or asymmetric. The TM-LFM signal presented in this chapter is a symmetric one. One period of the TM signal is traditionally viewed as a combination of two different SM signals with opposite FM rates. TM signal is commonly used because of the ease of hardware implementation (see Section 3.4.3.1) but not a signal processing requirement. In fact, usually only one half of the TM signal is used for data extraction.

In SAR image formation, the TM signal is treated as two SM signals and only one of the SM signals (up or down slope) is used to process the images [22], [34]-[36]. The employment of both SM sides are found in moving targets indication [17]-[19], [35], in which both SM signals are analyzed separately and the results are compared to detect the moving target.

Instead of treating the TM signal as two separated SM signals in the traditional way, this chapter establishes a mathematical model for analyzing the TM signal as one integral signal. Then a moving target indication (MTI) method is proposed based on the new model.

The traditional way of indicating moving targets is by detecting the Doppler frequency shift caused by their movement. However, Doppler-effect-based methods fail when the targets move slowly and do not introduce a detectable Doppler frequency shift (see Section 4.4.2). The proposed MTI method does not depend on Doppler effect detection and indicates moving targets by their wavelength-order movement inside a short time period. Therefore, very slow targets can be detected as long as their relative distance to

the radar keeps changing. Dechirp-on-receive is also needed when using the proposed MTI method.

This chapter is organized as follows. In the second section, the velocity ambiguity problem in MTI when using the LFM signal is introduced. In the third section, the analytical model used to analyze the TM signal is established. The fourth section is dedicated to the development of the MTI method. The MTI method is verified in Section 5 by simulation and real data, and the summary is given in Section 6.

4.2 Velocity Ambiguity of the LFM Signal

Exponential expressions are used in this section to explain the ambiguity problem in MTI when using LFM signal. Assuming the SM transmitted signal is

$$s_T(t) = e^{j\pi kt^2} e^{j2\pi f_0 t} \tag{4.1}$$

where k is the FM rate and f_0 is the centre frequency. Signal amplitude is assumed to be one for simplicity.

The returned signal is

$$s_R(t) = e^{j\pi k(t-\tau)^2} e^{j2\pi f_0(t-\tau)} \tag{4.2}$$

where $\tau = 2R/c$ is the distance between the radar and the target. The amplitude of the reflected signal is assumed to be one.

The IF signal is then

$$s_{IF}(t) = e^{j2\pi f_0 \tau} e^{j2\pi kt\tau} e^{-j\pi k\tau^2} . \tag{4.3}$$

The last term is normally neglected because its effect is small if the observing scenes are small [33] (Page 144), which is almost the case considering the short operation range of FMCW radar.

If the target is moving with a constant radial speed, we have

$$\tau = \frac{2R_0}{c} + \frac{2v_r t}{c} \tag{4.4}$$

where v_r is the radial speed of the target, and R_0 is the target's initial range from the radar when the radio wave is transmitted. Substituting (4.4) into (4.3), we have

$$s_{IF}(t) = e^{j\frac{4\pi R_0}{\lambda}} e^{j4\pi\left(\frac{kR_0}{c}+\frac{v_r}{\lambda}\right)t} e^{j2\pi k\frac{2v_r}{c}t^2}. \tag{4.5}$$

The first exponential term is a constant. The last exponential term is very small because it is the t^2 term (the length of t is normally several milliseconds). Therefore, the FFT of (4.5) will be a sinc function whose peak centre is at

$$f = 2\left(\frac{kR_0}{c} + \frac{v_r}{\lambda}\right). \tag{4.6}$$

Eq. (4.6) shows that the peak position in the frequency domain is determined both by the target's initial range and the target's radial velocity. Therefore, either range or velocity cannot be measured unambiguously by SM signal.

One way of removing the ambiguity is to use the TM signal, which can be seen as two separated SM signals with opposite FM rate. Because the radial velocity of the target will cause opposite frequency shifts in the two SM signals and the distance will cause the same frequency shifts, the velocity and the distance of the target can be measured unambiguous by comparing the FT results of the two SM signals [17]-[19].

4.3 A New Model of the Triangularly Modulated Signal

A triangularly modulated signal is shown in Figure 4.3, where f_0 is the carrier frequency, and Bw is the bandwidth. The duration of the TM signal is $PRT = 2T$. The TM signal can be expressed as

$$s_T(t) = rect\left(\frac{t+T/2}{T}\right)\cos\left(-\pi kt^2 + 2\pi f_0 t\right) + rect\left(\frac{t-T/2}{T}\right)\cos\left(\pi kt^2 + 2\pi f_0 t\right) \quad (4.7)$$

where $k = Bw/T$ is the FM rate. The amplitude of the transmitted signal is assumed to be one without loss of generality.

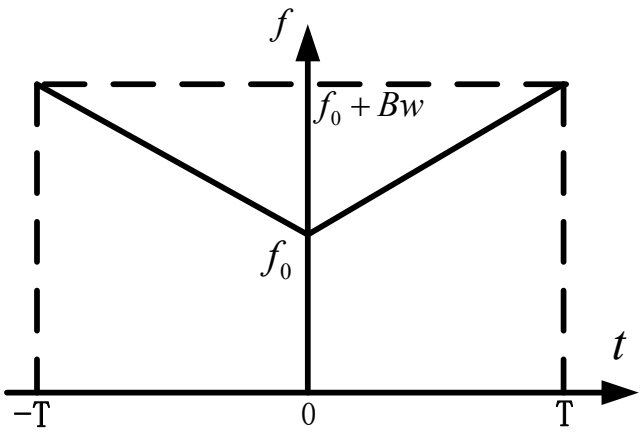

Figure 4.3 Time-frequency plot of a triangular LFM signal

The received signal is a time delayed version of (4.7), which is

$$\begin{aligned} s_R(t) = {} & \sigma \cdot rect\left(\frac{t+T/2}{T}\right)\cos\left[-\pi k(t-\tau)^2 + 2\pi f_0(t-\tau)\right] \\ & + \sigma \cdot rect\left(\frac{t-T/2}{T}\right)\cos\left[\pi k(t-\tau)^2 + 2\pi f_0(t-\tau)\right] \end{aligned} \quad (4.8)$$

where σ is the amplitude of the received signal, $\tau = 2R/c$ is the two way time delay. The IF signal is generated by mixing (4.8) with (4.7) and removing the sum frequency by filtering, which is

$$\begin{aligned} s_{IF}(t) &= \sigma \cdot rect\left(\frac{t+T/2}{T}\right)\cos\left(2\pi k\tau t - \pi k\tau^2 - 2\pi f_0\tau\right) \\ &+ \sigma \cdot rect\left(\frac{t-T/2}{T}\right)\cos\left(-2\pi k\tau t + \pi k\tau^2 - 2\pi f_0\tau\right) \end{aligned} \tag{4.9}$$

By using Euler's identity, (4.9) can be rewritten as

$$\begin{aligned} s_{IF}(t) &= \frac{\sigma}{2} rect\left(\frac{t+T/2}{T}\right)e^{j2\pi k\tau t}e^{-j2\pi f_0\tau}e^{-j\pi k\tau^2} + \frac{\sigma}{2} rect\left(\frac{t-T/2}{T}\right)e^{j2\pi k\tau t}e^{j2\pi f_0\tau}e^{-j\pi k\tau^2} \\ &+ \frac{\sigma}{2} rect\left(\frac{t+T/2}{T}\right)e^{-j2\pi k\tau t}e^{j2\pi f_0\tau}e^{j\pi k\tau^2} + \frac{\sigma}{2} rect\left(\frac{t-T/2}{T}\right)e^{-j2\pi k\tau t}e^{-j2\pi f_0\tau}e^{j\pi k\tau^2} \end{aligned} \tag{4.10}$$

After the CTFT of (4.10), the first two terms will appear at the positive frequency side of the two-sided Fourier spectrum, while the other two terms will appear as the image at the negative frequency which could be neglected because no new information is included. Therefore, the last two terms of (4.10) will be omitted in the subsequent equations. Rearranging the first two terms of (4.10), we have

$$\begin{aligned} s_{IF1}(t) &= \frac{\sigma}{2} rect\left(\frac{t+T/2}{T}\right)e^{j2\pi k\tau\left(t+\frac{T}{2}\right)}e^{-j2\pi k\tau\frac{T}{2}}e^{-j2\pi f_0\tau}e^{-j\pi k\tau^2} \\ &+ \frac{\sigma}{2} rect\left(\frac{t-T/2}{T}\right)e^{j2\pi k\tau\left(t-\frac{T}{2}\right)}e^{j2\pi k\tau\frac{T}{2}}e^{j2\pi f_0\tau}e^{-j\pi k\tau^2} \end{aligned} \tag{4.11}$$

If a target moves with a radial speed of v_r and the radar is stationary, then the time delay τ could be expressed as

$$\tau = \tau_n + \tau_r = \frac{2R_n}{c} + \frac{2v_r t}{c} \quad n = 0,1,2\cdots \tag{4.12}$$

where R_n is the instantaneous distance from the target to radar when the middle of the n[th] triangular sweep is transmitted. Substituting (4.12) into (4.11), we have

$$\begin{aligned} s_{IF1}(t) = {} & \frac{\sigma}{2} rect\left(\frac{t+T/2}{T}\right) e^{j2\pi k\left(t+\frac{T}{2}\right)\tau_n} e^{-j2\pi k\frac{T}{2}\tau_n} e^{-j2\pi f_0\tau_n} e^{-j2\pi f_0\frac{2v_r}{c}\left(t+\frac{T}{2}\right)} e^{j2\pi f_0\frac{2v_r}{c}\frac{T}{2}} e^{-j\pi k\tau_n^2} \\ & \cdot e^{-j2\pi k\tau_n\frac{2v_r}{c}t} e^{j2\pi k\frac{2v_r}{c}t^2} e^{-j\pi k\frac{4v_r^2}{c^2}t^2} \\ & + \frac{\sigma}{2} rect\left(\frac{t-T/2}{T}\right) e^{j2\pi k\left(t-\frac{T}{2}\right)\tau_n} e^{j2\pi k\frac{T}{2}\tau_n} e^{j2\pi f_0\tau_n} e^{j2\pi f_0\frac{2v_r}{c}\left(t-\frac{T}{2}\right)} e^{j2\pi f_0\frac{2v_r}{c}\frac{T}{2}} e^{-j\pi k\tau_n^2} \\ & \cdot e^{-j2\pi k\tau_n\frac{2v_r}{c}t} e^{j2\pi k\frac{2v_r}{c}t^2} e^{-j\pi k\frac{4v_r^2}{c^2}t^2} \end{aligned} \quad . \tag{4.13}$$

Before performing CTFT to (4.13), some small terms can be neglected. The exponentials $\exp\left(-j2\pi k\tau_n 2v_r t/c\right)$ of the first and second terms of (4.13) correspond to a small Doppler effect, but much smaller than the exponential term $\exp\left(-j2\pi f_0 2v_r\left(t+T/2\right)/c\right)$ and $\exp\left(-j2\pi f_0 2v_r\left(t-T/2\right)/c\right)$ because $f_0 \gg k\tau_n$ in common FMCW SAR (short radar range). The last two exponentials $\exp\left(j2\pi k2v_r t^2/c\right)\exp\left(-j\pi k4v_r^2 t^2/c^2\right)$ of the first and second terms are t^2 terms, which will cause the broadening of the peak in frequency domain. However, this broadening effect can be neglected under high PRF assumption. Therefore, the last three exponentials of the first and the second terms (the second and forth rows) of (4.13) can be discarded since they are very small under normal radar parameters (Table 3.1 shows parameters of a typical C-band radar). Then, the CTFT of (4.13) is

$$\begin{aligned} S_{IF1}(f) = {} & \frac{\sigma T}{2}\mathrm{sinc}\left[T\left(f-k\tau_n+\frac{2v_r}{\lambda}\right)\right] e^{-j2\pi k\frac{T}{2}\tau_n} e^{-j2\pi f_0\tau_n} e^{j2\pi\frac{T}{2}f} e^{j2\pi\frac{v_r}{\lambda}T} e^{-j\pi k\tau_n^2} \\ & + \frac{\sigma T}{2}\mathrm{sinc}\left[T\left(f-k\tau_n-\frac{2v_r}{\lambda}\right)\right] e^{j2\pi k\frac{T}{2}\tau_n} e^{j2\pi f_0\tau_n} e^{-j2\pi\frac{T}{2}f} e^{j2\pi\frac{v_r}{\lambda}T} e^{-j\pi k\tau_n^2} \end{aligned} \tag{4.14}$$

where $\lambda = c / f_0$ is the wavelength. The two sinc terms in (4.14) represent two peaks in frequency domain. The positions of the peaks are determined by two factors: initial target distant R_n (at the middle of the nth pulse) and the radial velocity v_r of the target. The initial distance causes the two sinc peaks to move in the same directions along the frequency axis while the radial velocity makes them move in the opposite directions.

4.4 Moving Target Indication

4.4.1 Fast Moving Target

When the target radial velocity v_r is high, the two sinc terms in (4.14) will move more than one resolution unit (3 dB mainlobe width of the sinc function) in the frequency domain in the opposite directions to one another. This will cause the two sinc functions to be separated and easily distinguished in the frequency domain, which is the basic idea of the MTI methods in [17]-[19], [35]. To resolve the two sinc functions, the Doppler effect needs to shift each sinc function by half of its null-to-null mainlobe width (the width between the two closest zero points away from peak, which is 2/T). Therefore, the radial velocity needed for detecting the moving targets by the Doppler effect is

$$\frac{2v_r}{\lambda} \geq \frac{1}{T} \Rightarrow v_r \geq \frac{\lambda}{2T} = \frac{\lambda}{PRT}. \tag{4.15}$$

For a 5.4 GHz C-band radar with 250 Hz PRF, v_r needs to be at least 13.8 m/s to make the two sinc functions easily distinguished. In many applications, such as monitoring icebergs, vessels or targets with low radial velocity, the radial speed will be much less than this threshold.

A choice for detecting a fast moving target is to use the 3 dB width of the sinc function, which is 1/T (half of the mainlobe width). This actually defines the minimum radial velocity that can be detected by the Doppler effect using a triangular sweep. For the example above, v_r needs to be at least 6.9 m/s to make the moving target detectable. A lower value of v_r will not allow the separation of the two sinc functions, and hence cannot be detected by the Doppler effect when using triangular LFM signal.

The threshold in (4.15) will be used to define fast moving targets in this chapter. For a target with radial velocity less than this threshold, part of the mainlobes of the two sinc functions shown in (4.14) will overlap, which can be used to indicate a slow moving target discussed below.

4.4.2 Slow Moving Target

When the target is slow or the PRF is high, the Doppler effect inside one pulse is normally neglected since it is very small. In this situation, the Doppler effect terms (v_r term) inside the sinc functions in (4.14) can be neglected. Then (4.14) can be simplified by using Euler's identity as

$$S_{IF1}(f) = \sigma \cdot T\text{sinc}\left[T(f - k\tau_n)\right]\cos\left[\pi T\left(f - k\tau_n - \frac{2f_0\tau_n}{T}\right)\right]e^{j2\pi\frac{v_r}{\lambda}T}e^{-j\pi k\tau_n^2} \quad (4.16)$$

with amplitude the product of a sinc function and a cosine function. The second term $k\tau_n$ inside the parenthesis of both sinc and cosine functions indicates that they will move in the same direction by the same amount determined by the instantaneous target distance. The third term inside the parenthesis of the cosine function implies that the cosine function will further move by $2f_0\tau_n / T$ relative to the sinc function. This will cause a misa-

lignment between the peaks of the sinc function and the cosine function. As a result, two peaks will appear in the product. The ratio between the movement caused by $2f_0\tau_n / T$ and the movement caused by $k\tau_n$ is

$$\frac{2f_0\tau_n / T}{k\tau_n} = \frac{2f_0}{kT} = \frac{2f_0}{Bw}, \tag{4.17}$$

where Bw is the bandwidth of the transmitted signal. The bandwidth of a radar system is normally several percent of the carrier frequency (value of (4.17) will be large), which means the cosine function will move much faster along frequency axis than the sinc function as the change of the initial range R_n at the middle of each pulse. Therefore, the shape of the magnitude of (4.16) will change continuously with the change of the position of the target.

The sinc function, cosine function and their products are shown in Figure 4.4. Figure 4.4(a) shows a typical plot of the product of the sinc function and the cosine function in (4.16). The dashed line is the cosine function in (4.16), the dotted line is the sinc function in (4.16) and the solid line is their product. Because of the existence of the term $2f_0\tau_n / T$ in the cosine function, the sinc function and cosine function are misaligned at most times (when the peak of the sinc function is not overlapped with one peak of the cosine function, they are misaligned). This will produce two peaks (not necessarily equal in amplitude) if the magnitude of Figure 4.4(a) is plot.

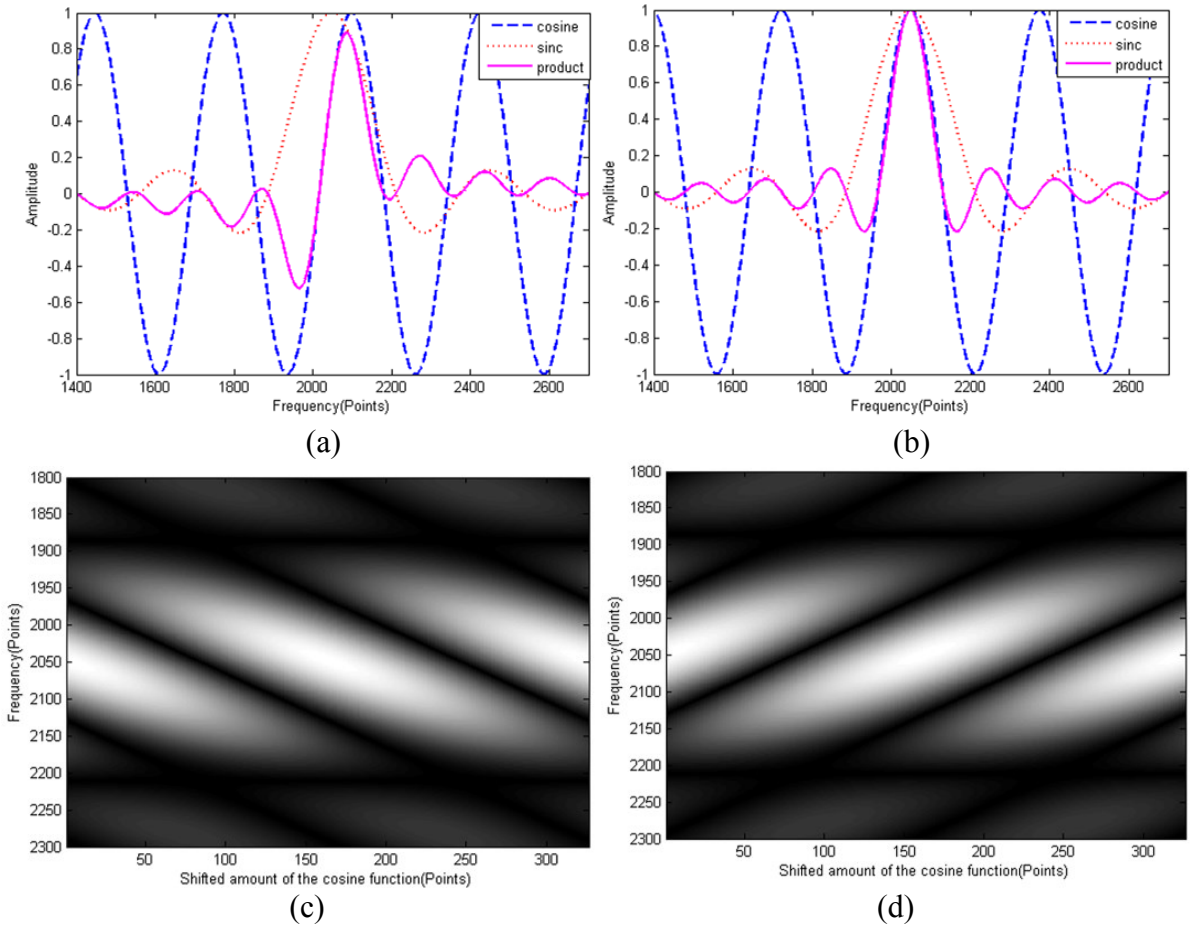

Figure 4.4 Product of the sinc function and the cosine function. (a) Amplitude: typical case. (b) Amplitude: special case ($2f_0\tau_n / T$ is an integer multiple of the period of the cosine function). (c) Magnitude: two periods of peak pattern (each slanted vertical is one period) formed by the continuous right shift of the cosine function. (d) Magnitude: two periods of peak pattern formed by the continuous left shift of the cosine function.

A special case occurs when the term $2f_0\tau_n / T$ is an integer multiple of the period of the cosine function. In this case, the product in (4.16) is a narrower sinc function due to the following identity

$$\begin{aligned} S_{IF1}(f) &= \sigma \cdot T\text{sinc}\left[T\left(f - k\tau_n\right)\right]\cos\left[\pi T\left(f - k\tau_n - \frac{2f_0\tau_n}{T}\right)\right]e^{j2\pi\frac{v_r}{\lambda}T}e^{-j\pi k\tau_n^2} \\ &= \sigma \cdot T\text{sinc}\left[T\left(f - k\tau_n\right)\right]\cos\left[\pi T\left(f - k\tau_n\right)\right]e^{j2\pi\frac{v_r}{\lambda}T}e^{-j\pi k\tau_n^2} \\ &= \sigma \cdot T\text{sinc}\left[2T\left(f - k\tau_n\right)\right]e^{j2\pi\frac{v_r}{\lambda}T}e^{-j\pi k\tau_n^2} \end{aligned} \quad . \quad (4.18)$$

Eq. (4.18) shows that when the term $2f_0\tau_n / T$ causes the cosine function to shift an integer multiple of its period (i.e. the sinc mainlobe peak is aligned with a peak of the cosine function), their product is a new sinc function with a mainlobe width half of that of the original sinc function. This can be observed in Figure 4.4(b), in which the product of the sinc and cosine function is a narrower sinc function. This provides a possibility to improve the range resolution without increasing the transmitted bandwidth due to the sampling nature of the radar system. If the radar can be designed in a way that the term $2f_0\tau_n / T$ can be removed from the cosine function every time when it takes a sample in azimuth, the improvement in range resolution can be achieved.

Empirical data collected for the MTI experimental have shown some apparent range improvement over singular points in range, but this could be an artifact of the hardware system used for the experiment. However, with improved hardware, it would give a better indication whether or not the observed phenomenon is worth further theoretical and experimental investigations.

The phenomenon shown in Figure 4.4(a) can be used in moving target detection. As shown by Figure 4.4(a) and (b), when the cosine function moves continuously with the change of the initial distance, the magnitude of the products in (4.16) from successive pulses will form a certain pattern which shows the target radial speed and the target moving direction. Figure 4.4(c) shows the pattern when the cosine function moves to the right of the frequency axis (corresponding to a target moving away from the radar) and Figure 4.4(d) shows the pattern when the target moves toward the radar.

In order to explain the formation of the peak pattern shown by Figure 4.4(c), we begin with examining the amplitude plot shown by Figure 4.4(a) and Figure 4.4(b).

Assume that the initial state is shown by Figure 4.4(b). If the target begins to move away from the radar, the cosine function (dashed line) shown by Figure 4.4(a) will begin to move toward higher frequency according to the term $2f_0\tau_n / T$ in (4.16). Since $2f_0\tau_n / T$ is the relative movement between the sinc function and the cosine function, we can imagine only the cosine function moves continuously according to $2f_0\tau_n / T$ while the sinc function stays stationary. With the movement of the cosine function, another peak will begin to appear at lower frequency as shown in Figure 4.4(a). The higher positive peak (around point 2070) in Figure 4.4(a) is the original peak (drawn by the solid line in Figure 4.4(b)) which moves from point 2048 to higher frequency; the lower negative peak (around point 1970) is the new peak that arises. With the continuous movement of the cosine function, both of the peaks will continuously move to higher frequency. Meanwhile, the negative peak will increase in magnitude and the positive peak will decrease in magnitude. The movement and decrease in the amplitude of the positive peak can be observed by comparing Figure 4.4(a) and Figure 4.4(b) (note that the peaks of the sinc function drawn by the dotted line in both figures are at 2048^{th} point). When the negative peak of the cosine function (around point 1930) shown by Figure 4.4(a) moves to point 2048 (align with the sinc function), the positive peak disappears and only the negative peak exists. This is the single peak case shown by Figure 4.4(b), with the only difference that the positive peak drawn by the solid line in Figure 4.4(b) becomes a negative peak this time (magnitude plot will be the same). If the cosine function continues to move, the above procedure will repeat and form the peak pattern shown in Figure 4.4(c). This peak pattern is composed of the slanted bright verticals that are parallel with each other and the period is the distance between two identical slanted verticals.

Similarly, the peak in Figure 4.4(d) first shifts to lower frequency due to the shorter distance caused by the approaching of the target.

The repetition period of the pattern is the same as the half period of the cosine function because after a half period, one peak (positive or negative) of the cosine function will align with the sinc function.

Since f_0 is normally large (several GHz), the term $2f_0\tau_n / T$ could be very sensitive to the change of the relative distance between the target and the radar. The relative distance change ΔR that makes the cosine function move for half of its period, i.e. the period of the pattern, can be calculated by

$$\frac{2f_0\Delta\tau}{T} = \frac{1}{T} \Rightarrow \Delta R = \frac{\lambda}{4} \quad (4.19)$$

For a 5.4 GHz radar system, this distance is only 0.014 m, meaning the period of the pattern corresponds to 1.4 cm relative distance change between the radar and the target.

4.4.3 Radial Velocity Measurement

The period of the peak pattern corresponds to the movement of $\lambda/4$ of the target. If the repetition period of the pattern measured by the data is $m \cdot \mathrm{PRT}$ seconds, then the radial velocity can be calculated as

$$v_r = \frac{\lambda}{4m\mathrm{PRT}} \quad m = 1, 2, 3\cdots \quad (4.20)$$

The maximum radial velocity that can be obtained by (4.20) is $\lambda/(4\cdot\mathrm{PRT})$ when $m=1$, which is still smaller than the fast moving target threshold λ/PRT defined by (4.15). Therefore, when the target radial velocity falls in the range

$$\frac{\lambda}{4\cdot \mathrm{PRT}} \le v_r \le \frac{\lambda}{\mathrm{PRT}}, \tag{4.21}$$

Eq. (4.20) cannot be used to calculate the velocity. We define the ambiguity index l

$$l = \left\lfloor v_r / \left(\lambda / \left(4 \cdot \mathrm{PRT} \right) \right) \right\rfloor \tag{4.22}$$

where $\lfloor x \rfloor$ means taking the largest integer not greater than x. When $1 \le l \le 3$, the radial velocity cannot be measured accurately by using the proposed method. The radial velocity threshold $\lambda / (4 \cdot \mathrm{PRT})$ corresponds to the speed at which the cosine function moves by half of its period in one PRT, and hence will not be observed in the peak pattern.

However, the peak pattern will still show a difference when $l \ge 1$ because the mainlobe of the sinc functions in (4.14) will begin to separate from each other with the increase of speed.

As shown by Figure 4.5, $k\tau_n$ is the frequency shift caused by the target distance, and the two sinc functions will move in opposite directions with increasing of radial speed. As a result, part of the mainlobes will still overlap and form the peak pattern discussed above, and the other part of the mainlobe will be gradually separated in the frequency domain. With a decrease of the overlapped part of the mainlobe, the pattern will become narrower in the range (frequency) direction, while the separated part will appear as solid lines on both sides of the peak pattern.

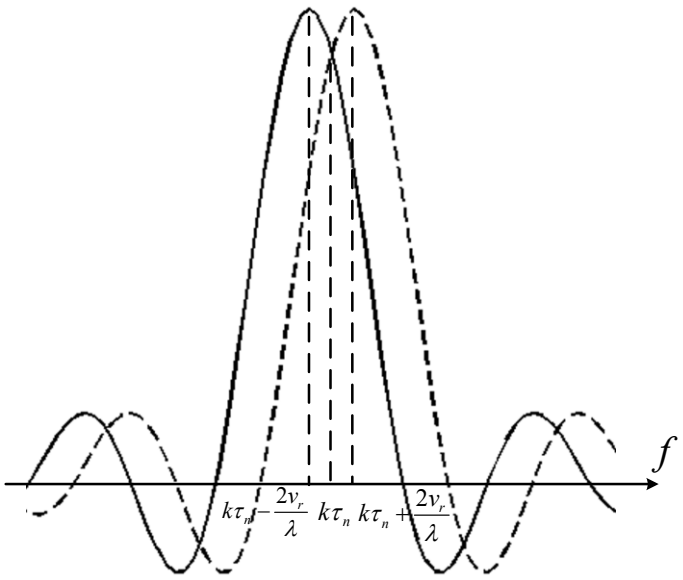

Figure 4.5 Separated sinc functions as radial velocity increases

4.5 Results

4.5.1 Simulation

The simulation parameters and signal processing parameters are shown in Table 4.1.

Table 4.1 Simulation parameters

Parameter	Value	Unit
Bandwidth	150	MHz
Carrier frequency	5590	MHz
PRF	250	Hz
Target radial velocity	0.3	m/s
Target initial distance	900	m
ADC rate	2	Msamples/second
FFT length	4096	Points
Frequency resolution	250	Hz
FFT weighting function	rectangular	

Figure 4.6 shows the peak pattern when the target leaves or approaches the radar with 0.3m/s radial speed. The horizontal axis represents the pulse number. The azimuth time can be calculated by multiplying the pulse number with PRT. No window is applied before the FFT. The ambiguity index is $l = 0$, so (4.20) can be used to calculate the target speed. Figure 4.6(a) is the FFT result of the TM signal (peak pattern of (4.16)) when the target is moving away from the radar and Figure 4.6(a) is the FFT result of the SM signal.

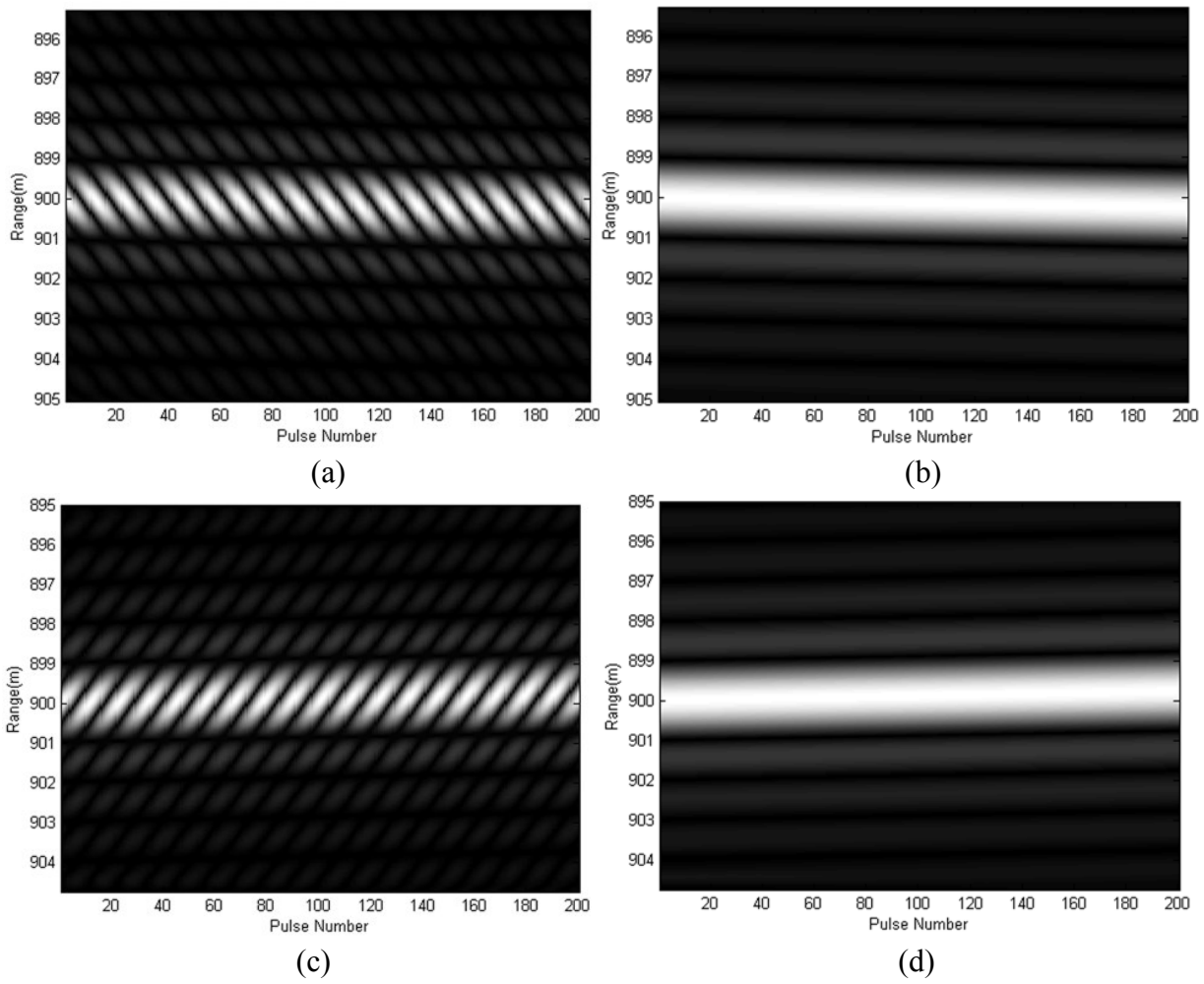

Figure 4.6 Peak patterns of the triangularly and sawtooth modulated signal when the target is moving with 0.3m/s radial speed. (a) Triangular peak pattern when target moves away. (b) Sawtooth peak pattern when target moves away. (c) Triangular peak pattern when target approaches. (d) Sawtooth peak pattern when target approaches.

Two hundred pulses are used to observe the target, during which the target moves 0.24m in line of sight direction.

No Doppler effect can be observed in Figure 4.6(a) or Figure 4.6(c) because the two sinc functions of (4.14) are completely overlapped, which makes Doppler-effect-based MTI methods [17]–[19], [35] fail to detect the moving target. Moreover, no target movement can be observed in Figure 4.6(b) or Figure 4.6(d) when using SM signal.

A clear pattern indicating the moving target is shown in Figure 4.6(a) using the proposed method in this chapter. The moving direction of the target can be immediately determined by observing the moving direction of the peak inside one pattern period. The period of the pattern is 11 pulses. By using (4.20), we can calculate that the target radial velocity is 0.3009 m/s, which is very close to the simulated value.

The pattern when the target is moving toward the radar is shown in Figure 4.6(c). Again, the moving target could be indicated by the TM signal and the direction can be determined. Figure 4.6(d) shows the FFT result of the SM signal, and no distance change between the radar and the target can be observed .

As can be seen in Figure 4.6 (a) and (c), we do not need the entire set of 200 pulses to indicate the moving of the target. 22 pulses (0.088s) which include two periods of the pattern are enough to indicate the moving target and calculate the moving parameters.

Other than the amplitude of the pattern, the azimuth phase of (4.16) could be used to calculate the period of the pattern in Figure 4.6(a) and (c). The first exponential term in (4.16) is a constant, and the second exponential term varies very slowly with the small change of τ_n. Therefore, the phase of (4.16) will be almost constant during a short observing period. The only fast varying term with the change of τ_n in (4.16) is the cosine

function, whose sign changes every half of its period. Therefore, the quadrant of the azimuth angle changes every period of the pattern. The azimuth angle will be a rectangular-like function whose half period equals to the period of the peak pattern.

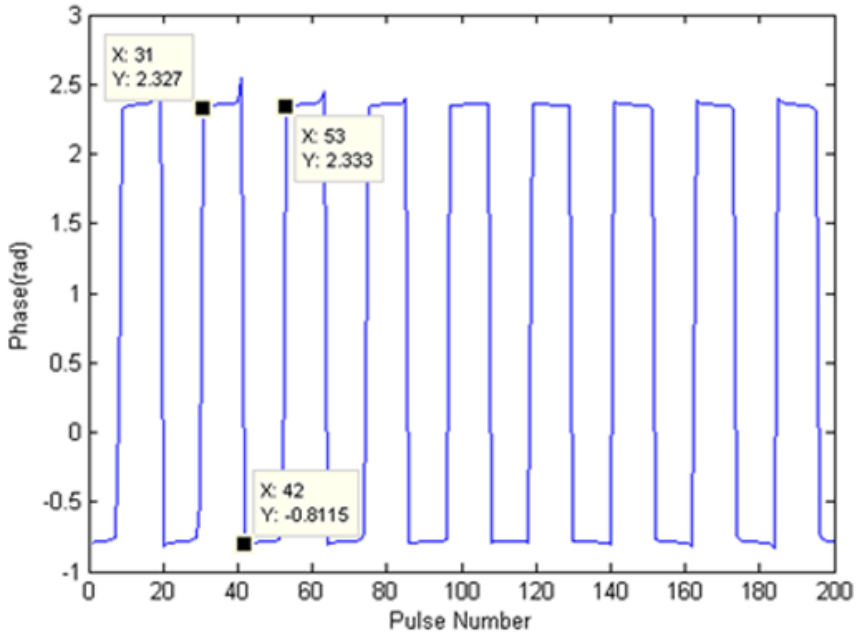

Figure 4.7 Azimuth angle slice of the moving target.

One azimuth angle slice of the moving target shown in Figure 4.6 (a) is shown in Figure 4.7. This figure is generated by computing (using Matlab) the phase along a horizontal line range=900 m in Figure 4.6 (a). The half period of the rectangular function is 11 pulses, which equals the peak pattern period measured by magnitude plot.

Figure 4.8 shows the effect on the peak pattern when the target radial velocity increases. In the cases presented, the target is moving away from the radar. All the parameters are the same as in Table 4.1 except that four different radial velocities are used

$$v_r = 0.3 + l \cdot \frac{\lambda}{4 \cdot \mathrm{PRT}} \quad l = 1,2,3,4 \tag{4.23}$$

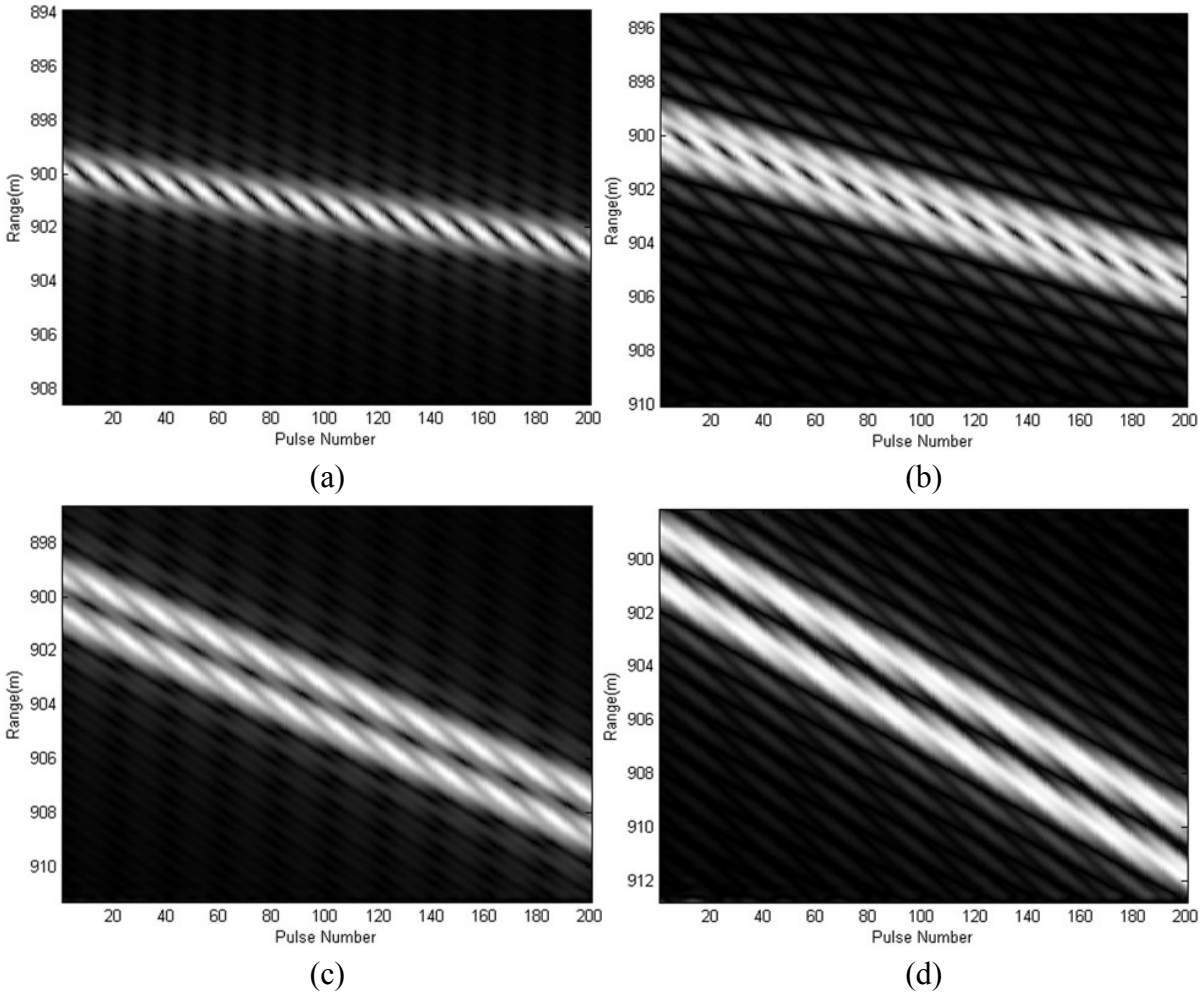

Figure 4.8 Peak patterns of the triangularly modulated signal when the radial speed of target increases (l is the ambiguity index). (a) l=1.(b) l=2. (c) l=3. (d) l=4.

As can be observed from Figure 4.8(a), when the radial velocity is $0.3+\frac{\lambda}{4\cdot \mathrm{PRT}}$ (ambiguity index $l=1$), a clear peak pattern still exists because the two sinc functions as previously shown in Figure 4.5 are still very close to each other. However, the separated parts of the sinc mainlobes begin to appear at both ends of the peak pattern and the tilt of the target azimuth trajectory begins to be recognized. With the increasing of the velocity, the two peaks begin to separate and the patterns between the separated parts become narrower. In Figure 4.8(d), the radial velocity is a little faster than the threshold of a fast

moving target defined by (4.15), hence the two peaks are completely separated from each other.

Moving targets with increasing radial speeds starting from very small value to larger values are shown in Figure 4.6 and Figure 4.8. In all the cases, the moving target can be detected, which validates the universality of the proposed MTI method.

4.5.2 Real Data

The FMCW SAR introduced in Chapter 3 was used to collect data to verify the effectiveness of the proposed MTI method. The high coherence of the SAR makes it possible to accurately analyze the azimuth phase history. A high PRF ensures the high update rate of the speed information. The FMCW SAR parameters during the data collection and the signal processing parameters are shown in Table 4.2. The same radar configuration shown in Figure 3.17 was used in this test.

Table 4.2 Radar parameters for MTI

Parameter	Value	Unit
Bandwidth	150	MHz
Carrier frequency	5590	MHz
PRF	250	Hz
ADC rate	2	Msamples/second
FFT length	8192	Points
Frequency resolution	250	Hz
FFT weighting function	rectangular	

4.5.2.1 Slow moving target

Figure 4.9 shows a comparison of the moving target and stationary target in both TM sweep and SM sweep cases. No window is applied before FFT (uniformly weighted). In

Figure 4.9, the van gradually stopped for traffic lights. The major target shown was an opportunity stationary target located on one side of the driving path. Figure 4.9 (a) is the FFT result of the IF signal when transmitting SM-LFM signal and Figure 4.9 (b) is the FFT result when triangular modulation and the proposed MTI method is used. In the left part of Figure 4.9 (b), the radar is still moving, hence a clear peak pattern can be observed. With the decreasing of the speed of the van, the period of the pattern becomes longer. After the van fully stopped, the pattern disappears and the target trajectory becomes solid (the right end of Figure 4.9 (b)).

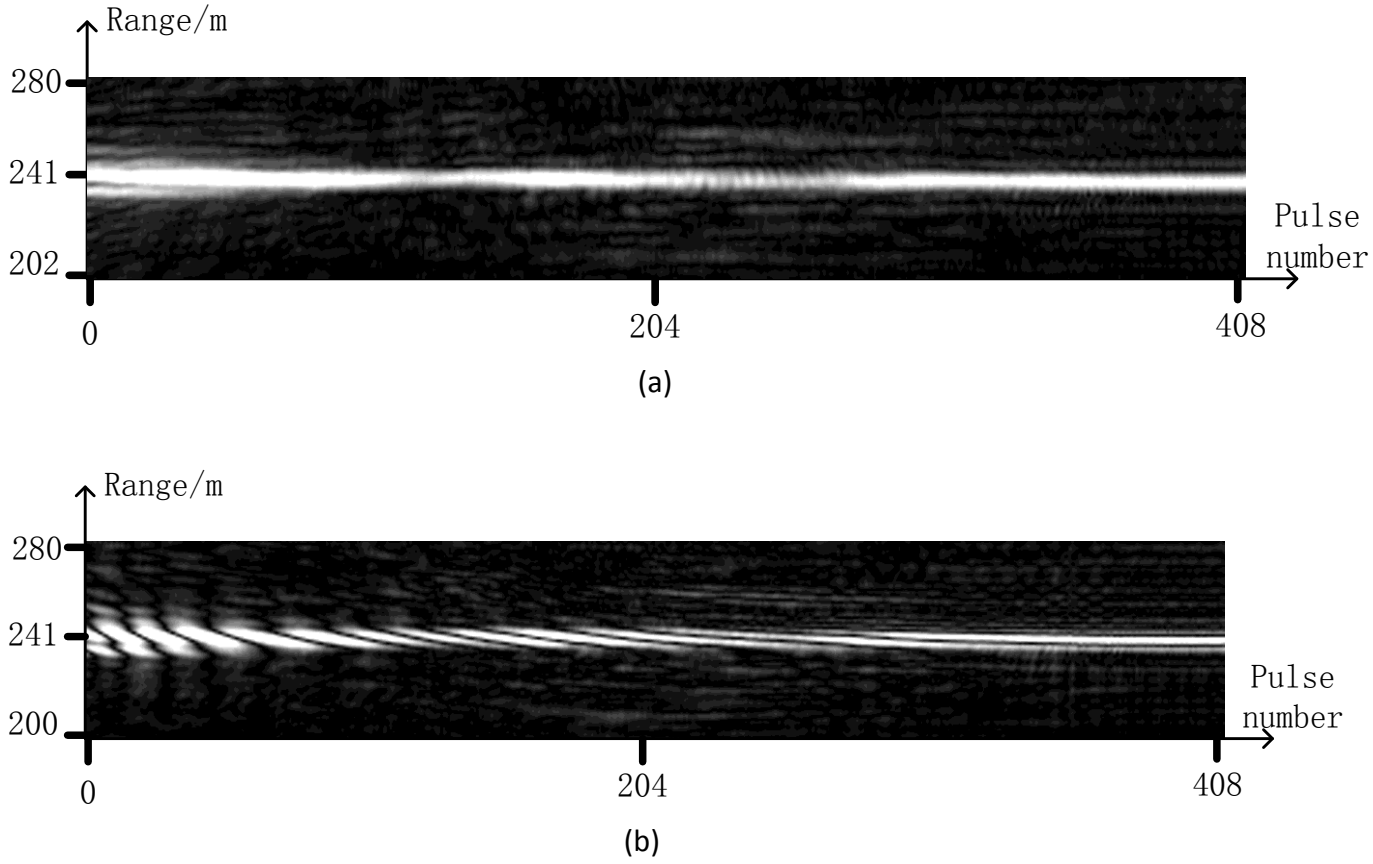

Figure 4.9 Peak patterns from moving radar that is gradually stopped. (a) SM signal. (b) TM signal.

The azimuth trajectory of a stationary target observed by the moving SAR with a constant speed is shown in Figure 4.10.

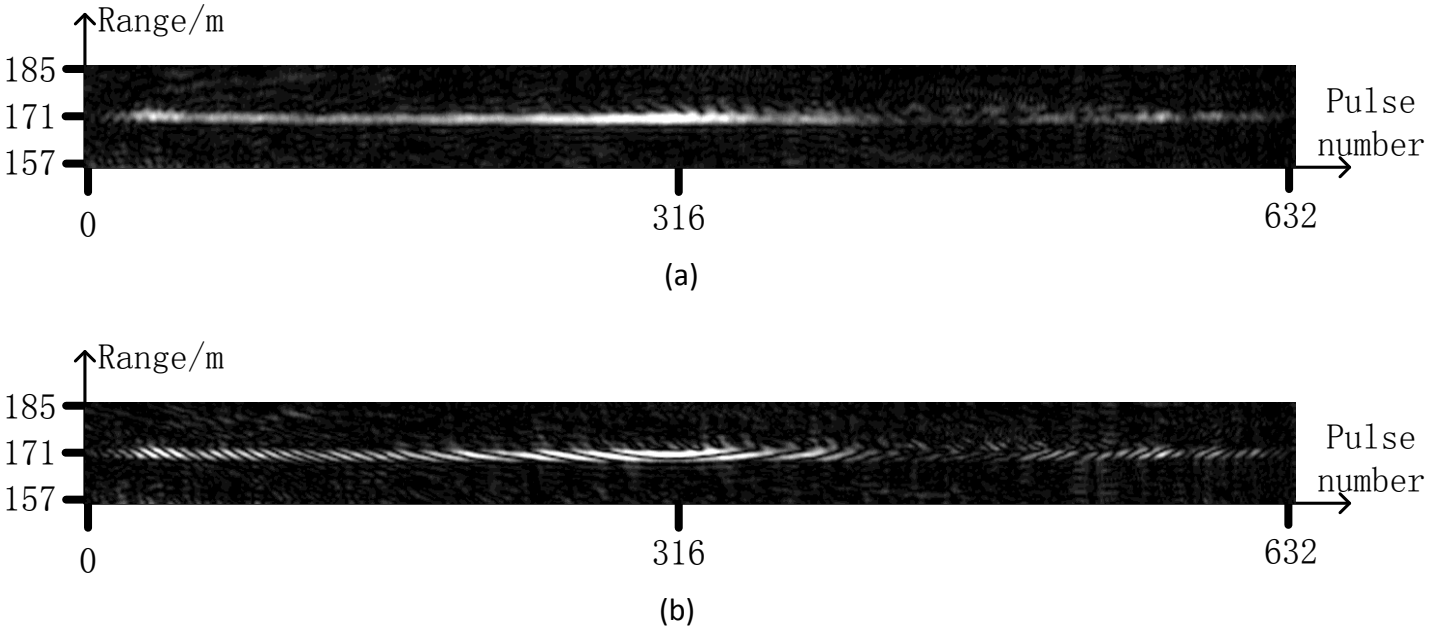

Figure 4.10 Azimuth trajectory of a stationary target when the radar moves with constant speed. (a) SM signal. (b) TM signal.

The radar broadside looks to one side of the vehicle. Therefore, for a stationary target located on one side of the moving path, the radar first approaches the target and then leaves. In this situation, the radial speed first decreases in one direction and then increases in the opposite direction. This can be observed on the right and the left side of Figure 4.10(b), where the moving direction of the peaks inside one pattern period is opposite. In the middle of Figure 4.10(b), the relative radial velocity of the radar is normal to the line of sight of the antennas, thus the radar is relatively stationary versus the target at the moment. Therefore, the peak pattern in the middle of Figure 4.10(b) stays unchanged for a short interval.

Two different methods will be used to calculate the radial speed when the target just enters the antenna beam. The results are compared to verify the speed measurement of the proposed method.

The first method calculates the radial speed using observing geometry. The antenna azimuth beamwidth Bm is about 0.1536 rad, and the closest approach distance R_0 (the distance between target and the moving path of the van) is 171 m (measured from SAR recorded data). The length of the target trajectory is 600 pulses (measured from data), which corresponds to 2.4 s. Hence the relative radial velocity when the target is just illuminated by the antenna beam is

$$v_1 \approx \frac{R_0 \cdot Bm}{600 \cdot PRT} \cdot \frac{Bm}{2} \approx 0.84 \ m/s \quad . \tag{4.24}$$

In (4.24), the numerator of the first fraction ($R_0 \cdot Bm$) is the distance traveled by the car while illuminating the target. The denominator ($600 \cdot PRT$) represents the time that the car used to travel this distance. Hence the first fraction calculates the speed of the vehicle. The second term ($Bm/2$) is the approximated sine value of the incident angle from boresight at the edge of the aperture. Therefore, the product of the first fraction and the second fraction gives the instantaneous radial speed when the target just illuminated by the antenna.

The second is the method proposed in this chapter. The azimuth phase slice of the target shown in Figure 4.10(b) is shown in Figure 4.11. Ten orders of interpolation are applied to the frequency domain signal in azimuth to more accurately reveal the phase.

The phase on the left side of Figure 4.11 is clearer than the phase on the right side. The same phenomenon can also be observed from the amplitude plot shown in Figure

4.10(b) where the peak pattern on the right half side of the figure is not as clear as that on the left side. One possible reason it that the right side signal is interfered with by other reflections.

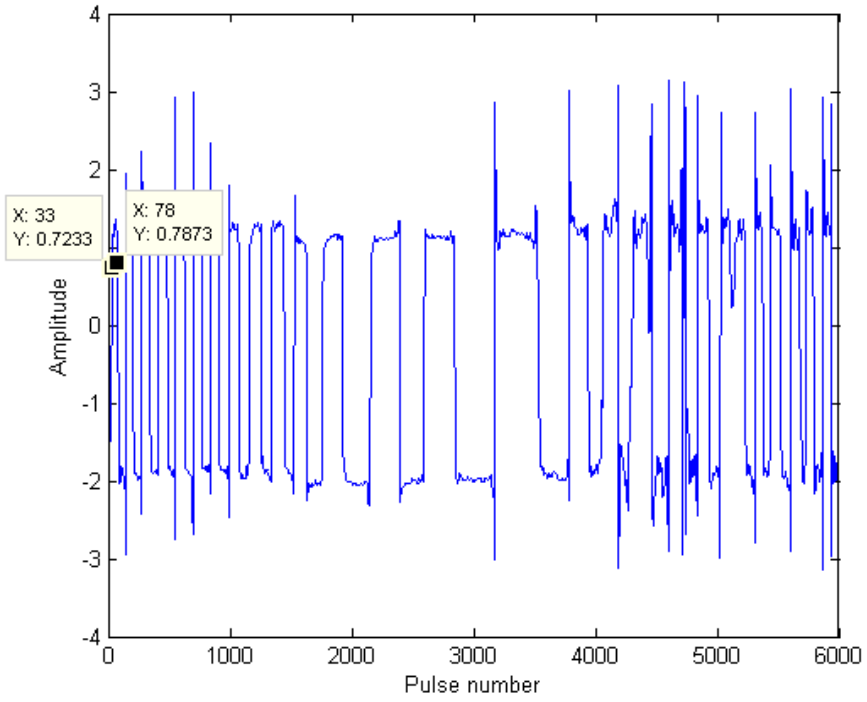

Figure 4.11 Azimuth phase slice of Figure 4.10(b)

The period of the peak pattern at the beginning of the target azimuth trajectory is measured as 45 pulses, which corresponds to 45/10=4.5 pulses before interpolation because ten orders of interpolation has been performed in the azimuth direction. Eq. (4.20) is then used to calculate the radial speed as 0.75 m/s, which is close to the speed obtained in (4.24) by using the geometry.

The radial speeds calculation results by using the above two different methods are very close. This validates that the proposed method can correctly measure the velocity of the moving target when the ambiguity index equals zero.

4.5.2.2 Fast moving target

The results for fast moving targets from the real data are shown in Figure 4.12.

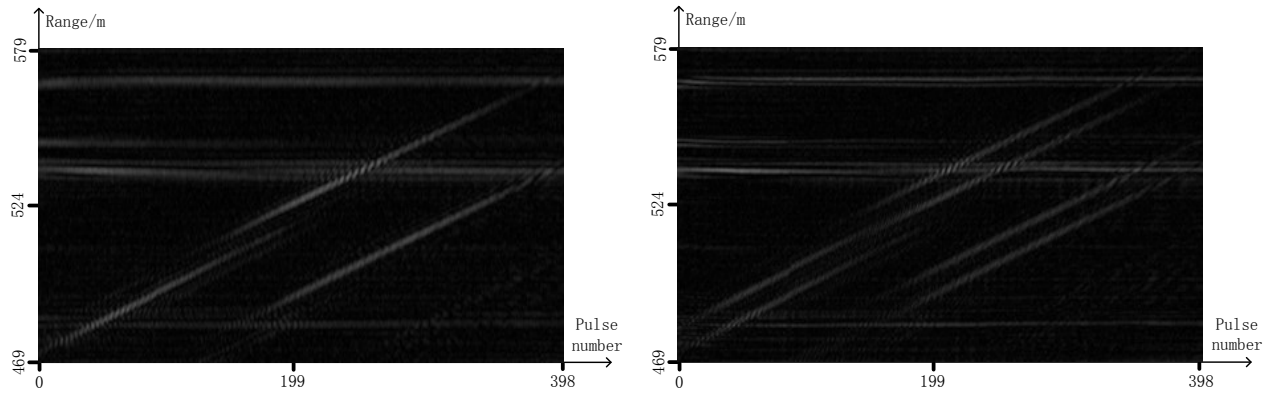

(a) (b)

Figure 4.12 Fast moving targets. (a) SM signal. (b) TM signal

The data are collected when the van was waiting for traffic light. The radar was stationary during the data collection, which can be observed by the horizontal solid lines in Figure 4.12(b) because no peak pattern is presented.

From Figure 4.12(a) we can see that three fast moving targets, which are represented by the three sloped lines, are captured by the radar. In Figure 4.12(b), each of these targets is represented by two sloped lines because their speeds are high enough to cause significant Doppler shifts. According to (4.14), the Doppler effect will move the two sinc peaks to opposite directions and hence separates them in frequency (range) direction.

4.6 Summary

This chapter corresponds to Contributions 2 and 3 in Section 1.3: A mathematical model has been proposed to analyze the TM-LFM signal as one integral signal, which is treated as two separated SM signals in traditional methods. As an application of the new

model, an MTI method is proposed. This MTI method is especially useful for slow moving target detection. Stationary targets, slow moving targets and fast moving targets can be detected altogether. The high coherency of the phase between different pulses provided by the SAR system was not used to improve the azimuth resolution in this MTI method, but used to reveal the peak pattern of a moving target along azimuth.

For the slow moving target, the moving direction can be determined by the moving direction of the peaks inside one period of the peak pattern; the radial speed can be calculated by the repetition period of the peak pattern. However, the velocity calculation for slow moving target is only applicable and accurate when the ambiguity index equals zero. Simulation and actual data acquired by the customized FMCW SAR system are used to demonstrate the effectiveness of the proposed method. Although the MTI method is demonstrated by the data collected from an FMCW radar, it can also be applied in pulse compression radar systems as long as triangular modulation and dechirp-on-receive is used. Since the targets in the real data are all opportunity targets without recorded ground truth, the error of the speed calculation could not be evaluated at this stage. The refinement could be done as future work.

CHAPTER 5. FOCUSING FMCW BISTATIC SAR SIGNALS BY A MODIFIED RMA BASED ON FRESNEL APPROXIMATION

5.1 Background and Literature Review

Bistatic SAR configuration is to separate and mount the transmitter and the receiver of a SAR system on different carrier platforms. The purpose of doing this in pulse SAR system is to increase the information and flexibility of SAR imagery. This technique can also be used in FMCW SAR to increase the isolation between the transmitter and the receiver, so that the transmitted power of a bistatic FMCW SAR can be significantly increased, which leads to longer imaging range. As the developments in the FMCW SAR techniques and UAV synchronized flying, the bistatic FMCW SAR is highly possible to be realized in the near future. The bistatic FMCW SAR model as well as the modified range migration algorithm (RMA) proposed in this section prepared the theory basis for the bistatic FMCW SAR signal processing. The modified RMA can also be used as a versatile and efficient signal processing method in monostatic FMCW SAR as well.

The development of the imaging algorithms for the pulse bistatic SAR has been an important branch in the SAR signal processing. The difficulty of bistatic SAR imaging lies in the fact that the instantaneous slant range is no longer a single square root form as previously shown in (2.33). Two square roots separately caused by the transmitter and the receiver appear in the slant range expression. This changes the slant range equation from the hyperbola in monostatic SAR case to the flattop hyperbola [51] in bistatic case, which invalids most of the existing monostatic SAR imaging algorithms because the signal model of bistatic SAR is changed.

The two dimensional spectral model of the pulse bistatic SAR is the basis of developing imaging algorithms. The complication of the bistatic configuration makes it hard to directly derive a closed form of the spectral model for image formation. In [52] and [53], a numerical method is used to calculate the spectrum. The problem of the numerical method is that it does not support the development of different imaging algorithms because there is no signal model for analysis in numerical method. In [51], [54] and [55], some approximations are used to develop the spectral models. The existing imaging methods in pulse monostatic SAR have been extended to process the pulse bistatic SAR data [56]-[61].

Some of the results and methods developed in pulse bistatic SAR have been introduced into the signal processing of the FMCW bistatic SAR [62], [63]. In addition to all the advantages brought by the pulse bistatic SAR, such as more image information, more flexible configurations, FMCW bistatic SAR offers a new way to overcome the inherent shortcoming of the energy feedthrough in monostatic FMCW SAR. However, as in the monostatic FMCW SAR, the in-pulse Doppler effect still exists in the bistatic FMCW SAR imaging, which complicates the signal model. Moreover, this in-pulse Doppler effect can be more severe as the various bistatic configurations push the SAR parameters to extreme cases such as extremely wide beamwidth or high squint angel imaging.

The two dimensional spectrum of bistatic FMCW SAR has been studied in [62], [63]. In [63], an approximated bistatic slant range equation was used to express the demodulated signal. The spectrum was then obtained by treating the azimuth Doppler frequency as two parts caused by the transmitter and the receiver separately. Reference [62] used a more accurate slant range approximation which considers the movement of the

receiver during the wave propagation. Two separated square roots were obtained in the two dimensional spectrum due to the consideration of the separately introduced azimuth Doppler by the transmitter and the receiver.

In this chapter, Fresnel approximation [54] is used to approximate the dual square roots in bistatic FMCW SAR slant range expression to a single monostatic-like square root so that the existing imaging algorithms in FMCW SAR can be applied to bistatic FMCW SAR without significant modification.

The range migration algorithm (RMA) is a widely used SAR imaging algorithm. The RMA had its origin from seismic processing and was extended into SAR signal processing by [40]-[42] in the 1980s. It was then extended to be integrated with motion compensation [64] or autofocus [65], [66] in pulse SAR image generation.

The RMA was introduced into FMCW monostatic SAR signal processing in [67], [68] by using a more accurate slant range expression. It is one of the preferred algorithms in FMCW SAR processing because the dechirp-on-receive demodulation readily transforms the raw data to the equivalent range frequency domain, reducing the number of FFTs required to obtain the two dimensional spectrum to one (two FFTs are normally required in pulse SAR to generate two dimensional spectrum).

Due to the special signal characteristics of the FMCW SAR, the application of RMA can be made more efficient by using the modified RMA proposed in this chapter. The modified RMA reduces the data size used in the traditional RMAs, which improves the processing speed and reduces the required memory size. The modified RMA also generates better focused images than the traditional RMA if the same size of spectrum is used (see Section 5.4.2.1).

This chapter is organized as follows. In Section 2, the monostatic-like spectrum for FMCW bistatic SAR is derived by using Fresnel approximation. A modified RMA based on the spectrum obtained in Section 2 is proposed in Section 3. The proposed spectral model and the modified RMA are verified in Section 4 by simulation. Then the real data collected by the customized FMCW SAR are used to verify the proposed RMA. A summary for this chapter is given in the last section.

5.2 Two Dimensional Spectrum of FMCW Bistatic SAR Based on Fresnel Approximation

The geometry of the general FMCW bistatic SAR is shown in Figure 5.1.

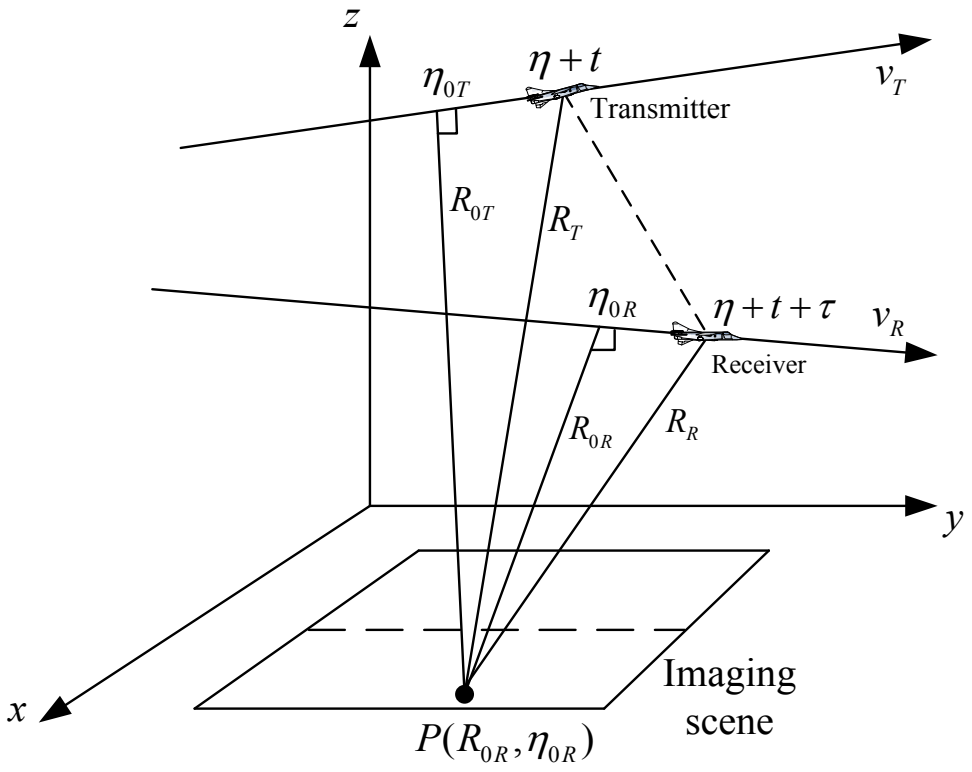

Figure 5.1 Geometry of FMCW bistatic SAR

In Figure 5.1, $P\left(R_{0R,}\eta_{0R}\right)$ is a point target in the imaging scene shown by the parallelogram. The transmitter moves with a constant speed v_T, and the receiver moves with speed v_R. The closest approach distance between the transmitter and the target is R_{0T} occurring at $\eta=\eta_{0T}$, and is R_{0R} between the receiver and the target when $\eta=\eta_{0R}$, where η is the azimuth time (slow time). Due to the longer pulse duration in FMCW SAR, the traditional start-stop assumption is no longer a good approximation, and the movement of the aircrafts inside the pulse needs to be considered [35], [36]. Therefore, in Figure 5.1, the transmitter is assumed to begin to transmit a certain frequency at time $\eta+t$, where t is the fast time. After time τ, the transmitted wave is reflected and arrives at the receiver. Therefore, the total time used for the propagation of the radio wave is

$$\tau\left(t,\eta\right)=\frac{R_R+R_T}{c}=\frac{1}{c}\left(\sqrt{R_{0R}^2+v_R^2\left(\eta+t+\tau-\eta_{0R}\right)^2}+\sqrt{R_{0T}^2+v_T^2\left(\eta+t-\eta_{0T}\right)^2}\right). \quad (5.1)$$

By contrast with the monostatic case previously shown in (2.48), two square roots appear in (5.1). A good approximation that keeps the two square root terms symmetric is to neglect τ in the first square root on the right hand side of (5.1), which means neglecting the movement of the receiver during the propagation of the transmitted wave. The error of this omission is normally a few millimeters in airborne applications [27], hence the approximation is valid for most airborne SAR cases. A more accurate approximation for the slant range is found in [67]. The slant range after approximation is

$$R\left(t,\eta\right)=R_R+R_T=\sqrt{R_{0R}^2+v_R^2\left(\eta+t-\eta_{0R}\right)^2}+\sqrt{R_{0T}^2+v_T^2\left(\eta+t-\eta_{0T}\right)^2}. \quad (5.2)$$

Since $R(t,\eta)$ is always positive, by first squaring $R(t,\eta)$ and then taking the square root [54], the result is

$$R=\sqrt{\begin{array}{l}R_{0R}{}^2+R_{0T}{}^2+v_R{}^2(\eta+t-\eta_{0R})^2+v_T{}^2(\eta+t-\eta_{0T})^2\\+2\sqrt{R_{0R}{}^2R_{0T}{}^2+R_{0R}{}^2v_T{}^2(\eta+t-\eta_{0T})^2+R_{0T}{}^2v_R{}^2(\eta+t-\eta_{0R})^2+v_R{}^2(\eta+t-\eta_{0R})^2v_T{}^2(\eta+t-\eta_{0T})^2}\end{array}} \tag{5.3}$$

For long range operation and narrow antenna beamwidth, we have $R_{0R} \gg v_{0R}\left(\eta+t-\eta_{0R}\right)$ and $R_{0T} \gg v_{0T}\left(\eta+t-\eta_{0T}\right)$, thus the last term in the inner square root of (5.3) can be neglected. Apply the Fresnel approximation to the inner square root and after some manipulations (Appendix B), we have

$$R(t,\eta)=2\sqrt{R_0^2+v^2\left(\eta+t-\eta_c\right)^2+\delta} \tag{5.4}$$

where

$$\begin{aligned}R_0 &= \frac{R_{0R}+R_{0T}}{2}\\ v &= \frac{1}{2}\sqrt{\frac{R_{0R}+R_{0T}}{R_{0R}R_{0T}}\beta}\\ \eta_c &= \frac{R_{0R}\eta_{0T}v_T^2+R_{0T}\eta_{0R}v_R^2}{\beta}\\ \delta &= \frac{v_R^2v_T^2\left(R_{0R}+R_{0T}\right)\left(\eta_{0R}-\eta_{0T}\right)^2}{4\beta}\\ \beta &= R_{0R}v_T^2+R_{0T}v_R^2\end{aligned} \tag{5.5}$$

R_0, v and η_c are the equivalent closest approach distance, velocity and azimuth Doppler centre that are similar to the monostatic parameters. The equivalent speed v is the function of the range in the new model, which is different from the normal airborne SAR cases. Eq. (5.4) is very similar to the instantaneous slant range expression of the monostatic

FMCW SAR shown by (2.48) except for the last term δ inside the square root, which is caused by the bistatic configuration.

The error of using (5.4) to approximate (5.2) is shown in Figure 5.2 by using the parameters shown in Table 5.1.

Table 5.1 Approximation error calculation parameters

Parameter	Value	Unit
Closest range from receiver to target	16	km
Closest range from transmitter to target	20	km
Receiver speed	50	m/s
Transmitter speed	60	m/s
Closest approach time of receiver	0	s
Closest approach time of transmitter	1	s
Slow time	8	s

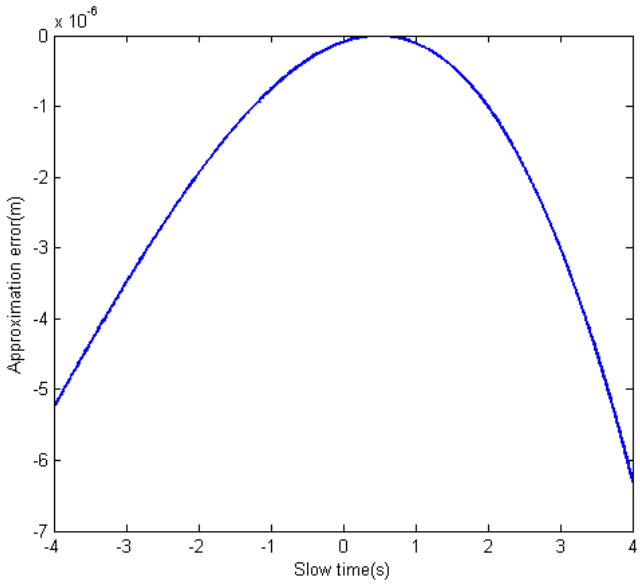

Figure 5.2 Slant range approximation error

As shown by Figure 5.2, the maximum error is about -6.3×10^{-6} m. In a C-band bistatic SAR with 0.06 m wavelength, this maximum error will introduce a phase error of

$4\pi \cdot \left(-6.3\times10^{-6}\right)/\lambda = 0.001$ rad , which can be neglected and will not influence the image formation process.

Using the monostatic-like expression, the two-way propagation delay can now be expressed as

$$\tau\left(t,\eta\right) = \frac{R\left(t,\eta\right)}{c} \quad . \tag{5.6}$$

Then the IF signal of the FMCW bistatic SAR after dechirp-on-receive demodulation can be expressed as

$$s\left(t,\eta\right) = \sigma\left(R_{0R,}\eta_{0R}\right) rect\left(\frac{t}{T}\right) rect_a\left(\frac{\eta-\eta_{0R}}{T_a}\right) \exp\left(j2\pi f_0\tau + j2\pi k\tau t - j\pi k\tau^2\right) \tag{5.7}$$

where $\sigma\left(R_{0R,}\eta_{0R}\right)$ is the reflection coefficient of the point $P\left(R_{0R},\eta_{0R}\right)$ in Figure 5.1, k is the FM rate of the transmitted signal, T is the PRT, T_a is the aperture length, and f_0 is the centre frequency. The last exponential term is the residual video phase (RVP), and is normally very small and can be neglected in narrow scenes imaging [33] (Page 144). It can also be removed before image generation. A method that removes RVP is given in [33] (Page 501). This term is not the focus of this dissertation and is assumed to be removed from now on and will not be included in the following derivation.

Because of the characteristics of the chirp signal, the dechirp-on-receive process has readily transformed the signal into its equivalent range frequency domain, hence only one azimuth FT is needed to obtain the two dimensional spectrum. Substitute (5.4), (5.6) into (5.7) and perform CTFT about η in (5.7), we have

$$S\left(t,f_\eta\right)=\sigma\left(R_{0R,}\eta_{0R}\right)rect\left(\frac{t}{T}\right)\int rect_a\left(\frac{\eta-\eta_{0R}}{T_a}\right)\exp\left(j\phi\left(t,\eta\right)\right)\exp\left(-j2\pi f_\eta\eta\right)d\eta \quad (5.8)$$

where

$$\phi\left(t,\eta\right)=\frac{4\pi}{c}\left(f_0+kt\right)\cdot\sqrt{R_0^2+v^2\left(\eta+t-\eta_c\right)^2+\delta} \quad (5.9)$$

is the phase of (5.7). Principle of stationary phase (POSP) can be used at this stage to find the azimuth phase stationary point. By solving $d\left(\phi\left(t,\eta\right)-2\pi f_\eta\eta\right)/d\eta=0$, we have

$$\left(\eta-\eta_c+t\right)^2=\left(\frac{cf_\eta\sqrt{R_0^2+\delta}}{2v^2\left(kt+f_0\right)\sqrt{1-\frac{c^2f_\eta^2}{4v^2\left(kt+f_0\right)^2}}}\right)^2. \quad (5.10)$$

then we obtain

$$\eta=\frac{cf_\eta\sqrt{R_0^2+\delta}}{2v^2\left(kt+f_0\right)\sqrt{1-\frac{c^2f_\eta^2}{4v^2\left(kt+f_0\right)^2}}}+\eta_c-t \quad (5.11)$$

.

The positive sign is selected when taking square root of the right hand side of (5.10). This is because in (5.9), $f_\eta=d\phi\left(t,\eta\right)/\left(2\pi\cdot d\eta\right)$ can be used to calculate the azimuth frequency. Then it can be obtained that the azimuth frequency is approximately proportional to the azimuth time η (not $-\eta$).

An approximated closed form of the integral in (5.8) can be obtained and the equivalent two dimensional spectrum can be expressed as

$$S\left(t,f_\eta\right)=\sigma\left(R_{0R,}\eta_{0R}\right)rect\left(\frac{t}{T}\right)rect_a\left(\frac{f_\eta+k_{aB}\eta_c-k_{aB}\eta_{0R}}{k_{aB}T_a}\right)\exp\left(j\Phi\left(t,f_\eta\right)\right) \quad (5.12)$$

where

$$\Phi\left(t, f_\eta\right) = \frac{4\pi\alpha R_0}{c}\sqrt{\left(f_0 + kt\right)^2 - \frac{c^2 f_\eta^2}{4v^2}} + 2\pi f_\eta t - 2\pi f_\eta \eta_c \tag{5.13}$$

and

$$\alpha = \sqrt{1 + \frac{v_R^2 v_T^2}{2R_0\beta}\left(\eta_{0R} - \eta_{0T}\right)^2} \tag{5.14}$$

.

The approximation

$$\eta = \frac{cf_\eta\sqrt{R_0^2 + \delta}}{2v^2\left(kt + f_0\right)\sqrt{1 - \frac{c^2 f_\eta^2}{4v^2\left(kt + f_0\right)^2}}} + \eta_c - t \approx \frac{c\sqrt{R_0^2 + \delta}}{2v^2 f_0\sqrt{1 - \frac{c^2 f_\eta^2}{4v^2 f_0^2}}} f_\eta + \eta_c \approx \frac{1}{k_{aB}} f_\eta + \eta_c \tag{5.15}$$

where

$$k_{aB} = \frac{2v^2}{\lambda\sqrt{R_0^2 + \delta}} \tag{5.16}$$

has been used in the azimuth envelop $rect_a$ in (5.12) to show the position in the azimuth spectrum. The similar approximation has been used and discussed in Section 2.2.3.2. k_{aB} is the equivalent azimuth FM rate in bistatic SAR.

Eq. (5.12) is an 'equivalent' two dimensional spectrum in that it still has range time t as one dimension, and hence is not a true two dimensional spectrum in the strict sense. However, the signal form in this t domain is similar to that in the frequency domain obtained by the range FT of fully compressed range signals [33] (Page 402). Therefore, (5.12) is named as equivalent two dimensional spectrum expression.

From the azimuth envelop shown in (5.12), we can see that the azimuth signal normally has a non-zero Doppler centre because $\eta_c \neq \eta_{0R}$. This is because the moving of the transmitter still causes azimuth Doppler frequency shift when the receiver is at the closest approach position.

The first term in (5.13) is the equivalent FMCW bistatic SAR square root term. A closer view of the terms in (5.13) could help to understand the major components and the physical interpretation of the equivalent monostatic phase. By expanding the square root in (5.13) about t using Taylor expansion and after some manipulations, we have

$$\Phi\left(t, f_\eta\right) = \frac{4\pi\alpha R_0}{c}\left[f_0 D\left(f_\eta, v\right) + \frac{kt}{D\left(f_\eta, v\right)} - \frac{k^2 t^2 c^2 f_\eta^2}{8v^2 f_0^2 D^3\left(f_\eta, v\right)} + o\left(t^2\right)\right] \\ +2\pi f_\eta t - 2\pi f_\eta \eta_c \tag{5.17}$$

where

$$D\left(f_\eta, v\right) = \sqrt{1 - \frac{c^2 f_\eta^2}{4v^2 f_0^2}} \tag{5.18}$$

represents the cosine of the instantaneous incidence angle of the receiver. $o\left(t^2\right)$ in (5.17) represents the higher order terms in Taylor expansion. The first term in the square brackets of (5.17) represents the azimuth modulation. The second term in the brackets is a linear function of range time when azimuth frequency is fixed, which shifts the position of the range spectrum after range FT and represents the azimuth frequency dependent range cell migration (RCM). The third term in the brackets is the major range-azimuth coupling term, which is normally mentioned as the secondary range compression (SRC) term. The higher order terms are also caused by the range-azimuth coupling and in most airborne SAR configurations are normally very small and can be neglected. However, they could

affect the image quality in some extreme cases [27], where they need to be considered and eliminated. Otherwise, these terms will cause uncompensated phase errors and degrade focusing quality. This is also the reason that RMA is considered to be a very accurate imaging algorithm because it does not make any approximation to the square root of (5.13) but use a Stolt mapping to process the square root. The second term from last is an additional RCM caused by the moving of the radar inside the pulse. The last term is caused by the target azimuth position. The target will be registered to $\eta = \eta_c$ in azimuth in the final image.

5.3 Modified RMA Based on the Bistatic Equivalent Spectrum

The modified RMA follows the traditional RMA steps. The first step is the reference function multiplication (RFM), which focuses the point in the reference range (normally chosen to be the centre range which is shown by the horizontal dashed line inside the parallelogram of Figure 5.1 (not very accurate because the middle of the imaging scene is a little different from the middle of slant range)). This reference function is

$$\exp\left(j\Phi_{RMF}\left(t, f_\eta\right)\right) = \exp\left(-j\frac{4\pi\alpha_{ref}R_{ref}}{c}\sqrt{\left(f_0 + kt\right)^2 - \frac{c^2 f_\eta^2}{4v_{ref}^2}} - j2\pi f_\eta t\right). \quad (5.19)$$

As shown by (5.5), the equivalent bistatic velocity varies with range. Therefore, a

Table 5.2 Parameters for velocity error calculation

Parameter	Value	Unit
Closest range from receiver to scene centre	16	km
Closest range from transmitter to scene centre	20	km
Receiver speed	50	m/s
Transmitter speed	60	m/s
Range swath	4	km

reference velocity needs to be used in this step. This means that the equivalent bistatic velocity is assumed to be the same for all ranges. This is a reasonable approximation because the velocity varies very slowly in long range imaging. Figure 5.3 shows the speed approximation errors using the parameters shown in Table 5.2.

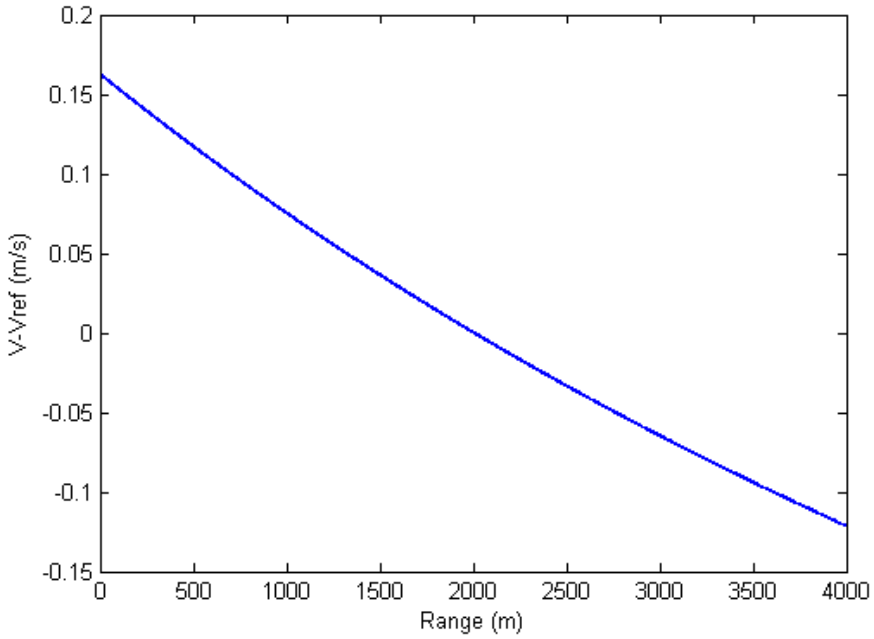

Figure 5.3 Velocity approximation error

The horizontal axis of Figure 5.3 is the distance to the near edge of the imaging scene. The vertical axis represents the velocity approximation error $v - v_{ref}$. The maximum speed error occurs at the closest edge of the scene to the radar, which is a little above 0.15 m/s. The reference velocity can be calculated by (5.5) using the parameters shown in Table 5.2 to be 56.1 m/s. Therefore, the maximum speed approximation error is only 0.29% of the reference velocity, which can be neglected.

The second step of the traditional RMA is the Stolt mapping [5], which is

$$\sqrt{\left(f_0+kt\right)^2-\frac{c^2f_\eta^2}{4v_{ref}^2}}=f_0+kt_1 \tag{5.20}$$

where t_1 is the new time variable. This step corresponds to a re-mapping of the time axis. The implementation of the Stolt mapping in digital signal processing requires interpolation. The spectrum values that correspond to the new variable are obtained by interpolating the original spectrum. The main components of the variable substitution can be obtained by the Taylor series of (5.20). If we Taylor expand the square root in (5.20) about t and take the first two terms of the series, we obtain (5.21), after some manipulations, which shows the main components of the variable substitution

$$t_1=\frac{f_0}{k}\left(D\left(f_\eta,v\right)-1\right)+\frac{t}{D\left(f_\eta,v\right)}. \tag{5.21}$$

In (5.21), we still use $D\left(f_\eta,v\right)$ but not $D\left(f_\eta,v_{ref}\right)$ even in the RFM stage we assume v at all ranges equals to v_{ref}. This is because the variation of v with range still exists in the data. However, since v is very close to v_{ref}, either way will not cause defocusing of the final image.

The first term on the right side of (5.21) is an azimuth frequency dependent time shift, which is the major change of the time variable. This part of the Stolt mapping finishes the azimuth compression operation. The second term is the scaling of time, which corresponds to the correction of RCM. Since $D\left(f_\eta,v\right)$ is always no more than 1, the change of variable always corresponds to an expansion of the spectrum size in time direction. This expansion could be very large when $D\left(f_\eta,v\right)$ is significantly smaller than 1, which could increase the computational load and the memory required for storing the in-

termediate and final results. Moreover, the decrease of focus quality occurs as the change in the value of the variable increases [69], resulting worse SAR images.

The modification of the RMA to decrease the calculation load and improve the image quality takes two steps.

The first step is to modify the mapping formula. Instead of the variable change in (5.20), the following mapping is used

$$\sqrt{\left(f_0+kt\right)^2-\frac{c^2 f_\eta^2}{4v_{ref}^2}}=D\left(f_\eta,v\right)f_0+kt_1 \tag{5.22}$$

.

By making the variable change in (5.22), the first term on the right side of (5.21) vanishes, and the mapping only includes the scaling of the time variable. This mapping eliminates the skew of the spectrum caused by parallel time shift. Similar but different variable changes are used in [64] and [69]. As this modified Stolt mapping performs all the functions of the traditional mapping except for the azimuth compression, the azimuth modulation needs to be removed in range Doppler domain.

The second step to simplify the RMA is achieved by noticing that the 3dB mainlobe width of the spectrum of the IF signal after dechirp-on-receive is only determined by the signal time duration (see Section 2.1.1). Therefore, there is no need to perform the full modified Stolt mapping shown in (5.22), which will expand the new time variable to $\left[-T/2D\left(f_\eta,v\right),T/2D\left(f_\eta,v\right)\right]$. The new variable only needs to be limited in the same range as the old time variable, which is

$$-\frac{T}{2}\le t_1\le\frac{T}{2} \tag{5.23}$$

.

For $D\left(f_\eta, v\right) = 0.9$, 10% more memory is required to perform the Stolt mapping if the second step is not used even when the variable change in (5.22) is employed.

By employing the above two modifications in the Stolt mapping, the data size during and after the mapping can be kept constant, which is important for the real time processing of the low cost FMCW SAR.

After the first two steps of the RMA, the signal can be expressed as

$$\begin{aligned} S_1\left(t_1, f_\eta\right) &= \sigma\left(R_{0R,}\eta_{0R}\right) rect\left(\frac{t_1}{T}\right) rect_a\left(\frac{f_\eta + k_{aB}\eta_c - k_{aB}\eta_{0R}}{k_{aB}T_a}\right) \\ &\cdot \exp\left(j\frac{4\pi\left(\alpha R_0 - \alpha_{ref}R_{ref}\right)}{c}\left(D\left(f_\eta, v\right)f_0 + kt_1\right) - j2\pi f_\eta \eta_c\right) \end{aligned} \tag{5.24}$$

in which the range and azimuth variables have been successfully separated. The range CTFT is then performed and we have

$$\begin{aligned} S_2\left(f_1, f_\eta\right) &= \int S_1\left(t_1, f_\eta\right)\exp\left(-j2\pi f_1 t_1\right)dt_1 \\ &= T\sigma\left(R_{0R,}\eta_{0R}\right)\text{sinc}\left[T\left(f_1 - \frac{2k\left(\alpha R_0 - \alpha_{ref}R_{ref}\right)}{c}\right)\right]\cdot rect_a\left(\frac{f_\eta + k_{aB}\eta_c - k_{aB}\eta_{0R}}{k_{aB}T_a}\right) \\ &\cdot \exp\left(j\frac{4\pi\left(\alpha R_0 - \alpha_{ref}R_{ref}\right)}{c}D\left(f_\eta, v\right)f_0\right)\exp\left(-j2\pi f_\eta \eta_c\right) \end{aligned} \tag{5.25}$$

where f_1 is the new range frequency variable. As implied by the sinc function in (5.25), the range signal has been focused and the RCM has been removed. The next step is to multiply the azimuth matched filter to perform the azimuth compression, which is

$$\exp\left(j\Phi_{ac}\left(f_1, f_\eta\right)\right) = \exp\left(-j\frac{4\pi\left(\alpha R_0 - \alpha_{ref}R_{ref}\right)}{c}D\left(f_\eta, v\right)f_0\right). \tag{5.26}$$

Then we have

$$S_3\left(f_1,f_\eta\right)=T\sigma\left(R_{0R,}\eta_{0R}\right)\mathrm{sinc}\left[T\left(f_1-\frac{2k\left(\alpha R_0-\alpha_{ref}R_{ref}\right)}{c}\right)\right]$$
$$\cdot rect_a\left(\frac{f_\eta+k_{aB}\eta_c-k_{aB}\eta_{0R}}{k_{aB}T_a}\right)\exp\left(-j2\pi f_\eta\eta_c\right) \tag{5.27}$$

An azimuth continuous time inverse Fourier transform (CTIFT) then generates the focused image, which is

$$\begin{aligned}s\left(f_1,\eta\right)&=\frac{1}{2\pi}\int S_3\left(f_1,f_\eta\right)\exp\left(j2\pi f_\eta\eta\right)d\eta\\&=A\sigma\left(R_{0R,}\eta_{0R}\right)\mathrm{sinc}\left[T\left(f_1-\frac{2k\left(\alpha R_0-\alpha_{ref}R_{ref}\right)}{c}\right)\right]\\&\cdot\mathrm{sinc}\left[k_{aB}T_a\left(\eta-\eta_c\right)\right]\exp\left[-j2\pi\left(k_{aB}\eta_c-k_{aB}\eta_{0R}\right)\eta\right]\end{aligned} \tag{5.28}$$

where A is a constant amplitude. The amplitude of the target point is now a two dimensional sinc function and the resolutions are determined by signal fast time duration T in range and azimuth bandwidth $k_{aB}T_a$ in azimuth.

The flow diagram of processing FMCW bistatic SAR signal by using the proposed signal model and the modified RMA is shown in Figure 5.4.

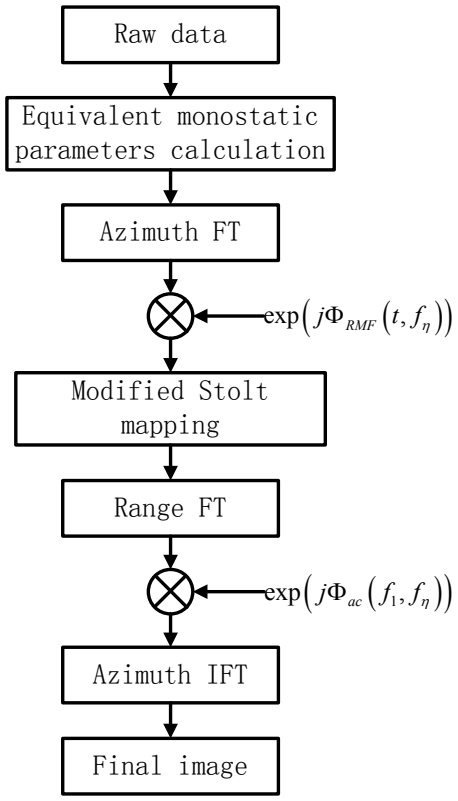

Figure 5.4 FMCW Bistatic SAR signal processing flow diagram

The first step of the signal processing is to calculate the equivalent monostatic parameters from bistatic parameters using (5.5). Then an azimuth FT is used to transform the data into the equivalent two dimensional frequency domain. The RFM is then performed by multiplying the function shown by (5.19). After the RFM, the data is interpolated in range and the proposed Stolt mapping is performed. A range FT is then applied to the spectrum after the proposed Stolt mapping. Then the function of (5.26) is multiplied and an azimuth IFT generates the image.

The proposed RMA can be used in monostatic FMCW SAR signal processing as well. The comparison of the flow diagram of the proposed RMA and the RDA when processing monostatic FMCW SAR is shown in Figure 5.5.

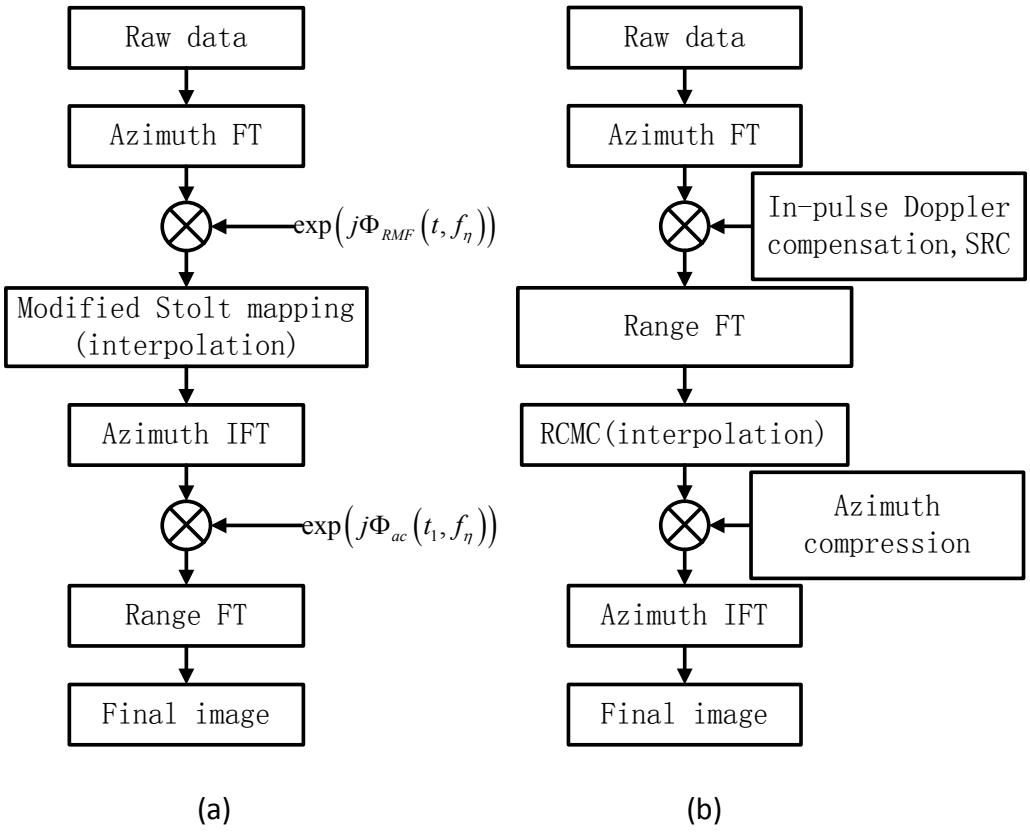

Figure 5.5 Comparison of the proposed RMA and the RDA. (a) Proposed RMA. (b) RDA.

Figure 5.5(a) is the flow diagram of the proposed RMA and Figure 5.5 (b) is that of the RDA. The 'In-pulse Doppler compensation, SRC' step and the 'Azimuth compression' step in Figure 5.5(b) are performed by phase multiplication. As can be observed in Figure 5.5, the proposed RMA has almost the same steps and computational load as RDA. While the traditional RMA is more complex than the RDA and takes longer time to generate images [22].

5.4 Results

The proposed FMCW bistatic SAR spectral model and the modified RMA are verified separately in this section.

Only simulation (no real data for FMCW bistatic SAR were collected) is used in Section 5.4.1 to verify the monostatic-like spectrum for FMCW bistatic SAR. The modified RMA is also validated in Section 5.4.1 to be effective in FMCW bistatic SAR signal processing.

Section 5.4.2 is used to validate the effectiveness of the proposed RMA in monostatic FMCW SAR image generation. Both simulation and real data collected by the customized FMCW SAR are used in this section.

5.4.1 Bistatic Imaging

In bistatic configuration, since the transmitter and receiver are separated and mounted on different platforms, the isolation between them is significantly increased. The transmitted power is no longer limited by the leakage problem in FMCW SAR. Therefore, bistatic FMCW SAR can work at significantly longer range. The simulation parameters are shown in Table 5.3. The transmitter illuminates the imaging scene in spotlight mode while the receiver works in broadside stripmap mode, so that the receiver can receive return echoes when flying over the imaging scene.

Table 5.3 Simulation parameters

Parameter	Value	Unit
Closest range from receiver to scene centre	20.48	km
Closest range from transmitter to scene centre	23.48	km
Receiver speed	50	m/s
Transmitter speed	60	m/s
Center frequency	5	GHz
Signal bandwidth	7.5	MHz
Pulse repetition frequency	220	Hz

Nine point targets are set in the imaging scene as shown in Figure 5.6(a). Point E is the scene centre. Figure 5.6(b) shows the processing result by using the proposed equivalent spectrum (5.12) and the modified RMA.

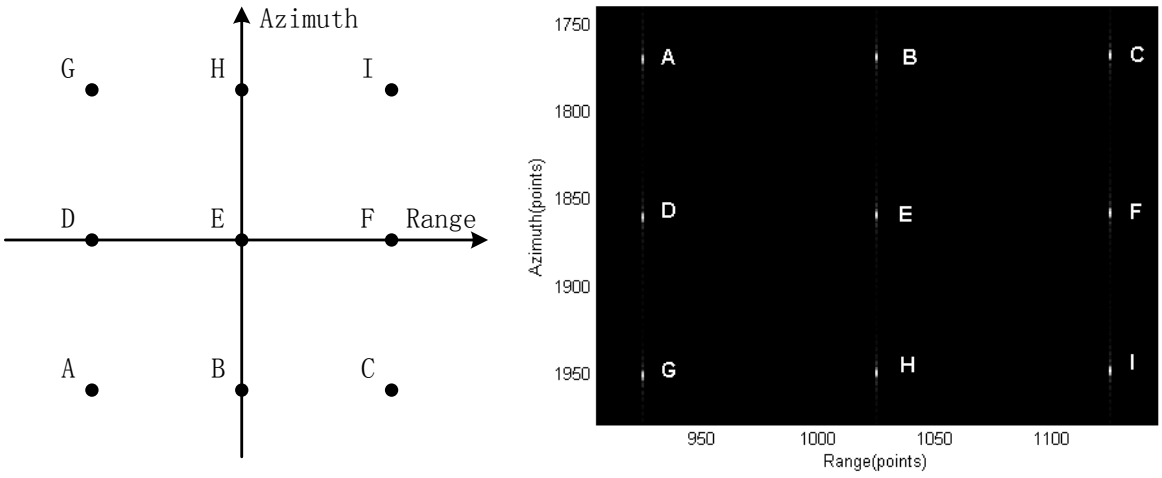

Figure 5.6 Nine targets in the scene. (a) Targets positions. (b) The targets images by using the proposed signal model and the proposed RMA.

Figure 5.7 shows the scene centre point E and Figure 5.8 and Figure 5.9 show the points further from the centre. Interpolation is used to both the range direction and azimuth direction of the amplitude plot of each target to give a better view of the mainlobe and sidelobes. It can be observed from Figure 5.7 - Figure 5.9 that all the targets are well focused and there are minimal differences among the three different targets in contour plots while the magnitude plots look the same.

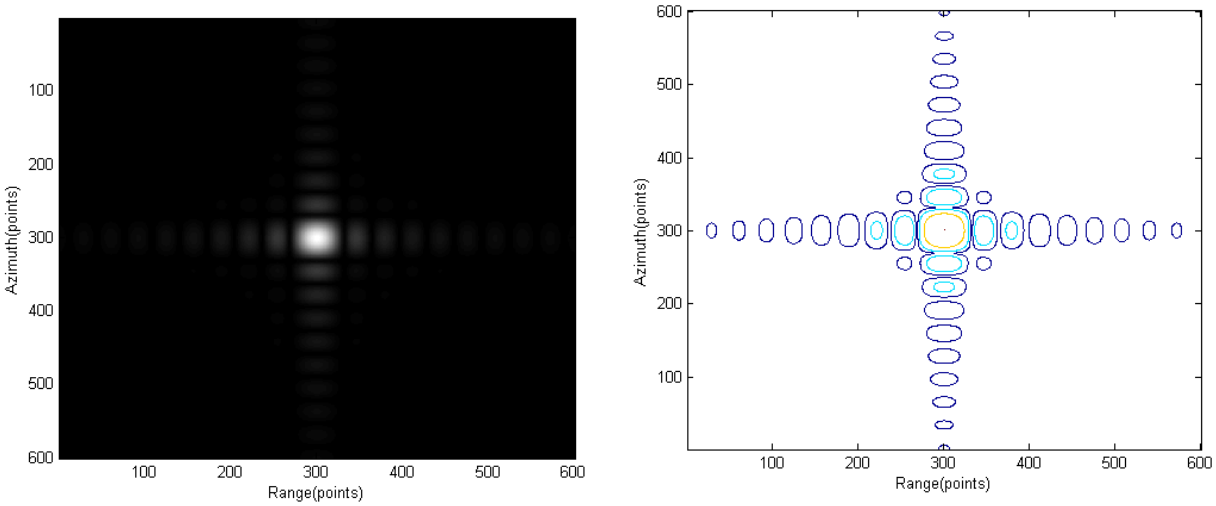

(a) (b)

Figure 5.7 Point E. (a) Amplitude plot. (b) Contour plot.

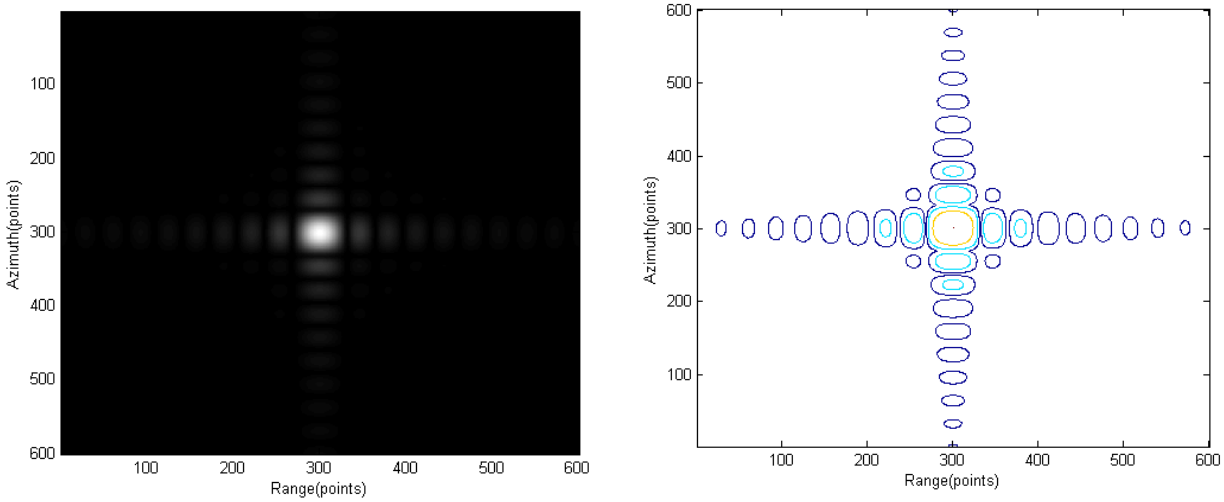

(a) (b)

Figure 5.8 Point G. (a) Amplitude plot. (b) Contour plot.

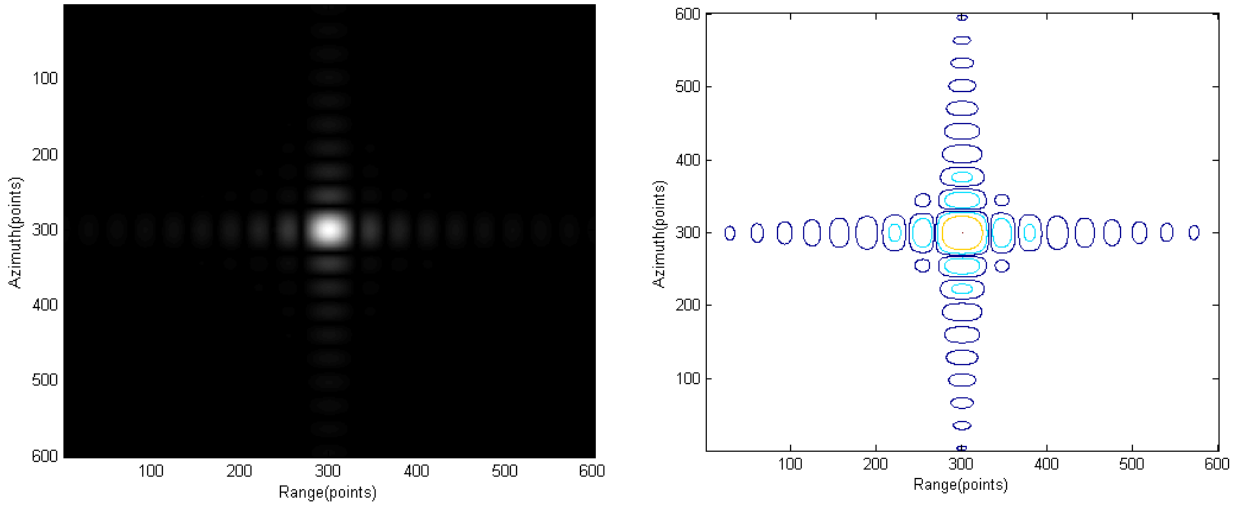

(a) (b)

Figure 5.9 Point C. (a) Amplitude plot. (b) Contour plot.

A range slice and azimuth slice of point C are shown in Figure 5.10. The peak to sidelobe ratio (PLSR) of range and azimuth slices has minimal differences, but all fit well with the PSLR of a sinc function. The range 3 dB mainlobe width is 29 samples and the azimuth 3 dB mainlobe width is 30 samples, which means the range and azimuth resolutions are approximately the same.

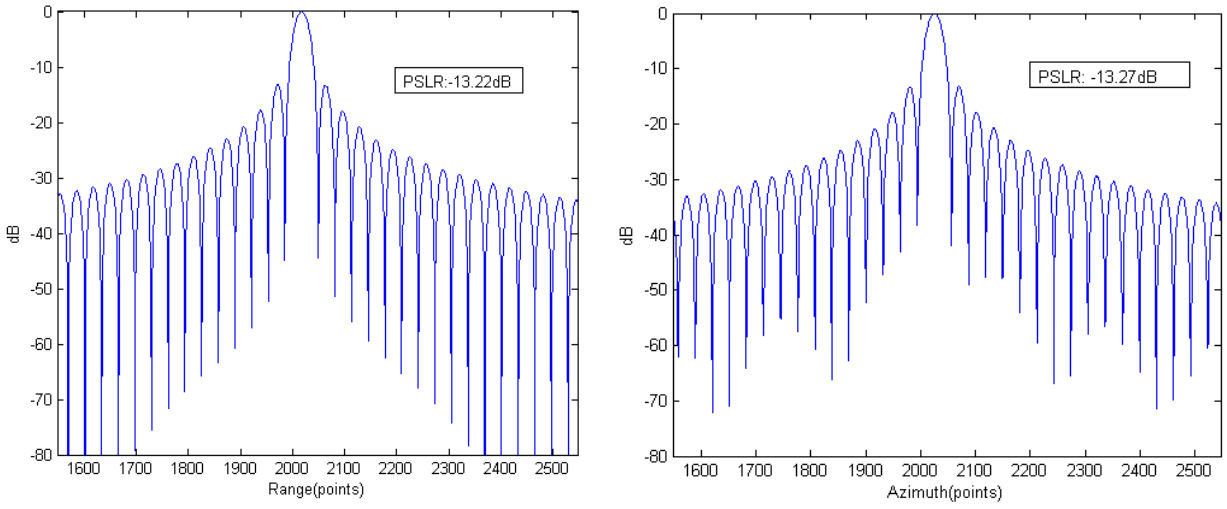

(a) (b)

Figure 5.10 Range and azimuth slices of point C. (a) Range slice. (b) Azimuth slice.

The proposed equivalent two dimensional spectrum (5.12) was used in this simulation to express the spectrum of the simulated bistatic FMCW SAR raw data, and well-focused images were generated. Therefore, eq. (5.12) can be demonstrated by this simulation to be an accurate representation of the two dimensional spectrum of bistatic FMCW SAR under long range and narrow beamwidth operation.

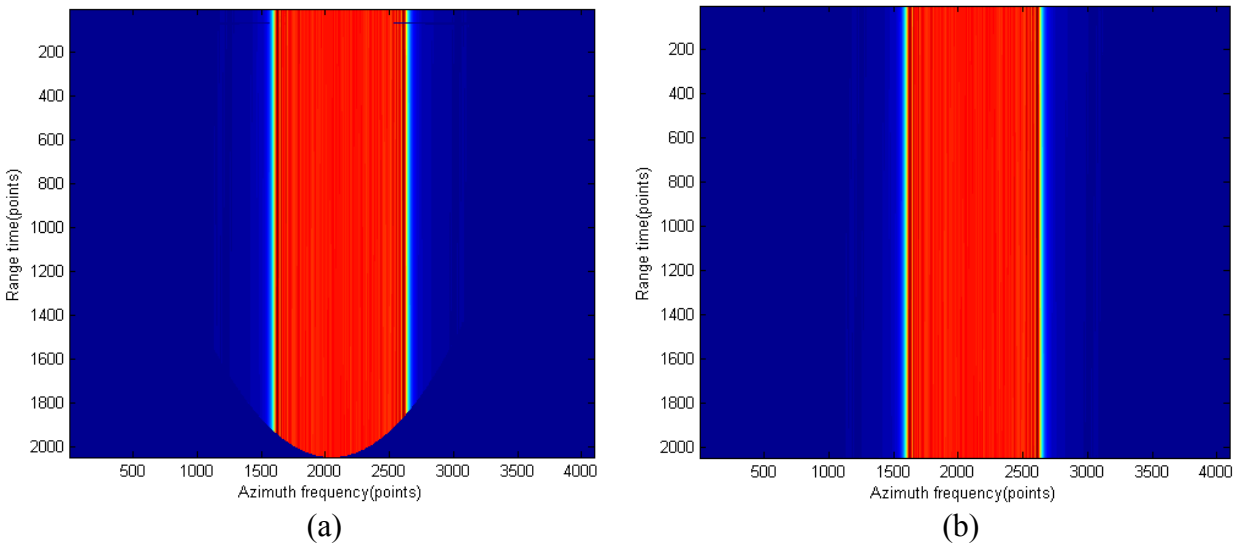

Figure 5.11 Two dimensional spectrum comparison after Stolt mapping. (a) Spectrum after the traditional Stolt mapping. (b) Spectrum after the proposed Stolt mapping.

The comparison of the two dimensional spectrums after Stolt mapping when using the proposed RMA and the traditional RMA is shown in Figure 5.11. The data sizes used in both spectrums during Stolt mapping are the same which are 2048 samples by 4096 samples. As shown by Figure 5.11, the azimuth Doppler centre is not zero even when the receiver works in broadside stripmap mode. This is because the transmitter still causes Doppler shift when the receiver passes the closest approach position.

Figure 5.11(a) shows that the spectrum is skewed because of the traditional Stolt mapping, which will cause the decrease of the compression quality because less spectrum information in range is used to generate the final image. To solve this problem, data size

can be expanded by performing the full traditional Stolt mapping, which will increase the computational load and the required memory size. Figure 5.11(b) is the resulting spectrum of the proposed Stolt mapping, which occupies the whole time domain. The range FFT of the spectrum in Figure 5.11(b) will maintain the same range resolution as the spectrum before Stolt mapping.

The focus result using the spectrum of Figure 5.11(a) (traditional RMA) is shown in Figure 5.12. A decrease in the image quality can be observed especially from the contour plot.

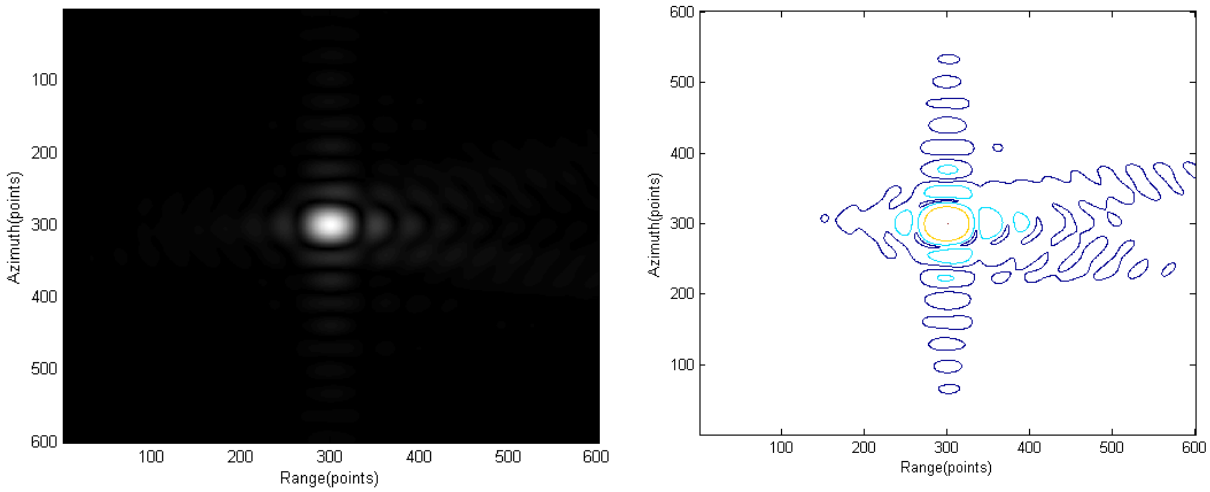

(a) (b)

Figure 5.12 Imaging results using the spectrum of Figure 5.11(a). (a) Amplitude plot. (b) Contour plot.

5.4.2 Modified RMA

This section illustrates the effectiveness of the proposed RMA in FMCW monostatic SAR signal processing.

5.4.2.1 Simulation

One point target that is not at the range centre of the imaging scene is simulated in this section. The simulation parameters are shown in Table 5.4.

Table 5.4 Simulation parameters

Parameter	Value	Unit
Centre frequency	400	MHz
PRF	200	Hz
Signal bandwidth	7.5	MHz
Scene centre	2560	m
SAR speed	50	m/s
Antenna beamwidth	42.97	Degree
Azimuth data length	8192	samples
Range data length	256	Samples
Target range	2000	m

Figure 5.13 shows the parallel shift ($f_0\left(D\left(f_\eta, v\right)-1\right)/k$) of the variable in the traditional Stolt mapping, which corresponds to the first term of (5.21).

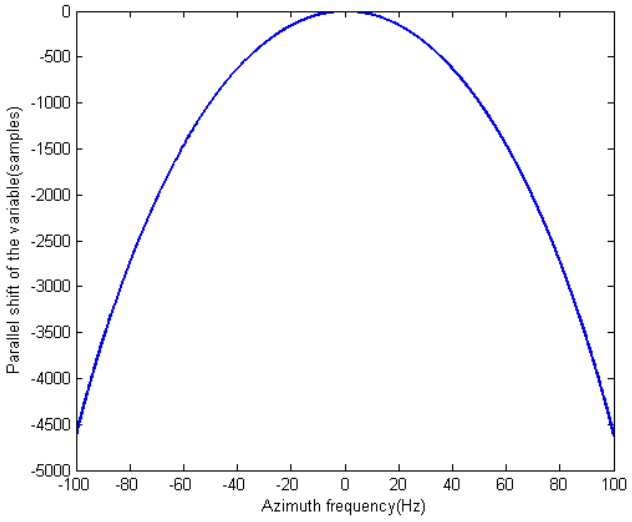

Figure 5.13 Parallel shift of the variable in traditional Stolt mapping

As shown by Figure 5.13, at both edges of the azimuth aperture, the parallel shift caused by the first term of (5.21) is more than 4500 samples, which means the length of the range spectrum should be greatly expanded to store the result of the traditional Stolt mapping. This corresponds to a significant expansion in the size of the result spectrum because the length of the original spectrum before the traditional Stolt mapping is only 256 samples in range. The modified Stolt mapping avoids this parallel shift, which reduces the required memory size for performing the traditional Stolt mapping.

Figure 5.14 shows the $D\left(f_\eta, v\right)$ defined in (5.18). At the edge of the azimuth aperture, $D\left(0, v\right)$ is 0.66 in this simulation. This means the variable change in (5.22) will still expand the time variable to 1/0.66=1.5 times of its original length. This expansion is not necessary and can be avoided if we limit the new variable in the range shown by (5.23). As a result, the proposed Stolt mapping does not expand the original spectrum length and will still maintain the same range resolution as the original spectrum.

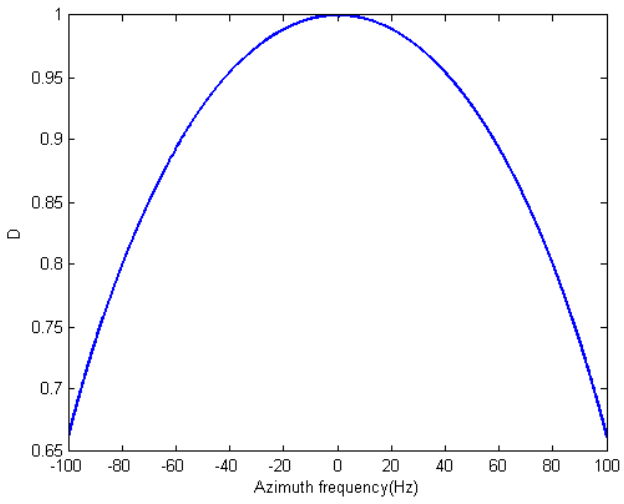

Figure 5.14 $D\left(f_\eta, v\right)$ defined in (5.18)

Figure 5.15 shows the spectrums before Stolt mapping and after Stolt mapping using the simulation parameters shown in Table 5.4. The Matlab used to generate the raw SAR data in this simulation is shown in Appendix C.

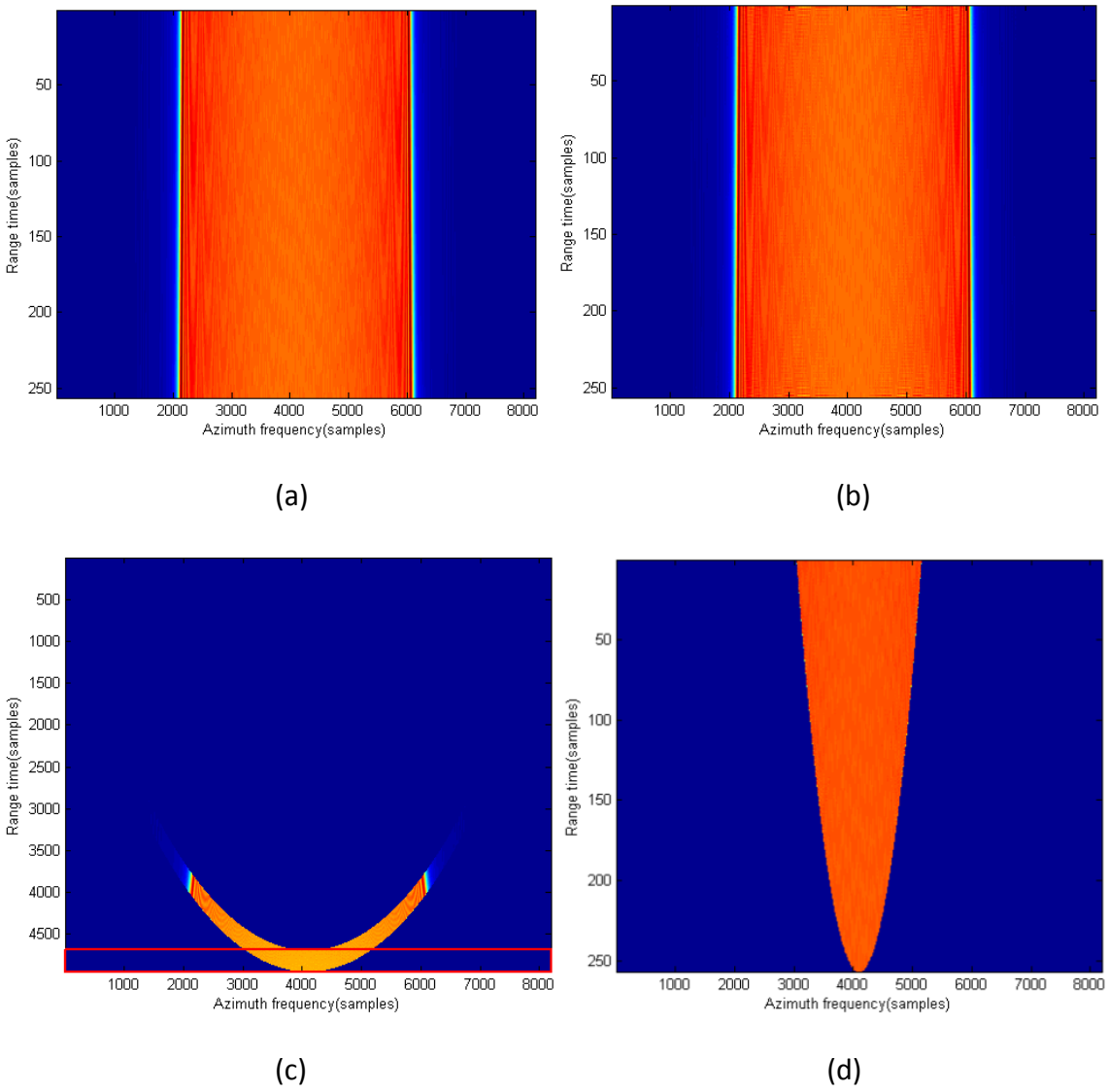

Figure 5.15 Original spectrum and the result spectrums after Stolt mapping. (a) Original spectrum. (b) Result spectrum of the proposed Stolt mapping. (c) Result spectrum of the full traditional Stolt mapping. (d) Spectrum marked by the rectangular in (c).

Figure 5.15(a) is the original spectrum which is 256 samples x 8192 samples. Figure 5.15(b) is the result of the proposed Stolt mapping, which has the same size as the origi-

nal spectrum. Figure 5.15(c) is the result spectrum after the full traditional Stolt mapping, which is about 5000 samples x 8192 samples. Because of the parallel shift and the expansion of the time variable in the traditional Stolt mapping, the size of the result spectrum has been significantly increased (almost 20 times larger than the original spectrum before Stolt mapping). This will increase the memory size required to store the spectrum after full traditional Stolt mapping, and will also increase the computational load in the following processing steps (such as longer FFT is required).

Figure 5.15(d) is the spectrum cut from the bottom 256 range samples (area marked by the rectangular in Figure 5.15 (c)) of the Figure 5.15(c), which has the same size as Figure 5.15(a) (256 samples x 8192 samples).

If the spectrums in Figure 5.15(b) and Figure 5.15(d) are used to generate the final image, Figure 5.16 is generated.

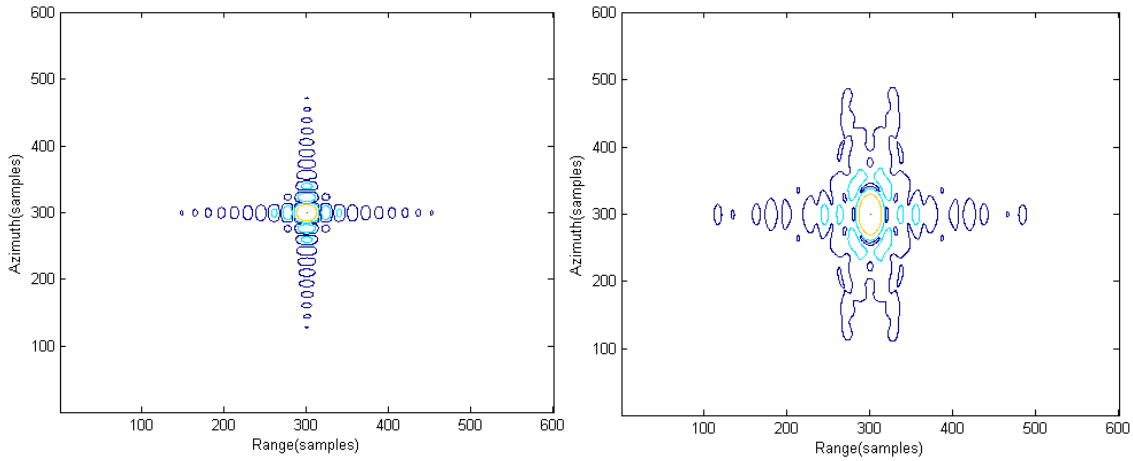

(a) (b)

Figure 5.16 Imaging result. (a) Generated image using the spectrum in Figure 5.15(b). (b) Generated image using the spectrum in Figure 5.15(d).

As can be seen from Figure 5.16, the proposed method has a better focusing quality than the traditional RMA if the same size of spectrum is used (note that the size of the spectrum that generated Figure 5.16 (a) and (b) is the same).

Figure 5.17 shows the comparison for the range slice and azimuth slice of the compressed target when using the modified RMA and the traditional RMA. The solid lines are the range and azimuth slices of the target image from Figure 5.16(a), while the dashed lines are that from Figure 5.16(b). For the solid lines in Figure 5.17(a) and (b), the 3 dB width of the mainlobes are all 15 samples, meaning the range and azimuth resolutions are the same. The mainlobe of the dashed line in Figure 5.17(b) is significantly wider than that of the solid line because the azimuth bandwidth is greatly decreased in the traditional RMA if using the cut spectrum (after Stolt mapping) that has the same size as the original one.

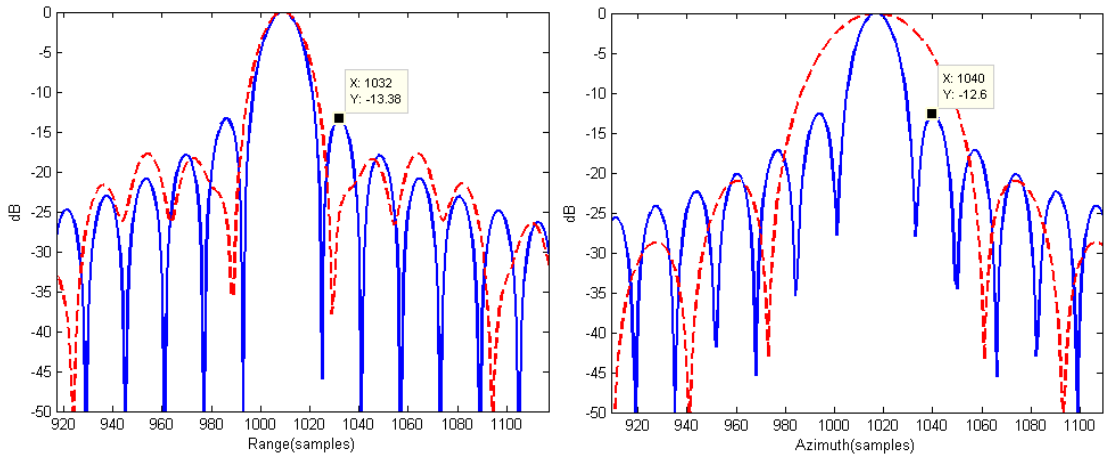

(a) (b)

Figure 5.17 Comparison of the range and azimuth slices of the compressed target. (a) Range slices. (b) Azimuth slices.

Another simulation is conducted using the parameters shown in Table 5.5. In this simulation, two targets that are very close to each other are simulated. The two targets are

at the same azimuth position, and are separated by 40 m (two range resolution cell) in range. The proposed RMA is used in this simulation to process the simulated raw data. The range FT result of the spectrum after the proposed Stolt mapping is shown in Figure 5.18(a) and the focusing result is shown in Figure 5.18(b).

Table 5.5 Simulation parameters

Parameter	Value	Unit
Centre frequency	400	MHz
PRF	200	Hz
Signal bandwidth	7.5	MHz
Scene centre	2560	m
SAR speed	50	m/s
Antenna beamwidth	42.97	Degree
Azimuth data length	8192	samples
Range data length	256	samples
Target1 range	2000	m
Target2 range	2040	m

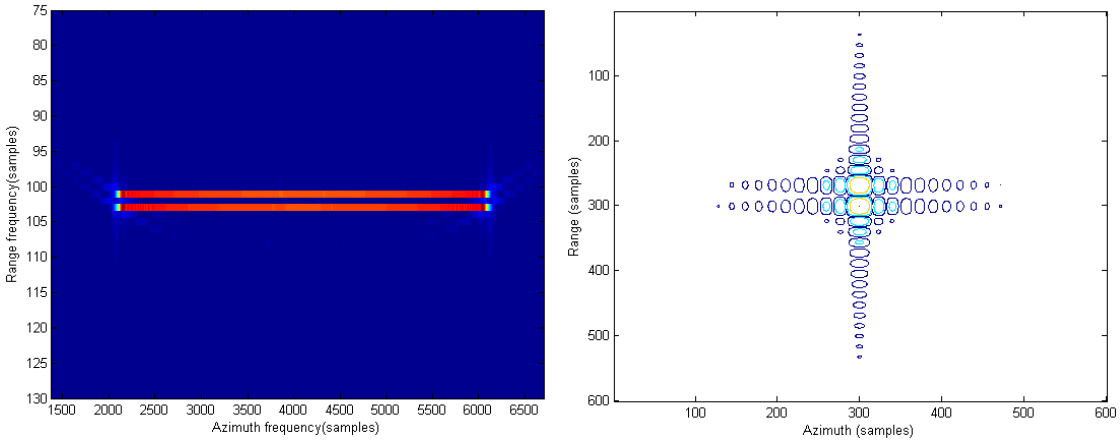

Figure 5.18 Results of using the proposed RMA. (a) Range FT result of the spectrum after the proposed Stolt mapping. (b) Targets images.

As can be seen from Figure 5.18(a), the RCM of the two targets has been totally corrected. In Section 2.1.1, it has been demonstrated that the 3 dB mainlobe width of the sinc function in the spectrum of the IF signal (after dechirp-on-receive) is determined by the

time duration of the signal. Since in the proposed Stolt mapping, the time duration of the new variable is not changed (see (5.23)), the 3 dB mainlobe width of the sinc function after the range FFT of the new variable will not change. Therefore, the targets azimuth trajectories are two straight lines that only occupy one range resolution cell at all azimuth frequencies. Figure 5.18(b) is the image result using the proposed RMA and shows that the two targets are well focused.

5.4.2.2 Real data

The real data collected by the customized FMCW SAR introduced in Chapter 3 is used in this section to verify the proposed RMA. The parameters of the SAR are shown in Table 5.6.

Table 5.6 FMCW SAR parameters

Parameter	Value	Unit
Bandwidth	150	MHz
Carrier frequency	5590	MHz
PRF	250	Hz
SAR speed	60	km/h

The images obtained by the traditional RMA and the modified RMA are shown in Figure 5.19. Four orders of interpolation are used to perform the Stolt mapping. No window is applied in both the range direction and the azimuth direction FFT for better comparison of the focusing quality because noise is not eliminated by windowing and will be more obvious in the final images. The same size of spectrum after Stolt mapping are used to generate Figure 5.19(a) and (b) as has been shown in the simulation in Figure 5.15(b) and (d).

Figure 5.19(a) presents the image obtained using the traditional RMA. By comparing the two areas marked by the boxes in Figure 5.19(a) with the same areas in Figure 5.19(b), it can be observed that a higher noise level exists in Figure 5.19(a).

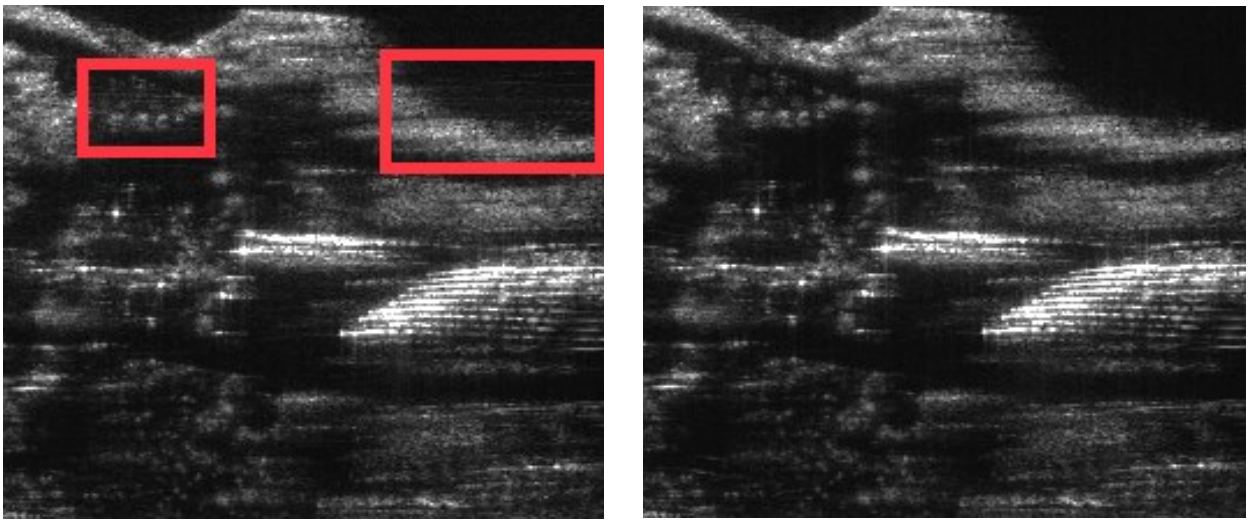

(a) (b)

Figure 5.19 Images generated by different RMAs. (a) Traditional RMA. (b) Proposed RMA.

Another real data result is shown in Figure 5.20. The procedure to generate the two images in Figure 5.20 is the same as that used to generate Figure 5.19. By comparing the area marked by the box in Figure 5.20(a) with the same area in Figure 5.20 (b), it can be observed that the image processed by the traditional RMA has higher background noise than the image generated by the proposed RMA.

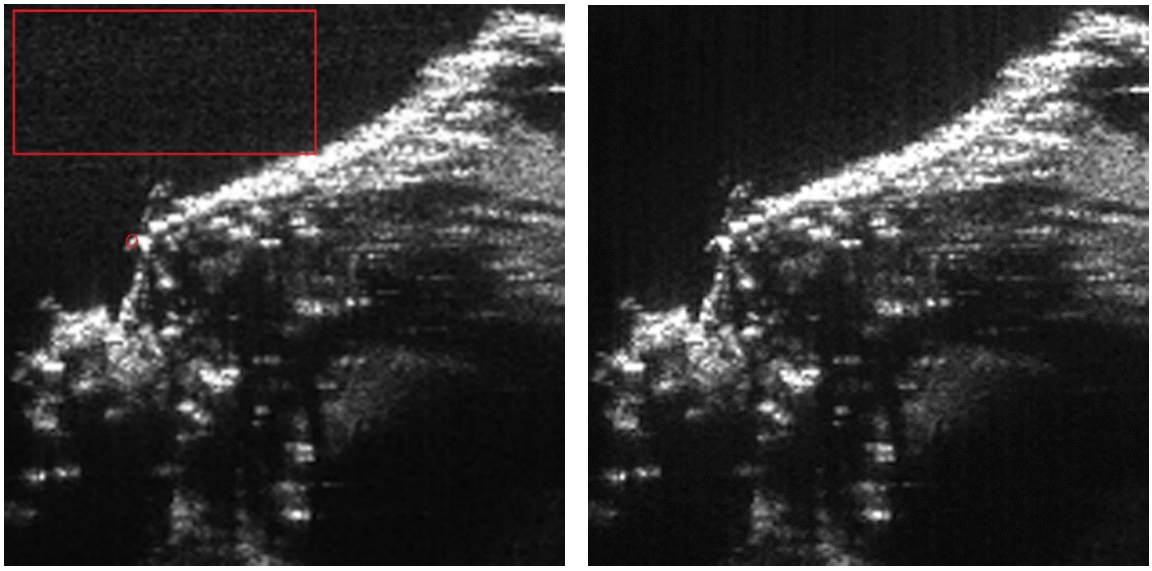

(a) (b)

Figure 5.20 Real data processed by different RMAs. (a) Traditional RMA. (b) Proposed RMA.

The range slice of the isolated strong point target marked by the small red circle in Figure 5.20(a) is shown in Figure 5.21.

In Figure 5.21, the solid line is the range slice of the marked point in Figure 5.20(a) while the dashed line is that of the same point in Figure 5.20(b). An improvement in the range focusing quality (the dashed line has narrower mainlobe) of the proposed RMA than the traditional RMA can be observed.

The improvements shown in Figure 5.19, Figure 5.20 and Figure 5.21 are slight because the SAR parameters used in the ground test are normal. The truncated spectrum after the traditional Stolt mapping in this case is not skewed as much as shown in Figure 5.15(d). The antenna beamwidth used in simulation to generate Figure 5.15(d) is chosen to be wider than normal in order to better show the improvements of the proposed method.

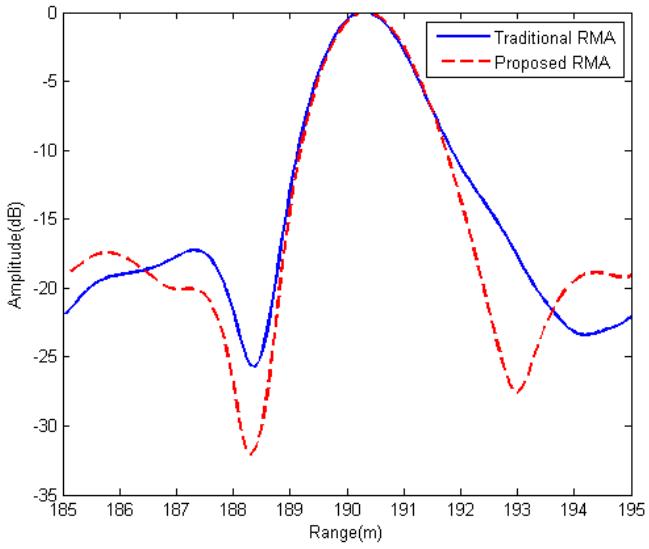

Figure 5.21 Comparison of the range profiles of an isolated strong point target marked by the red circle in Figure 5.20(a).

5.5 Summary

This chapter corresponds to Contributions 4 and 5 in Section 1.3: The bistatic configuration overcomes the limitation to the transmission power in FMCW SAR. A two dimensional spectral model for bistatic FMCW SAR signal processing has been proposed based on the Fresnel approximation. The advantage of the spectral model is that it is very similar to the monostatic FMCW SAR spectrum and thus the existing FMCW SAR imaging algorithms for monostatic configuration can be used to process the bistatic FMCW SAR image. The given spectral model is accurate under long range and narrow beamwidth SAR imaging.

A modified RMA is then proposed and used to process the bistatic FMCW SAR signal based on the proposed spectral model. The modified RMA takes advantage of the special characteristics of the IF signal in dechirp-on-receive FMCW radar systems to decreases the computational load and the memory required during image generation. The

modified RMA now have almost the same computational speed as compared to the RDA if the same orders of interpolation are used. A better focusing quality is also obtained in the proposed RMA than in the traditional RMA when using the same size of the spectrum after Stolt mapping. The modified RMA can be used in the monostatic FMCW SAR signal processing as well. Both simulation and real data verified the effectiveness of the proposed algorithm.

CHAPTER 6. CONCLUSIONS

To recapitulate, the purpose of this thesis is to improve SAR signal processing capabilities, with an application focus on small mobile platform deployment, to complement advances in SAR hardware development. The contributions and the technical and theoretical challenges I have overcome are presented in Section 6.1. A list of my publications and conference presentations is included in Section 6.2 and the areas for future work are discussed in Section 6.3.

6.1 Contributions

The contributions as outlined in Section 1.3 and documented in Chapters 3 to 5 are summarized here for the Reader's convenience:

1. A high PRF, highly coherent, and wideband prototype FMCW SAR system designed completely in-house.
2. A mathematical model to express the spectrum of the IF signal by one equation in a triangularly modulated linear frequency modulated FMCW SAR system.
3. An MTI method that can detect both the fast and very slow moving targets by using FMCW SAR data.
4. A bistatic-to-monostatic equivalent spectral model that allows the monostatic FMCW SAR signal processing algorithms to be used in bistatic FMCW SAR signal processing without significant modification.
5. A versatile and efficient modified range migration algorithm for (real time) FMCW SAR signal processing.

The technical and theoretical challenges I have overcome were:

(a) The design and build of the FMCW SAR: The radar system was designed and built independently by the author, while the antennas were from the BYU μSAR system. Several FMCW SAR systems were studied during the design of the system. A number of technical reports and component specifications have been reviewed to select the appropriate elements that fit system requirements. Experimental results obtained during the development of the system are described.

(b) Analyzing triangularly modulated linear frequency modulated signal as one signal and indicating both fast and slow moving targets: The model to analyze TM-LFM signal as one signal and the MTI method were presented in Chapter 4. The employment of the triangularly modulated signal in FMCW SAR is a requirement from the hardware rather than from signal processing in a traditional sense. However, as shown by the derivation and the real data results, by exploiting the high coherency of the SAR system the TM signal can be used as one integral signal to accurately indicate moving targets with radial velocities less than 1 m/s. The possibility of improving the range resolution without increasing the modulated signal bandwidth has also been demonstrated by using certain stationary ground reflectors. However, the universality of this hypothesis still needs to be verified using a redesigned radar system.

(c) Analyzing bistatic FMCW SAR signal: The model to analyze bistatic FMCW SAR signal and an improved RMA for FMCW SAR signal processing were introduced in Chapter 5. With proper synchronization between the transmitter and the receiver, the bistatic configuration will improve the FMCW SAR capability.

(d) Improving the range migration algorithm: By exploiting the characteristics of the IF signal in FMCW SAR system, an efficient modified RMA which can be used for real time signal processing was proposed in Chapter 5.

6.2 Publications and Conferences

The peer-reviewed journal papers are:

1. Yake Li and Siu O'Young, "A Method of Doubling Range Resolution Without Increasing Bandwidth in FMCW Radar," *Electronic Letters*, vol. 51, no. 12, 2015.
2. Yake Li and Siu O'Young, "Focusing Bistatic FMCW SAR Signal by Range Migration Algorithm Based on Fresnel Approximation," *Sensors,* vol. 12, no. 12, 2015.
3. Yake Li and Siu O'Young, "Detection of Moving Targets with Triangularly Modulated FMCW Radar," *IEEE Sensors Journal.* Under review.
4. Yake Li and Siu O'Young, "A Modified Range Migration Algorithm for FMCW SAR signal processing", *IET Radar Sonar and Navigation.* Under revision.

The conference presentations were:

1. Yake Li, Siu O'Young and Robert MacIsaac, "A K-Band FMCW Radar System: Introduction and First Experiment," *Newfoundland Electrical and Computer Engineering Conference*, Newfoundland, Canada, Nov. 2013.
2. Yake Li and Siu O'Young, "Removal of Synthetic Aperture Effect in Stepped Frequency Radar Altimeter," *Progress In Electromagnetics Research Symposium*, Guangzhou, China, Aug. 2014.

3. Yake Li, Siu O'Young and Robert MacIsaac, "Introduction to a C-band FMCW Radar System," *Newfoundland Electrical and Computer Engineering Conference*, Newfoundland, Canada, Nov. 2014.

6.3 Future Work

1. Redesign and rebuild the customized FMCW SAR. The FMCW SAR can still be improved in size, SNR and detection range. First, by compacting and combining all the elements on the PCBs, the separated PCBs can be combined. Second, most of the off-the-shelf microwave components (mainly in the receiving channel) in the current radar system can be replaced by equivalent circuits composed of surface-mount components. This will further miniaturize the radar system and increase the efficiency of the microwave power propagation (decrease the losses between components) and hence the SNR. As a result, the FMCW SAR will be smaller, more cost effective, and have improved imaging range performance.
2. The hypothesis of increasing range resolution without increasing signal bandwidth should be further investigated. A radar that is specially used for this purpose should be designed and built. The new radar system should have a very high centre frequency and carefully designed PRF. Moreover, stable microwave components should be used.
3. The proposed MTI method is only capable of calculating the radial speed when the velocity ambiguity index is zero. Further research could be conducted to develop a method to calculate the velocity accurately when the ambiguity index is not zero.

4. A bistatic FMCW SAR can be designed and built. Because the pulse length of the FMCW radar is longer than that for pulse radars, synchronization, which is the main problem for pulse bistatic SAR, could be easier to achieve in FMCW bistatic SAR. As the result, the operation range of the FMCW SAR could be significantly increased.
5. The research on the algorithms for FMCW bistatic SAR signal processing is still in the initial stage. Significant effort could be put into the development of the signal processing algorithms which will push forward applications of FMCW bistatic SAR.

REFERENCES

[1] A. W. Love, "In Memory of Carl A. Wiley," *IEEE Antennas and Propagation Society Newsletter*, vol. 27, no. 3, pp. 17–18, June 1985.

[2] C. W. Sherwin, J. P. Ruina and R. D. Rawcliffe, "Some Early Developments in Synthetic Aperture Radar Systems," *IRE Trans. on Military Electronics*, vol. MIL-6, no. 2, pp. 111-115, April 1962.

[3] A. Moreira, P. Prats-Iraola, M. Younis, G. Krieger, I. Hajnsek, K.P. Papathanassiou "A Tutorial on Synthetic Aperture Radar," *IEEE Geoscience and Remote Sensing Magazine,* vol. 1, no. 1, 2013.

[4] E. N. Leith, "Quasi-Holographic Techniques in the Microwave Region," *Proc. of the IEEE,* vol. 59, no. 9, Sep. 1971.

[5] I. G. Cumming and F. H. Wong, "Digital Processing of Synthetic Aperture Radar Data," Artech House, 2005.

[6] M. Cherniakov, "Bistatic Radar: Emerging Technology," NY: Wiley, 2008.

[7] G. Krieger and A. Moreira, "Potential of digital beamforming in bi-and multistatic SAR," in *Proc. IEEE International Geoscience and Remote Sensing Symposium. (IGARSS)*, 2003, pp. 527–529.

[8] M. Edrich, "Design Overview and Flight Test Results of the Miniaturised SAR Sensor MISAR," in *Proc. EuRAD*, Amsterdam, The Netherlands, Oct. 2004, pp. 205–208.

[9] E. C. Zaugg, D. L. Hudson and D.G. Long, "The BYU μSAR: A Small, Student-built SAR for UAV Operation," in *Proc. IGARSS*, Denver, USA, Jul. 2006, pp. 411–414.

[10] A. Meta, J. Wit and P. Hoogeboom, "Development of a High Resolution Airborne Millimeter Wave FM-CW SAR," in *Proc. EuRAD*, Amsterdam, The Netherlands, 2004, pp. 209-212.

[11] M. Edrich, "Ultra-lightweight Synthetic Aperture Radar Based on a 35 GHz FMCW Sensor Concept and Online Raw Data Transmission," *IEE Proc.Radar Sonar Navigation*, vol. 153, no. 2, April 2006.

[12] E. Zaugg and D. Long, "Theory and Application of Motion Compensation for LFMCW SAR," *IEEE Trans. on Geoscience and Remote Sensing*, vol. 46, no. 10, pp. 2990-2998, Oct. 2008.

[13] M. Edwards, D. Madsen, C. Stringham, A. Margulis, B. Wicks, and D. Long, "MicroASAR: A Small, Robust LFM-CW SAR for Operation on UAVs and Small Aircraft," in *Proc. IGASS*, 2008, pp. V-514-V-517.

[14] S. Stanko, W. Johannes, R. Sommer, A. Wahlen, J. Wilcke, H. Essen, A. Tessmann, I. Kallfass, "SAR with MIRANDA - Millimeterwave Radar Using Analog and New Digital Approach," in *Proc. EuRAD,* 2011, pp. 214-217.

[15] H. Essen, S. Stanko, ect., "Millimetre Wave SAR for UAV Operation," in *Proc. APMC,* 2011, pp.963-966.

[16] W. van Rossum, M. Otten, P. van Dorp, "Multichannel FMCW SAR," in *Proc. Eu-SAR*, Nuremberg, Germany, Apr. 2012, pp. 279-282.

[17] H. Rohling, C. Moller, "Radar Waveform for Automotive Radar Systems and Applications," in *Proc. RADAR* , Rome, Italy, May 2008, pp. 1-4.

[18] S. Kim, I. Paek, M. Ka, "Simulation and Test Results of Triangular Fast Ramp FMCW Waveform," in *Proc. RADAR,* Ottawa, Canada, Apr. 2013, pp. 1-4.

[19] H. Rohling, M. Meinecke, "Waveform Design Principles for Automotive Radar Systems," in *Proc. Radar,* 2001, pp. 1-4.

[20] J. Zhang, E. Gill and J. Walsh, "High Frequency (HF) Radar Cross Sections of the Ocean Surface Incorporating a Continuous Wave Frequency Modulated Source," *OCEANS*, Quebec, Canada, 2008, pp. 1-5.

[21] A. G. Stove, "Linear FMCW radar techniques," *Proc. Inst. Electr. Eng. F—Radar Signal Processing*, vol. 139, no. 5, pp. 343–350, Oct. 1992.

[22] E. C. Zaugg, "Generalized Image Formation for Pulsed and LFM-CW Synthetic Aperture Radar," Ph.D. thesis, Department of Electronics and Computer Engineering, BYU, Provo, UT, 2010.

[23] R. K. Raney, H. Runge, R. Bamler, I.G. Cumming, and F.H. Wong, "Precision SAR Processing Using Chirp Scaling," *IEEE Trans. on Geoscience and Remote Sensing*, vol. 32, no. 4, pp. 786-799, 1994.

[24] A. Moreira and Y. Huang, "Airborne SAR Processing of Highly Squinted Data Using a Chirp Scaling Approach with Integrated Motion Compensation," *IEEE Trans. on Geoscience and Remote Sensing*, vol. 32, no. 5, pp.1029-1040, Sep. 1994.

[25] A. Moreira, J. Mittermayer, and R. Scheiber, "Extended chirp scaling algorithm for air- and spaceborne SAR data processing in stripmap and scanSAR imaging modes," *IEEE Trans. on Geoscience and Remote Sensing*, vol. 34, no. 5, pp. 1123–1136, Sep. 1996.

[26] G. Davidson, I. Cumming, and M. Ito, "A Chirp Scaling Approach for Processing Squint Mode SAR Data," *IEEE Trans. on Aerospace and Electronic Systems*, vol. 32, no. 1, pp. 121–133, 1996.

[27] E. C. Zaugg, D. Long, "Generalized Frequency Scaling and Backprojection for LFM-CW SAR Processing," *IEEE Trans. on Geoscience and Remote Sensing,* vol. 53, no. 7, pp. 3600-3614, July, 2015.

[28] E. Zaugg and D. Long, "Generalized Frequency-Domain SAR Processing," *IEEE Trans. on Geoscience and Remote Sensing,* vol. 47, no. 11, pp. 3761-3773, 2009.

[29] J. Mittermayer, A. Moreira and O. Loffeld, "Spotlight SAR Data Processing Using the Frequency Scaling Algorithm," *IEEE Trans. on Geoscience and Remote Sensing,* vol. 37, no. 5, pp. 2198-2214, 1993.

[30] D. R. Wehner, "High-Resolution Radar (Second Edition)," Boston: Artech House, 1994.

[31] J.H.G. Ender and A.R. Brenner, "PAMIR - a wideband phased array SAR/MTI system," *IEE Proc.-Radar Sonar Navigation,* vol. 150, no. 3, June 2003.

[32] C. A. Balanis, "Antenna theory: analysis and design (second edition)," NY: Wiley, 1997.

[33] W. G. Carrara, R. S. Goodman and R. M. Majewski, "Spotlight Synthetic Aperture Radar," Artech House, 1995.

[34] A. Meta., P. Hoogeboom, and L. P. Ligthart, "Signal Processing for FMCW SAR," *IEEE Trans. on Geoscience and Remote Sensing*, vol. 45, no. 11, pp. 3519-3532, Nov. 2007.

[35] A. Meta and P. Hoogeboom, "Signal Processing Algorithms for FMCW Moving Target Indicator Synthetic Aperture Radar," in *Proc. IGASS'05*, Seoul, Korea, July 2005, pp. 316-319.

[36] J. J. M. de Wit, A. Meta, and P. Hoogeboom, "Modified Range-Doppler Processing for FM-CW Synthetic Aperture Radar," *IEEE Geoscience and Remote Sensing Letters*, vol. 3, no. 1, pp. 83-87, Jan. 2006.

[37] C. Wu, "A Digital System to Produce Imagery from SAR Data," in *AIAA Conference: System Design Driven by Sensors*, Oct. 1976.

[38] C. Wu, K. Y. Liu and M. J. Jin, "A Modeling and Correlation Algorithm for Spaceborne SAR Signals," *IEEE Tans. on Aerospace and Electronic Systems*, vol. AES-18, no. 5, pp. 563-574, 1982.

[39] I. G. Cumming and J. R. Benett, "Digital Processing of SEASET SAR DATA," in *IEEE 1979 International Conference on Acoustics, Speech and Signal Processing*, Washington, D. C., 1979.

[40] C. Cafforio, C. Prati and F. Rocca, "SAR data focusing using seismic migration techniques," *IEEE Trans. on Aerospace and Electronic Systems*, vol. 27, no. 2, pp. 194-207, 1991.

[41] F. Rocca, C. Prati, and Monti-Guarnieri, "A New algorithms for processing of SAR data," ESA Contract Report, ESRIN contract 7998/88/F/FL(SC), 1989.

[42] C. Cafforio, C. Prati and F. Rocca, "Full resolution focusing of Seasat SAR images in the frequency-wave number domain," *International Journal of Remote Sensing,* vol. 12, no. 3, pp. 491-510, 1991.

[43] S. O'Young and P. Hubbard, "RAVEN: A Maritime Surveillance Project Using Small UAV", *IEEE Conference on Emerging Technologies and Factory Automation*, 2007, pp. 904-907.

[44] RS3400X datasheet, http://siversima.com/wp-content/uploads/RS3400X00-Data-Sheet.pdf

[45] RS3400 evaluation kit, http://siversima.com/wp-content/uploads/FMCWKITK.pdf

[46] SRR series datasheet, http://ducommun.com/pdf/SRR-Series.pdf

[47] J. Yang, C. Liu, Y. Wang, "Nonlinearity Correction of FMCW SAR Based on Homomorphic Deconvolution," *IEEE Geoscience and Remote Sensing letters,* vol. 10, no. 5, pp. 991-995, 2013.

[48] "Fundamentals of Direct Digital Synthesis (DDS)," tutorial from Analog Devices, MT-085.

[49] "A Technical Tutorial on Digital Signal Synthesis," tutorial from Analog Devices.

[50] Y. Li, C. Liu, Y. Wang and Q. Wang, "A Robust Motion Error Estimation Method Based on Raw SAR Data," *IEEE Trans. on Geoscience and Remote Sensing,* vol. 50, no. 7, pp. 2780-2790, 2012.

[51] O. Loffeld, H. Nies, V. Peters et al., "Models and Useful Relations for Bistatic SAR Processing," *IEEE Trans. on Geoscience and Remote Sensing*, vol. 42, no. 10, pp. 2031-2038, Oct. 2004.

[52] R. Bamler and E. Boerner, "On the Use of Numerically Computed Transfer Functions for Processing of Data from Bistatic SARs and High Squint Orbital SARs," *IGARSS,* 2005, pp. 1051-1055.

[53] R. Bamler, R. Meyer and L. Liebhart, "No Math: Bistatic SAR Processing Using Numerically Computed Transfer Functions," *IGARSS,* 2006, pp. 1844-1847.

[54] Xupu Geng, Honghui Yan and Yanfei Wang, "A two-dimensional spectrum model for general bistatic SAR," *IEEE Trans. on Geoscience and Remote Sensing*, vol.46, no. 8, pp. 2216-2223, Aug. 2008.

[55] Y. L. Neo, F. Wong and I. G. Cumming, "A Two-dimensional Spectrum for Bistatic SAR Processing Using Series Reversion," *IEEE Geoscience and Remote Sensing letters*, vol. 4, no. 1, pp. 93-96, Jan. 2007.

[56] B. D. Rigling and R. L. Moses, "Polar Format Algorithm for Bistatic SAR", *IEEE Trans. on Aerospace and Electronic Systems*, vol. 40, no. 4, pp. 1147-1159, Oct. 2004.

[57] M. Soumekh, "Bistatic Synthetic Aperture Radar Inversion with Application in Dynamic Object Imaging," *IEEE Trans. on Signal Processing*, vol. 39, no. 9, pp. 2044-2055, Sep. 1991.

[58] I. Walterscheid, J. H. G. Ender, A. R. Brenner et al., "Bistatic SAR Processing Using an Omega-k Type Algorithm", *in Proc. IGARSS,* 2005, vol. 2, pp. 1064-1067.

[59] V. Giroux, H. Cantalloube and F. Daout, "An omega-k algorithm for SAR bistatic systems", *in proc. IGARSS,* 2005, vol. 2, pp. 1060-1063.

[60] Y. L. Neo, F. H. Wong and I. G. Cumming, "Processing of Azimuth-invariant Bistatic SAR Data Using the Range Doppler Algorithm", *IEEE Trans. on Geoscience and Remote Sensing*, vol. 46, no. 1, pp. 14-21, Jan. 2008.

[61] F. H. Wong, I. G. Cumming and Y. L. Neo, "Focusing Bistatic SAR Data Using Nonlinear Chirp Scaling Algorithm", *IEEE Trans. on Geoscience and Remote Sensing*, vol. 46, no. 9, pp. 2493-2505, Sept. 2008.

[62] Y. Liu, R. Wang, Y. Deng, O. Loffeld, "Bistatic FMCW SAR Signal Model and Imaging Approach," *IEEE Trans. on Aerospace and Electronic Systems,* vol. 49, no. 3, 2017-2028, 2013.

[63] Y. Liu, Y. Deng, R. Wang, O. Loffeld, X. Wang, "Model and Signal Processing of Bistatic Frequency Modulated Continuous Wave Synthetic Aperture Radar," *IET Radar Sonar Navigation,* vol. 6, pp. 472-482, 2013.

[64] A. Reigber, E. Alivizatos, A. Potsis, A. Moreira, "Extended Wavenumber-domain Synthetic Aperture Radar Focusing with Integrated Motion Compensation," *IET Radar Sonar Navigation*, vol. 153, pp. 301-310, 2006.

[65] L. Zhang, J. Sheng, M. Xing, Z. Qiao, T. Xiong, Z. Bao, "Wavenumber-Domain Autofocusing for Highly Squinted UAV SAR Imagery," *IEEE Sensors Journal*, vol. 12, no. 5, pp. 1574-1588, 2012.

[66] G. Xu, M. Xing, L. Zhang, Z. Bao, "Robust Autofocusing Approach for Highly Squinted SAR Imagery Using the Extended Wavenumber Algorithm," *IEEE Trans. on Geoscience and Remote Sensing*, vol. 51, no. 10, pp. 5031-5046, 2013.

[67] R. Wang, O. Loffeld, H. Nies, S. Knedlik, M. Hagelen, H. Essen, "Focus FMCW SAR Data Using the Wavenumber Domain Algorithm," *IEEE Trans. on Geoscience and Remote Sensing,* vol. 48, pp. 2109-2118, 2010.

[68] Y. Liu, Y. Deng, R. Wang, "Focus Squint FMCW SAR Data Using Inverse Chirp-Z Transform Based on an Analytical Point Target Reference Spectrum," *IEEE Geoscience and Remote Sensing letters*, vol. 9, no. 5, 2012.

[69] M. Vandewal, R. Speck, Helmut, "Efficient and Precise Processing for Squinted Spotlight SAR through a Modified Stolt Mapping," *EURASIP Journal on Advances* in Signal Processing, pp. 1-7, 2007.

[70] http://www.imsar.com/pages/products.php?name=nanosar. NANO SAR specifications.

[71] H. Chen, etc., "New Approach for Synthesizing the Range Profile of Moving targets via stepped-Frequency Waveforms," *IEEE Geoscience and Remote Sensing Letters*, vol. 3, no. 3, Jul. 2006.

[72] R. T. Lord and M. R. Inggs, "High Resolution SAR Processing Using Stepped-Frequencies," in *Proc. IGARSS*, Aug. 1997, pp. 490-492.

[73] R. T. Lord and M. R. Inggs, "High Range Resolution Radar using Narrowband Linear Chirps offset in Frequency," in Proc. *COMSIG*, Sept. 1997, pp. 9-12.

[74] G. S. Gill, "Step Frequency Waveform Design and Processing for detection of Moving Targets in Clutter," in *Proc. Radar Conference*, 1995, pp. 573-578.

[75] Y. Liu, etc., "Velocity Estimation and Range Shift Compensation for High Range Resolution Profiling in Stepped-Frequency Radar," *IEEE Geoscience and Remote Sensing Letters*, vol. 7, no. 4, Oct. 2010.

[76] J. L. Auterman, "Phase stability requirements for a bistatic SAR", in *Proc. IEEE National Radar Conference*, Altanta, GA, March 1984, pp. 48-52.

[77] D. M. Pozar, "Microwave Engineering (Fourth Edition)," NY: Wiley, USA, 2011.

[78] M. Skolnik, "Radar Handbook (Second Edition)," NY: McGraw-Hill, USA, 1990.

[79] R. E. Collin, "Foundations for Microwave Engineering (Second Edition)," NY: Wiley, USA, 2000.

[80] W. D. Brown, and D. C. Ghiglia, "Some Methods for Reducing Propagation-Induced Phase emrs in Coherent Imaging Systems," *Journal of the Optical Society of America*, vol. 5, pp. 924-941, 1988.

[81] A. Reigber and K. Papathanassiou, "Correction of Residual Motion Errors in Airborne Repeat-Pass Interferometry," *in Proc. IGARSS*, vol. 7, 2001.

[82] P. H. Eichel, D. C. Ghiglia, and C. V. Jakowatz, "Speckle processing method for synthetic-aperture-radar phase correction," *Optics Letters*, vol. 14, no. 1, pp. 1-3, Jan. 1989.

[83] Y. Li and S. O'Young, "A Method of Doubling Range Resolution Without Increasing Bandwidth in FMCW Radar," *IET Electronic Letters*, vol. 51, no. 12, 2015.

[84] Y. Li, Y. Wang and C. Liu, "Detect and Focus the Moving Target by Its Range Walk in Time Domain," *in Proc. on International conference on wireless communication and signal processing*, 2011.

[85] Y. Li, C. Liu and Y. Wang, "A Range-Dependent Autofocus Algorithm Based on Tikhonov Regularization Method," *International Journal of Remote Sensing,* vol. 33, no. 21, 2012.

[86] K. Wang and X. Liu, "Quartic-phase algorithm for highly squinted SAR data processing," *IEEE Geoscience and Remote Sensing Letters*, vol. 4, no. 2, pp. 246–250, 2007.

[87] R. Lord and M. Inggs, "High resolution SAR processing using stepped-frequencies," i*n Proc. IEEE International Geoscience and Remote Sensing Symposium*, vol. 1, pp. 490–492, 1997.

[88] A. Wilkinson, R. Lord, and M. Inggs, "Stepped-frequency processing by reconstruction of target reflectivity spectrum," *in Proc. South African Symposium on Communications and Signal Processing*, pp. 101–104, 1998.

[89] A. Meta, P. Hoogeboom, and L. Ligthart, "Range non-linearities correction in FMCWSAR," *in Proc. IEEE International Geoscience and Remote Sensing Symposium*, pp. 403–406, 2006.

APPENDIX A. INSTANTANEOUS SLANT RANGE IN FMCW SAR

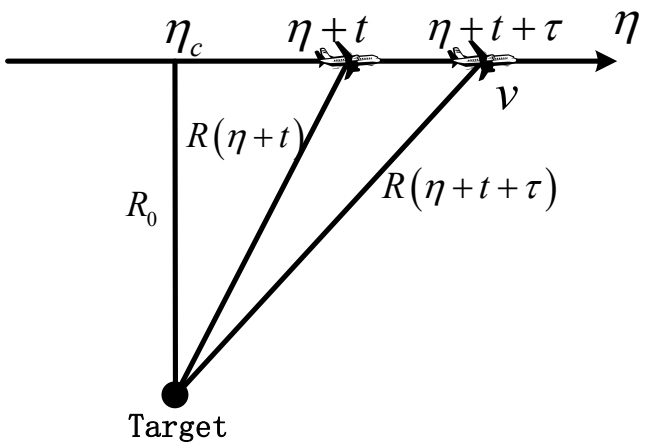

Figure A1 FMCW SAR instantaneous slant range

Figure A1 shows the geometry used to derive the instantaneous slant range. The radar transmits a signal with specific frequency at time $\eta+t$ and receives the returned echo at time $\eta+t+\tau$. Therefore, the following equation holds

$$\tau=\frac{R(\eta+t)+R(\eta+t+\tau)}{c} \tag{A.1}$$

where

$$R(\eta+t)=\sqrt{R_0^2+v^2(\eta+t-\eta_c)^2} \tag{A.2}$$

$$R(\eta+t+\tau)=\sqrt{R_0^2+v^2(\eta+t+\tau-\eta_c)^2} \tag{A.3}$$

In (A.1), move $R(\eta+t)/c$ to the left and square both sides, τ could be resolved which is

$$\tau=2\frac{c^2}{c^2-v^2}\left[\frac{R(\eta+t)}{c}+\frac{v^2}{c^2}(\eta+t-\eta_c)\right] \tag{A.4}$$

And we have $v \ll c$, hence (A.4) can be approximated as

$$\tau \approx \frac{2R(\eta + t)}{c} \tag{A.5}$$

This approximation equals to assume the aircraft stays stationary after the signal is transmitted until the returned signal is received. As the propagation time of the electro-magnetic wave is only tens of microseconds, this approximation is quite accurate. The error is only several millimeters at most in airborne case.

APPENDIX B. THE APPROXIMATION OF THE SLANT RANGE

The inner square root in (5.3) can be expressed as

$$\begin{aligned}
&\sqrt{R_{0R}{}^2 R_{0T}{}^2 + R_{0R}{}^2 v_T{}^2(\eta+t-\eta_{0T})^2 + R_{0T}{}^2 v_R{}^2(\eta+t-\eta_{0R})^2 + v_R{}^2(\eta+t-\eta_{0R})^2 v_T{}^2(\eta+t-\eta_{0T})^2} \\
&\approx \sqrt{R_{0R}{}^2 R_{0T}{}^2 + R_{0R}{}^2 v_T{}^2(\eta+t-\eta_{0T})^2 + R_{0T}{}^2 v_R{}^2(\eta+t-\eta_{0R})^2} \\
&= R_{0R} R_{0T} \sqrt{1 + \frac{v_T{}^2(\eta+t-\eta_{0T})^2}{R_{0T}^2} + \frac{v_R{}^2(\eta+t-\eta_{0R})^2}{R_{0R}^2}}
\end{aligned} \tag{B.1}$$

Let

$$\frac{v_T{}^2(\eta+t-\eta_{0T})^2}{R_{0T}^2} + \frac{v_R{}^2(\eta+t-\eta_{0R})^2}{R_{0R}^2} = \rho^2$$

Then the square root in the third row of (B.1) has the form of $\sqrt{1+\rho^2}$. Under the assumption of $R_{0R} \gg v_{0R}\left(\eta+t-\eta_{0R}\right)$ and $R_{0T} \gg v_{0T}\left(\eta+t-\eta_{0T}\right)$, we have $\rho \ll$. Therefore, we have

$$\sqrt{1+\rho^2} \approx 1 + \frac{\rho^2}{2} \tag{B.2}$$

Substitute (B.2) into (B.1), we have

$$\sqrt{1 + \frac{v_T{}^2(\eta+t-\eta_{0T})^2}{R_{0T}^2} + \frac{v_R{}^2(\eta+t-\eta_{0R})^2}{R_{0R}^2}} \approx 1 + \frac{v_T{}^2(\eta+t-\eta_{0T})^2}{2R_{0T}^2} + \frac{v_R{}^2(\eta+t-\eta_{0R})^2}{2R_{0R}^2} \tag{B.3}$$

which is the Fresnel approximation.

Then the last row of (B.1) can be expressed as

$$\begin{aligned}
&R_{0R} R_{0T} \sqrt{1 + \frac{v_T{}^2(\eta+t-\eta_{0T})^2}{R_{0T}^2} + \frac{v_R{}^2(\eta+t-\eta_{0R})^2}{R_{0R}^2}} \\
&\approx R_{0R} R_{0T} \left(1 + \frac{v_R{}^2(\eta+t-\eta_{0R})^2}{2R_{0R}{}^2} + \frac{v_T{}^2(\eta+t-\eta_{0T})^2}{2R_{0T}{}^2}\right)
\end{aligned} \tag{B.4}$$

For simplicity, we first square both sides of (5.3) so that the outer square root does not appear in the following derivation. Substituting (B.4) into the squared result of (5.3), we have

$$R^2 = {R_{0T}}^2 + {R_{0R}}^2 + {v_T}^2(\eta + t - \eta_{0T})^2 + {v_R}^2(\eta + t - \eta_{0R})^2 + 2R_{0R}R_{0T}\left(1 + \frac{{v_R}^2(\eta + t - \eta_{0R})^2}{2{R_{0R}}^2} + \frac{{v_T}^2(\eta + t - \eta_{0T})^2}{2{R_{0T}}^2}\right)$$

$$= \left(R_{0T} + R_{0R}\right)^2$$

$$+ \frac{{v_T}^2 R_{0R}R_{0T}(\eta + t - \eta_{0T})^2 + {v_T}^2{R_{0R}}^2(\eta + t - \eta_{0T})^2 + {v_R}^2 R_{0R}R_{0T}(\eta + t - \eta_{0R})^2 + {v_R}^2{R_{0T}}^2(\eta + t - \eta_{0R})^2}{R_{0R}R_{0T}}$$

$$= \left(R_{0T} + R_{0R}\right)^2 + \frac{R_{0T} + R_{0R}}{R_{0R}R_{0T}}\left[{v_R}^2 R_{0T}(\eta + t - \eta_{0R})^2 + {v_T}^2 R_{0R}(\eta + t - \eta_{0T})^2\right]$$

$$= \left(R_{0T} + R_{0R}\right)^2 + \frac{\left(R_{0T} + R_{0R}\right)\left({v_R}^2 R_{0T} + {v_T}^2 R_{0R}\right)}{R_{0R}R_{0T}}$$

$$\cdot\left[\left(\eta + t\right)^2 - 2\frac{{v_R}^2 R_{0T}\eta_{0R} + {v_T}^2 R_{0R}\eta_{0T}}{{v_R}^2 R_{0T} + {v_T}^2 R_{0R}}\left(\eta + t\right) + \frac{{v_R}^2 R_{0T}\eta_{0R} + {v_T}^2 R_{0R}\eta_{0T}}{{v_R}^2 R_{0T} + {v_T}^2 R_{0R}}\right]$$

$$= \left(R_{0T} + R_{0R}\right)^2 + \frac{\beta\left(R_{0T} + R_{0R}\right)}{R_{0R}R_{0T}}$$

$$\cdot\left[\left(\eta + t\right)^2 - 2\frac{{v_R}^2 R_{0T}\eta_{0R} + {v_T}^2 R_{0R}\eta_{0T}}{{v_R}^2 R_{0T} + {v_T}^2 R_{0R}}\left(\eta + t\right) + \frac{\left({v_R}^2 R_{0T}\eta_{0R} + {v_T}^2 R_{0R}\eta_{0T}\right)^2 + {v_T}^2{v_R}^2 R_{0T}R_{0R}\left(\eta_{0T} - \eta_{0R}\right)^2}{\left({v_R}^2 R_{0T} + {v_T}^2 R_{0R}\right)^2}\right]$$

$$= \left(R_{0T} + R_{0R}\right)^2 + \frac{\beta\left(R_{0T} + R_{0R}\right)}{R_{0R}R_{0T}}\left[\eta + t - \frac{{v_R}^2 R_{0T}\eta_{0R} + {v_T}^2 R_{0R}\eta_{0T}}{\beta}\right]^2 + \frac{R_{0T} + R_{0R}}{\beta}{v_T}^2{v_R}^2\left(\eta_{0T} - \eta_{0R}\right)^2$$

$$= 4\left\{\left(\frac{R_{0T} + R_{0R}}{2}\right)^2 + \frac{\beta\left(R_{0T} + R_{0R}\right)}{4R_{0R}R_{0T}}\left[\eta + t - \frac{{v_R}^2 R_{0T}\eta_{0R} + {v_T}^2 R_{0R}\eta_{0T}}{\beta}\right]^2 + \frac{R_{0T} + R_{0R}}{4\beta}{v_T}^2{v_R}^2\left(\eta_{0T} - \eta_{0R}\right)^2\right\}$$

where

$$\beta = R_{0R}v_T^2 + R_{0T}v_R^2$$

APPENDIX C. PROGRAM FOR FMCW SAR RAW DATA GENERATION

The following Matlab program is used to generate the raw data used in the first simulation of Section 5.4.2.1.

```
Fc=4e8;
C=3e8;
lumda=C/Fc;
Rmax=10240/2;
D=1;
V=50;
sqtangle=0/180*pi;
dopplercenf=2*V*sin(sqtangle)/lumda;
halfPRF=1.3*2*V/D/2;
tempintger=floor(dopplercenf/halfPRF);
tempintger=0;
if tempintger>1
   if mod(tempintger,2)==1
      tempintger=tempintger-1;
   end
   PRF=dopplercenf/tempintger*2;
   ambnum=tempintger/2;
else
   PRF=2*(2*V/D+1*2*V*sin(sqtangle)/lumda);
   ambnum=0/2;
end
Tr=1/PRF;
Bw=7.5e6;
Kr=Bw/Tr;
Fs=2*Kr/C*Rmax;
Nr=round(1/PRF*Fs);
beamww=lumda/D*180/pi
Na=8192;
Rposi=[2000];
acenter=round(Na/2+Rposi*tan(sqtangle)/V*PRF);
Tgt=[Rposi(1), acenter(1)
   ];
beamw=lumda/D;
Ntarget=length(Tgt(:,1));
rawdata=zeros(Nr,Na);
t=[-Tr/2+Tr/Nr:Tr/Nr:Tr/2]';
Rst=0;
reftime=2*Rst/C;
for i=1:Ntarget
```

```
  R0=Tgt(i,1);
  centr=Tgt(i,2)-round(R0*tan(sqtangle)/V*PRF);
  aztime=2*(R0*tan(sqtangle)-R0*tan(sqtangle-lumda/2/D))/V;
  azlengPnt=round(aztime*PRF);
  if (mod(azlengPnt,2)~=0)
     azlengPnt=azlengPnt+1;
  end
  aztimeidx=[-azlengPnt/2+1:azlengPnt/2];
  azptidx=centr+aztimeidx;
  rgrealtime=t*ones(1,azlengPnt);
  azrealtime=ones(Nr,1)*[-aztime/2+aztime/azlengPnt:aztime/azlengPnt:aztime/2];
  doplcent=R0*tan(sqtangle)/V;
  azrealtime=azrealtime-doplcent;
  tao=2*sqrt(R0^2+(azrealtime+rgrealtime).^2*V^2)/C;
  rawdata(:,azptidx)=rawdata(:,azptidx)+exp(j*2*pi*Fc*tao+j*2*pi*Kr*rgrealtime.*tao);
end
```